**To cite this version :**

Alice ALÉON-TOPPANI, Rosario BRUNETTO, Zélia DIONNET, Stefano RUBINO, Donia BAKLOUTI, François BRISSET, Maxime VALLET, Eva HERIPRE, Tomoki NAKAMURA, Cateline LANTZ, Zahia DJOUADI, Ferenc BORONDICS, Christophe SANDT, David TROADEC, Obadias MIVUMBI, Megumi MATSUMOTO, Kana AMANO, Tomoyo MORITA, Hisayoshi YURIMOTO, Takaaki NOGUCHI, Ryuji OKAZAKI, Hikaru YABUTA, Hiroshi NARAOKA, Kanako SAKAMOTO, Shogo TACHIBANA, Toru YADA, Masahiro NISHIMURA, Aiko NAKATO, Akiko MIYAZAKI, Kasumi YOGATA, Masanao ABE, Tatsuaki OKADA, Tomohira USUI, Makoto YOSHIKAWA, Takanao SAIKI, Satoshi TANAKA, Fuyuto TERUI, Satoru NAKAZAWA, Sei-Ichiro WATANABE, Yuichi TSUDA - Correlated IR-SEM-TEM studies of three different grains from Ryugu: From the initial material to post-accretional processes - Geochimica et Cosmochimica Acta - Vol. 371, p.1-30 - 2024
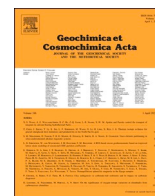
# Correlated IR-SEM-TEM studies of three different grains from Ryugu: From the initial material to post-accretional processes

Alice Aléon-Toppani [a],[*], Rosario Brunetto [a], Zélia Dionnet [a], Stefano Rubino [a],[b], Donia Baklouti [a], François Brisset [c], Maxime Vallet [d],[e], Eva Heripre [e],[f], Tomoki Nakamura [g], Cateline Lantz [a], Zahia Djouadi [a], Ferenc Borondics [h], Christophe Sandt [h], David Troadec [i], Obadias Mivumbi [a], Megumi Matsumoto [g], Kana Amano [g], Tomoyo Morita [g], Hisayoshi Yurimoto [j], Takaaki Noguchi [k], Ryuji Okazaki [l], Hikaru Yabuta [m], Hiroshi Naraoka [l], Kanako Sakamoto [n], Shogo Tachibana [o], Toru Yada [n], Masahiro Nishimura [n], Aiko Nakato [n], Akiko Miyazaki [n], Kasumi Yogata [n], Masanao Abe [n], Tatsuaki Okada [n], Tomohira Usui [n], Makoto Yoshikawa [n], Takanao Saiki [n], Satoshi Tanaka [n], Fuyuto Terui [p], Satoru Nakazawa [n], Sei-ichiro Watanabe [q], Yuichi Tsuda [n]

[a] Université Paris-Saclay, CNRS, Institut d'Astrophysique Spatiale, 91405 Orsay, France
[b] Istituto di Astrofisica e Planetologia Spaziali, INAF, Rome, Italy
[c] Université Paris-Saclay, CNRS, Institut de Chimie Moléculaire et des Matériaux d'Orsay, Orsay, France
[d] Université Paris-Saclay, CentraleSupelec, ENS Paris-Saclay, CNRS, LMPS-Laboratoire de Mecanique Paris-Saclay, Gif-sur-Yvette 91190, France
[e] Université Paris-Saclay, CentraleSupelec, CNRS, Laboratoire SPMS, 91190 Gif-sur-Yvette, France
[f] PIMM, Arts et Metiers Institute of Technology, CNRS, CNAM, HESAM University, 151 boulevard de l'Hopital, 75013 Paris, France
[g] Division of Earth and Planetary Materials Science, Laboratory for Early Solar System Evolution, Tohoku University, Sendai, Japan
[h] SOLEIL Synchrotron, Gif-sur-Yvette, France
[i] Institut d'électronique de microélectronique et de nanotechnologie, UMR 8520, Laboratoire central, Cité scientifique, Avenue Henri Poincaré, 59652 Villeneuve d'Ascq cedex, France
[j] Hokkaido University, Sapporo 060-0810, Japan
[k] Kyoto University, Kyoto 606-8502, Japan
[l] Kyushu University, Fukuoka 812-8581, Japan
[m] Hiroshima University, Higashi-Hiroshima 739-8526, Japan
[n] Institute of Space and Astronautical Science (ISAS), Japan Aerospace Exploration Agency (JAXA), Sagamihara 252-5210, Japan
[o] The University of Tokyo, Japan
[p] Kanagawa Institute of Technology, Atsugi 243-0292, Japan
[q] Nagoya University, Nagoya 464-8601, Japan

## ARTICLE INFO

## ABSTRACT

In order to better constrain the alteration history of the Ryugu parent body, we performed a multi-analytical study combining scanning electron microscopy, transmission electron microscopy and infrared spectroscopy on sections extracted from the three fragments A0064-FO019, A0064-FO021 and C0002-FO019 returned from Ryugu by the Hayabusa2 space mission. The three sections show large differences in terms of structure, mineralogy and infrared signature. Section A0064-FO019 resembles the major Ryugu lithology with the presence of both fine-grained phyllosilicates (fg-phyllos) with embedded nanosulfides and coarse-grained phyllosilicates (cg-phyllos), whereas section C0002-FO019 belongs to the group of the less altered lithologies with the presence of anhydrous minerals embedded in a partially amorphous matrix. Section A0064-FO021 also belongs to this group but shows two different lithologies, a compact amorphous one and a more porous and very fractured one showing the presence of Na-rich phosphate, calcite and olivine. The two less altered lithologies (sections A0064-FO021 and C0002-FO019) show the presence of numerous mineralogical features similar to those observed in cometary interplanetary dust particles, ultra-carbonaceous Antarctic micrometeorites or in the CM Paris

meteorite, i.e. amorphous and partially crystallized matrix with GEMS-like ghosts objects, whisker olivine, phosphide, or FeNi metal. This supports an outer solar system origin common with that of cometary material for the Ryugu parent body. Combined with the results of Nakamura et al. (2022b) reporting the presence of a lithology showing the presence of GEMS-like objects, we propose that section C0002-FO019 represents the onset of aqueous alteration of such primitive materials. The cg-phyllos and fg-phyllos of section A0064-FO019, i.e. of the major Ryugu lithology, representing the advanced stage of alteration, exhibit distinctive IR signatures with a higher abundance of oxygen-rich functional groups in the organic matter (OM) from the cg-phyllos. We thus suggest the following chronology of formation and evolution for Ryugu: (1) accretion of highly porous aggregate of GEMS-like units with fine-grained high-temperature anhydrous silicates, (2) onset of alteration with the dissolution of primary nanosulfides and development of amorphous/partially crystallized material in the pores, (3) crystallization of fg-phyllos with a second generation of sulfides, (4) later formation of cg-phyllos devoid of nanosulfides and their associated oxygen-rich OM in a more water-rich environment.

## 1. Introduction

In December 2019, the Hayabusa 2 sample return mission brought back to Earth 5.4 g of precious material from the Cb-type asteroid 162,173 Ryugu (Watanabe et al., 2019; Yada et al., 2022). The Hayabusa2 spacecraft performed two touch-down operations and sampled two different landing sites (Morota et al., 2020; Tachibana et al., 2022), one at the surface and the other one near the crater that the spacecraft made (Arakawa et al., 2020), stored in chamber A and C of the sample container (Sawada et al., 2017), respectively. This first collection of C-type carbonaceous asteroids, which are abundant in the asteroid belt and undersampled in our meteorite collections, will help to link meteorites and their parent asteroids and to better characterize the outer solar system bodies. Initial in situ laboratory analyses of Ryugu samples show that Ryugu, mainly composed of a phyllosilicates-rich matrix with abundant sulfides (pyrrhotite, pentlandite), carbonates, and magnetite, shares many mineralogical, chemical and isotopic similarities with CI chondrites (e.g. Yada et al., 2022; Nakamura et al., 2022a; Nakamura et al., 2022b; Yokoyama et al., 2023; Yabuta et al., 2023; Kita et al., 2023). Many analyses show that Ryugu material has suffered extensive aqueous alteration similar to CI chondrites, with a fluid temperature around 30 °C to 100 °C. However, they also show differences with CI chondrites, and in particular Ryugu material shows a higher porosity and more reduced characteristics. This may indicate that CI chondrites suffered additional modification/oxidation on Earth. In addition, Fe isotopic studies have revealed that Ryugu material sampled a reservoir different from other carbonaceous chondrites (Hopp et al., 2022). Observations of $CO_2$-bearing fluid inclusions suggest a formation of Ryugu in the outer solar system, beyond the $CO_2$ snow line (Nakamura et al., 2022b) and O-isotopic studies of anhydrous minerals (olivine or CAI-type minerals) point toward a link with cometary material (Liu et al., 2022; Kawasaki et al., 2022; Nakashima et al., 2023). Organic matter (OM) from Ryugu is also comparable to that in CI chondrites with the presence of organic nanoparticles and diffuse OM intimately mixed with phyllosilicates (Yabuta et al., 2023; Le Guillou et al., 2022). However, organic matter in the Orgueil CI chondrite presents more oxygenated functional groups than in Ryugu, which could point to different conditions of alteration on the parent body or alteration of OM on Earth (Le Guillou et al., 2022).

Remote observations of the surface and analyses of the returned samples point toward a formation of Ryugu by a re-accumulation of material ejected from a larger parent-body by an impact (Nakamura et al., 2022b; Yamaguchi et al., 2023; Yabuta et al., 2023). In particular, observations of the returned samples show that Ryugu is a breccia containing different clasts/lithologies with varying degrees of alteration. The most altered lithology shows the presence of Fe-bearing Mg-rich phyllosilicates mixed with sulfides whereas the least altered lithology shows the presence of anhydrous silicates with GEMS (Glass with Embedded Metal and Sulfide)-like objects (Nakamura et al., 2022b). Ryugu thus contains mixed materials with distinctive alteration histories revealing different local alteration conditions, maybe related to different origins inside its primary parent body.

At Université Paris-Saclay and SOLEIL synchrotron (France), we performed a multi-analytical sequence on several micrometer-sized fragments of Ryugu grains allocated during the initial analysis period (Rubino et al., 2023; Aléon-Toppani et al., 2021; Dionnet et al., 2023). Reflectance infrared measurements of 8 allocated fragments followed by their InfraRed computed micro-tomography (IR-CT) analysis were performed as a first non-destructive characterization of the mineral and OM and their distribution in the grains (Dionnet et al., 2023). Although few grains were analyzed, IR reflectance signatures revealed a variability of the mineral and OM among the grains (Dionnet et al., 2023), which could indicate that those grains sample different lithologies. An IR-CT and X-ray 3D computed tomography (XCT) campaign was performed on four of the allocated fragments and results are reported by Dionnet et al., 2023. Here, we present a multi-analytical study combining scanning electron microscope (SEM)/Transmission electron microscope (TEM)/IR on slices extracted from three other allocated fragments (different from the ones analyzed by XCT) showing very different IR signatures in order 1/ to better understand the origin of this IR signature variability, 2/ if related to different lithologies, to better characterize those different lithologies. Combining these different techniques (SEM/TEM/IR) is a powerful tool as it allows linking molecular studies of the mineral and OM with more classical chemical and mineralogy from the micrometer to the nanometer scale. The present multi-analytical study aims thus at better characterizing the brecciated nature of Ryugu.

## 2. Methods

This study is part of a larger campaign performed in the framework of the initial analysis group "STONE", led by T. Nakamura. First results were presented in Nakamura et al., (2022b) and Dionnet et al. (2023). We received more than 20 fragments (ranging from 30 to 80 μm in size) from Tohoku University that spontaneously detached or were scratched from ~three millimeter-sized grains A0064, C0046 and ~eight-millimeter-sized grain C0002. A0064 was sampled at the first touch-down site, and C0046 and C0002 at the second touch-down site. All these fragments have been initially characterized inside $N_2$ sample holder as described in Rubino et al. (2023).

In this study, we followed part of the previously developed multi-analytical procedure (Aléon-Toppani et al., 2021; Dionnet et al., 2022) shown in Fig. S1. Details of the preparation procedure for each step can be found in Aleon-Toppani et al. 2021. Eight fragments characterized by IR surface reflectance were each welded to a tungsten or aluminum needle in order to characterize the 3D distribution of organics and minerals by IR-CT. Both IR surface reflectance and tomography measurements of the 8 fragments presented in Dionnet et al. (2022) and Dionnet et al. (2023) were used to choose 1/ the fragments from which slices will be extracted and 2/ the localization of the slices. The 3 chosen fragments were then recovered from the metallic needles and 2.5 μm thick slices were extracted using FIB-SEM (Focused Ion Beam-SEM). Because of time limitation during the initial analysis period, only one or two slices were extracted from each fragment. The extracted slices were subsequently analyzed by SEM and 2D IR mapping to combine

mineralogical, chemical and molecular information on organic and silicate matter. Those slices were then thinned down to 100 nm and analyzed by TEM to get information at a nanometer scale.

### 2.1. Choice of the sample and localization of the slicing

IR reflectance spectra of the 8 fragments are reported in Fig. 2 in Dionnet et al. (2023). A precise list of attributed main IR spectral signatures for those 8 fragments can be found in table 1 of Dionnet et al. (2023). Overall, they show the presence of IR vibrational features characteristic of the presence of OM (between 2900 and 3000 cm$^{-1}$ for the CH stretching vibrations and between 1200 and 1400 cm$^{-1}$ for the CH bending and aromatic C=C vibrations, as well as a small feature at 1260 cm$^{-1}$ attributed to C-O stretching vibrations), molecular water-OH and phyllosilicate structural M—OH stretching vibrations (between 3000 and 3700 cm$^{-1}$ and around 3660 cm$^{-1}$ respectively), carbonates (vibrations at 880 cm$^{-1}$, 1437 cm$^{-1}$, 2533 cm$^{-1}$ and ~ 2902 cm$^{-1}$ in the fragment A0064-FO023) and silicates (major band between 996 and 1020 cm$^{-1}$ depending on the grain). The presence and the intensity of those features vary between the different fragments. A subset of the fragments was dedicated combining IR-CT and X-CT measurements whereas the other subset was dedicated to mineralogy and IR measurements with a better spatial resolution.

We chose to slice the ones showing large differences in (1) the degree of hydration based on the intensity of the M—OH band, (2) the quantity of OM based on the intensity of the aliphatic CH stretching band and finally (3) the nature of the silicates based on the shape/position of the Si-O vibration band. We chose fragment A0064-FO019 because of the presence of an important structural M—OH stretching band and of an asymmetric silicate band with a maximum around 1014 cm$^{-1}$. Fragment A0064-FO021 was chosen because of the presence of a very weak M—OH band and the presence of an important molecular water-OH band. We finally chose to slice the C0002-FO019 fragment because of the presence of the silicate band with a maximum around 996 cm$^{-1}$, which was very different from the other slices (1014 cm$^{-1}$ and 1002 cm$^{-1}$ for fragments A0064-FO019 and A0064-FO021, respectively). The choice of this fragment was also driven by its origin from the C-batch.

### 2.2. FIB preparation of the SEM and TEM samples

Samples were prepared using a FEI ThermoFisher Helios Nanolab 660 SEM-FIB at Centrale-Paris (Université Paris-Saclay) following the procedure presented by Aléon-Toppani et al. (2021). Using FIB-SEM (Fig. 1), a) the fragments were welded using Pt at the tip of W needles to perform IR micro-tomography and IR surface reflection measurements, (2) the fragments were recovered from the W needle and deposited on gold conductive plate in order to cut them in several slices. After extraction, the thick slices were welded on TEM grids for 2D-IR spectroscopy and SEM characterization. After analyses, they were thinned down to 100 nm for TEM observations. Details of analytical parameters are given in Aléon-Toppani et al. (2021).

Two consecutive slices were extracted from the bottom part of fragment A0064-FO019 (in the region showing Si-O-Si band peak position varying between 999 and 1007 cm$^{-1}$, see Fig. 3 by Dionnet et al., 2023). Two slices were extracted from both ends of the C0002-FO019 fragment, and finally only one slice was cut in fragment A0064-FO021. Because SEM and IR results were very similar on the two slices extracted from each of the fragments A0064-FO019 and C0002-FO019, only one slice for each fragment was chosen and thinned down to 100 nm.

### 2.3. SEM

Characterization of the thick slices was performed using a Zeiss Supra 55 VP FEG SEM and Zeiss Sigma HD SEM (ICMMO, Univ. Paris-Saclay) equipped with an EDAX energy dispersive detector. Because the TEM grids holding the thick slices were deposited on a Al holder, a slight contamination in Al could be possible depending on the orientation of the holder. EDS (Energy-dispersive X-ray spectroscopy) mapping was performed at 5 keV to increase the spatial resolution, minimize phase mixing and holder contamination. Uncertainties for heavy elements (e.g. Ca) can thus be large, and some elements such as Mn were not measured. In addition, although phase mixing was minimized, contamination of adjacent phases can be possible because of the sub-μm size of the phases. EDS analyses were extracted from the EDS maps using IDFix-Maxview software.



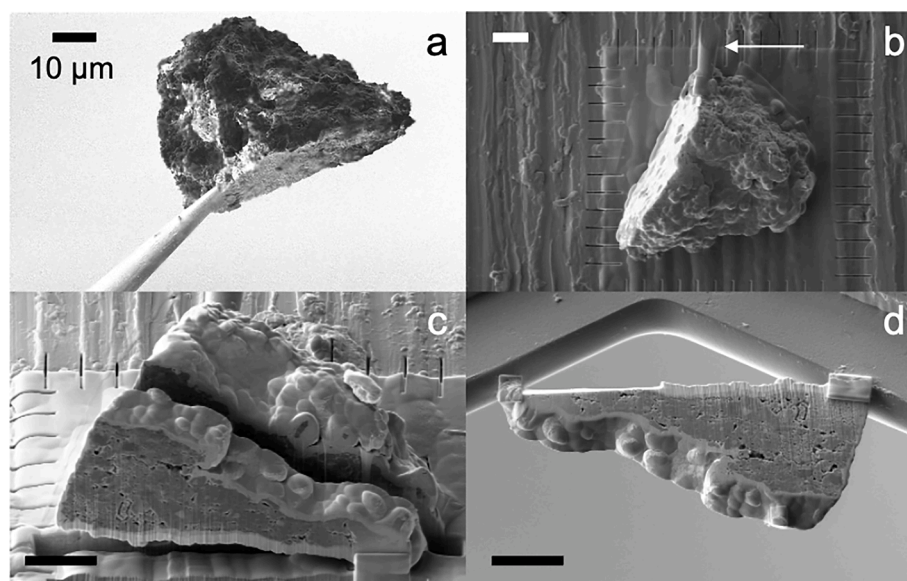**Fig. 1.** Secondary electron images of a) grain A0064-FO021 welded on a tungsten needle for IR measurement, b) grain A0064-FO021 recovered after IR measurement, deposited on gold plate and coated with platinum before slicing. c) grain A0064-FO021 sliced and d) final ~2.5 μm thick slice welded to a M−FIB grid. Arrow in (b) indicates the remaining of the cut tungsten needle at the top of the grain. All scale bars correspond to 10 μm.
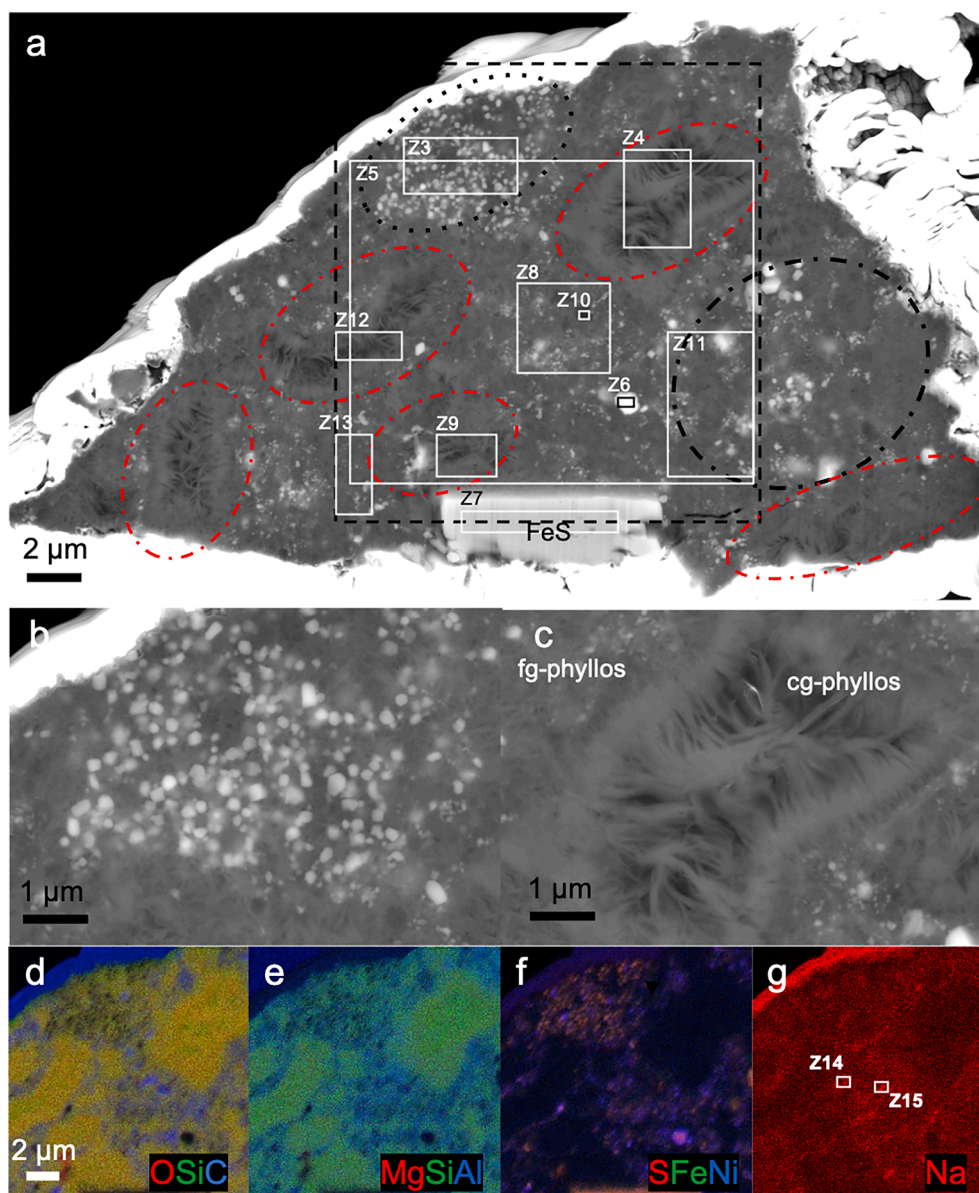
**Fig. 2.** a) SEM-BSE image of the thick slice extracted from grain A0064-FO019. The white layers surrounding the section correspond to the platinum deposit. b) SEM-BSE image of the fg-phyllos sulfide-rich region. Notice the euhedral morphology of the sub-µm sulfides. c) BSE image of the cg-phyllos. Cg-phyllos show large and oriented packets of layers radiating inward the void. d) composite X-ray map of O (red), Si (green) and C (blue) showing the very low concentration in C in the cg-phyllos. e) composite X-ray map of Mg (red), Si (green) and Al (blue). f) composite X-ray map of S (red), Fe (green) and Ni (blue) showing the presence of both Ni-rich and Ni-poor sulfide and g) X-ray map of Na distributed heterogeneously in the sample. On BSE image (a), red and black dashed-line circles indicate cg-phyllos- and fg-phyllos-rich regions, respectively. The black dashed-line rectangle indicates the analyzed zone corresponding to the X-ray maps (d-g). The numbered white rectangles correspond to zones analyzed by EDS (Table 1). Abbreviations: FeS for sulfide, cg-phyllos for coarse-grained phyllosilicates, fg-phyllos for fine-grained phyllosilicates.

## 2.4. TEM

Thinned samples were characterized using 1/ a 200 kV JEM-2100+ microscope (Univ. Paris-Saclay) equipped with a Gatan CMOS RIO 16 camera and an EDS-SDD system using the EDS SAMx analysis system, and 2/ a Titan3 G2 80–300 microscope (FEI ThermoFisher) (Centrale-Supelec, Univ. Paris-Saclay) equipped with a super X EDS detector (with 4 SSD detectors). Observations and analysis were performed at 300 keV with the Titan TEM.

Imaging was carried out in a conventional mode (bright field) as well as in scanning mode (STEM) using the high angle annular dark field (STEM- HAADF) and the annular bright field detectors (STEM-ABF) of the Titan TEM. Chemical analyses were obtained in conventional mode on the JEOL TEM and in STEM mode on the Titan TEM. The STEM-EDS mapping was performed during a total time of acquisition of 10 to 30 min using a probe size of 1 to 10 nm depending on the map. The elemental maps represent a sum of signal over the total time of acquisition. Compositional data were extracted from the STEM-EDS maps using Esprit software by adding pixels from the data cubes in given regions of interest.

Element abundances were quantified from EDS spectra by fitting peaks for all elements detected and applying a Cliff–Lorimer thin-film correction procedure (Cliff and Lorimer, 1975). SAMx and Esprit softwares were used respectively for analyses obtained with the JEOL and TITAN microscopes. Relative uncertainties for the major elements are typically 5—10 % whereas those for minor elements ($\sim$<1%) are around 20 %. Elemental abundances were normalized to 100 %. Oxygen abundances should be viewed with caution because of variable amounts of self-absorption by the sample. Imaging and EDS were carried out with low dose conditions to minimize sample damage.
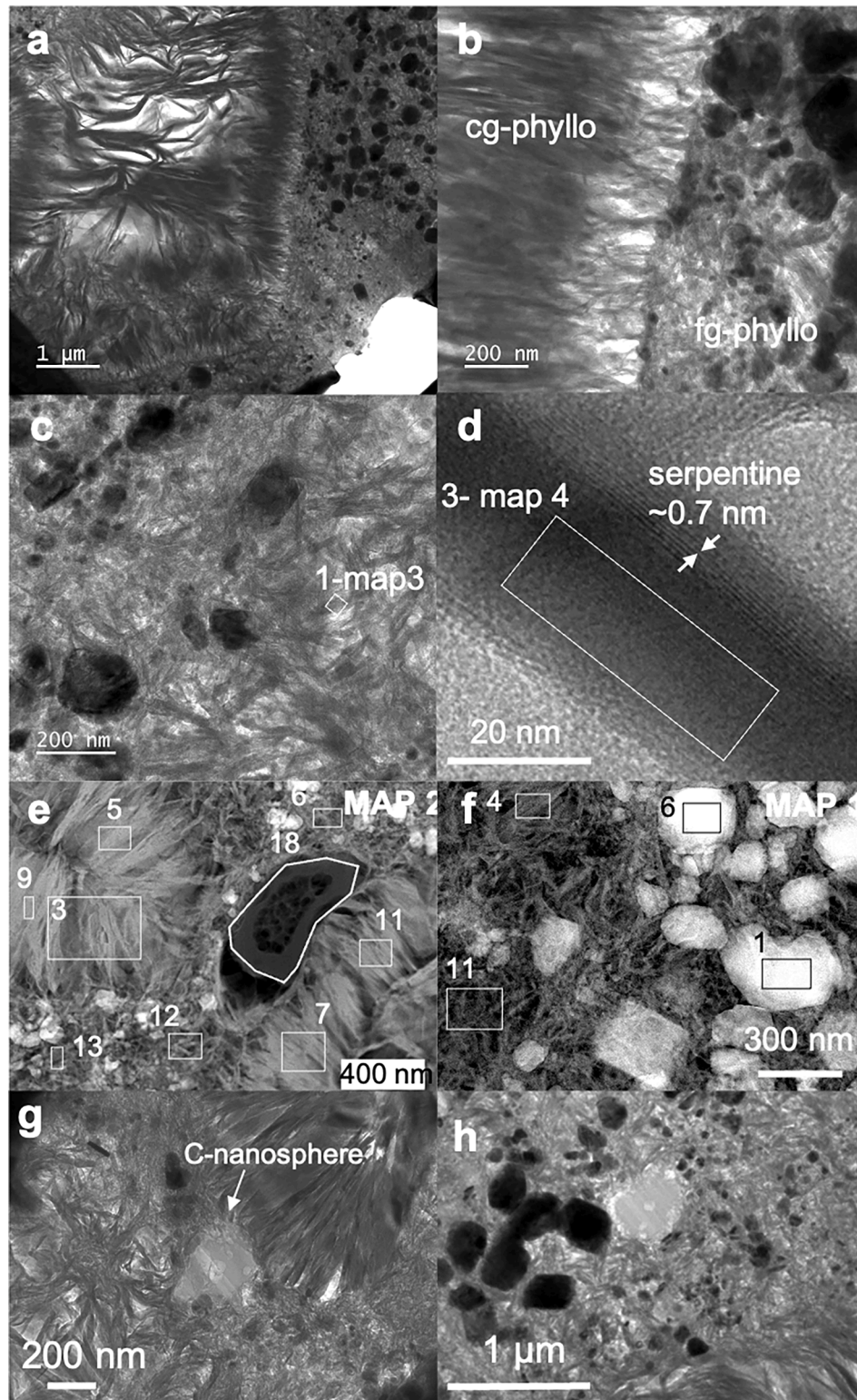
**Fig. 3.** TEM images from section A0064-FO019. (a-d) Bright field TEM images of phyllosilicates. (a) Contact between cg-phyllos and the fg-phyllos-rich matrix. (b) Detail of another contact between cg- and fg-phyllos. (c) Fg-phyllos-rich region. (d) High resolution image of a cg-phyllos. The interlayer width is ~ 0.71 nm, corresponding to that of a Fe-bearing serpentine-group mineral. (e-f) HAADF-STEM images of two different regions of section A0064-FO019 showing (e) the presence of nanosulfides and a C-rich nanoglobule (circled in white) embedded in a fg-phyllos-rich region between two cg-phyllos patches, and (f) of sub-μm sulfides embedded in a fg-phyllos-rich region. (g-h) Bright field TEM images of C-rich nanospheres with a vesicular core embedded in fg-phyllos-rich regions of section A0064-FO019. The numbered white or black rectangles correspond to zones from which EDS analyses were extracted from STEM-X-ray maps 2 and 1 (Table 3).

## 2.5. IR spectroscopy

IR micro-spectroscopy of the thick slices was performed using an Agilent Cary 670 Fourier-Transform IR (FTIR) microscope equipped with a Focal Plane Array Detector (FPA) (SOLEIL, France) in transmission mode. The spectral resolution was 4 cm$^{-1}$. The spectral range extended from 800 to 3950 cm$^{-1}$. A 25× objective was used in combination with a high magnification system placed in front of the 128x128 or 64 × 64 pixels FPA detector. The projected pixel size was ~0.66 μm and the field of view was ~84 μm or ~42 μm, respectively. The spatial resolution was diffraction-limited in the whole spectral range. Acquisition time was limited to 512 scans. Before each analysis, a background spectrum of an empty field of view was acquired (no sample).

In order to determine the distribution of different bands, we draw linear baselines and calculated band areas without Gaussian fit in different spectral ranges. Spectral integration of band areas was performed in Quasar (https://quasar.codes) using the Orange Spectroscopy toolbox (Toplak et al., 2017).

## 3. Results

In the following, we will present the results concerning the SEM and IR mapping observations of the 3 representative thick sections extracted from fragments A0064-FO019, C0002-FO019 and A0064-FO021 (Figs. 2, 5 and 10). They were subsequently observed by TEM in the thinned zones. EDS analyses realized with both TEM and SEM are reported in Tables 1, 2 and 3. Matrix and sulfides analyses are reported in ternary diagrams in Fig. 4. Localizations of the TEM/SEM analyses are reported in the different figures.

### 3.1. Mineralogy and chemical composition of the 3 slices

#### 3.1.1. Fragment A0064-FO019

The thick section of fragment A0064-FO019 is approximately 10 μm by 17 μm (Fig. 2a) large. It shows the presence of Fe-bearing Mg-rich coarse-grained phyllosilicate (named hereafter cg-phyllos) distributed in several patches from 1 μm to over 10 μm long and of a Fe-bearing Mg-rich fine-grained phyllosilicate-rich matrix (named hereafter fg-phyllos). Fg-phyllos mostly appear as randomly oriented packets of layers with a heterogeneous width <10 nm to 30 nm (Fig. 3c). Cg-phyllos show larger widths (30 to 100 nm) and more oriented packets of layers. In addition, they seem to fill voids with a growth perpendicular to the surface of the voids (Figs. 2 and 3a, 3b). Some TEM observations of the cg-phyllos show the presence of serpentine (Fig. 3d) phyllosilicate with a width interlayer around 0.7 nm.

EDS-SEM analyses of different regions of the matrix show variation of the content of Fe and S, but a relatively stable Mg/Si ratio which is principally linked to the abundance of sulfides in the analysed regions (Table 1). However, local STEM analyses (Fig. 3c, d, e, f, Table 3) show a difference in the chemical composition between the cg-phyllos and the fg-phyllos with the cg-phyllos showing a higher (Mg + Fe)/Si ratio than the fg-phyllos (1 and 0,7 respectively) which can be attributed to a higher Mg content in the cg-phyllos. Those local STEM analyses reveal content in Fe around 3 at%, while the Mg/(Mg + Fe) ratio of both fg- and cg-phyllos varies between 0.7 and 0.9 with a mean around 0.8. In addition, local STEM analyses of fg- and cg-phyllos are reported in a Si+Al-Fe-Mg ternary diagram (Fig. 4). Fg-phyllos plot along the saponite solid solution line with a slightly enriched content in Si whereas cg-phyllos lie between the saponite and serpentine solid solution line, both with enrichment toward the Fe endmember. Al and Na contents of different regions of the matrix vary from ~1 at% to 3–4 at% and from ~1 to 3 at%, respectively, with the fg-phyllos region being the richer in Al and Na (see Mg-Si-Al X-ray Map – Fig. 2e). The Na distribution seems to be heterogeneous at the μm scale with some small regions (<500 nm) showing enrichments up to 5 at% in Na (Fig. 2g).

No sulfide was observed in the cg-phyllo patches, whereas in addition to the tiny sulfides (100 to 200 nm) heterogeneously distributed in the matrix, several larger euhedral sulfides from 500 nm up to several μm were observed in the section (Fig. 2f). As shown by EDS local analyses and chemical maps (Table 1, Fig. 3 and Fig. 2f), the large sulfide present in the bottom part of the section is a pyrrhotite (zone Z7- Table 1). Smaller pyrrhotites were also observed in addition to small Ni-rich sulfides (zone Z6 – Fig. 2). In this section, the fg–phyllo matrix shows a region (zone Z3- Fig. 2) very rich in 100–200 nm sized sulfides whereas in other parts of the section, the fg-phyllos matrix shows also larger 500 nm-sized sulfides in addition to fewer tiny sulfides (e.g. zone Z11- Fig. 2). TEM observations reveal that the sulfides seem largely rounded to euhedral (Fig. 3f) with a size down to tens of nm. The few analyses of the different observed sulfides (either acquired with TEM or SEM) were reported in a Fe-S-Ni ternary diagram and lie along the pyrrhotite solid solution (Fig. 4). No correct analyses of Ni-rich sulfides were acquired (i.e. without contamination from the adjacent matrix).

The carbon map shows a heterogeneous diffuse distribution of carbon in the section with in particular, a very low abundance of C in the cg-phyllos-rich regions (Fig. 2d). Several 200 to 500 nm-C rich nanospheres with a vesicular core were observed in the fg-phyllos-rich regions (Fig. 3g, h), with some in contact with the cg-phyllos (Fig. 3h). One C-rich nodule was analyzed with EDS-TEM (~82 % at C, 15 % at 0) and is enriched in Na (1,5% at). EDS-SEM analyses show also a peak in nitrogen, showing its presence but quantification was too uncertain.

No Ca, Fe or Mg carbonate, magnetite or phosphate was observed in this section.

#### 3.1.2. Fragment C0002-FO019

The thick section of grain C0002-FO019 is approximately 20 μm by 20 μm large (Fig. 5). It shows a completely different texture from A0064-FO019, with presence of anhydrous minerals embedded in a very fine-grained porous and fibrous Fe-bearing Mg-rich matrix. This matrix shows regions with different crystallinity, from amorphous regions (Fig. 6a with its associated diffraction pattern) to zones with a low crystallinity (Fig. 6b) and finally to relatively well crystallized zones (Fig. 6c), and different porosity. Global compositions (EDS-SEM) of different large regions (7 by 7 μm$^2$) of the sections (see Fig. S2 for their locations) are reported in table 1 and show 1/ small variability in Na, Al, Mg and Si, 2/ variability in Fe and S attributed to an heterogeneous distribution in magnetite and/or sulfide. Al and Na contents of different regions of the matrix varies from 1 to 3.5 at% and from 0 to 1 at% at respectively.

Local STEM analyses of the matrix reveal content in Fe around 3–4 at %. They are reported in a Si+Al-Fe-Mg ternary diagram (Fig. 4) and lie between the saponite solid solution line and the serpentine solid solution line with enrichment toward the Fe endmember. Saponite-type phyllosilicate was observed with an interlayer width around 1 nm in one region. One small phyllosilicate-rich nodule (from 200 to 500 nm) was also observed with an Al and Na enrichment up to 6.5 and 2 at%, respectively.

Several olivine-rich zones (see areas within the red dashed circles on Fig. 5a) are present with olivines from 200 nm to almost 1.5 μm. The olivine-rich zones are several micrometers large. The olivines show different habitus with anhedral olivine (Fig. 7a and b), rounded olivines or elongated olivines that appear as platelet or whisker (Fig. 7c). TEM observations reveal the presence of vesicles in some olivines with the number of those vesicles increasing under the electron beam (Fig. 7e). Olivines in zone 2 (Fig. 5a from SEM and Fig. 7d for TEM observations, respectively) seem to show a triple junction. One μm-sized olivine shows some defects (Fig. 7b). However, the observed olivine grains do not show features of alteration. Local SEM, TEM and STEM non-contaminated analyses all point toward Fo99.7 to 99.9 composition and Mn content between 0.1 and 0.3 at%.

Several 1 to 2 μm large sulfides were observed in addition to numerous very tiny sulfide (50 to 500 nm). SEM-EDS maps (Fig. 5a) reveal that 1/ one of these sulfides (pyrrhotite FeS-G6) is closely

**Table 1**

Composition (at%) of different areas of sections A0064-FO019, A0064-FO021 and C002-FO019 extracted from SEM-EDS spectral maps. The locations of the different areas are indicated in Figs. 2, 5 and 10 except for the global analyses of section C002-FO019, which are given in Fig. S1. The location of global analysis for section A0064-FO021 corresponds to the dotted black rectangle in Fig. 10a. The carbon content is indicated for low-C phases but is not included in totals. It is by contrast reported for C-rich phases where it contributes to the totals. The carbon content of olivines is around 1 to 2 at%, which gives an estimate of the C contamination of the analyses. N content of the C-rich nanoparticles is indicated when the N peak was clearly identified in the spectra. However, quantification has to be taken with caution. Bd is indicated when %at $\leq$ 0.3. Nd is indicated when element was not quantified. LC is for low-count.

| | counts | C ind | C | N | O | Na | Mg | Al | Si | P | S | Ca | Fe | Ni |
|---|---|---|---|---|---|---|---|---|---|---|---|---|---|---|
| **Grain A0064-FO019** | | | | | | | | | | | | | | |
| Z5-global zone | | 11.6 | | | 54.8 | 1.9 | 15.8 | 3.7 | 14.9 | bd | 3.1 | nd | 5.0 | 0.6 |
| Z3-fg-phyllos-rich. sulfur-rich matrix | | 10.7 | | | 47.5 | 1.7 | 13.4 | 3.3 | 13.3 | bd | 10.0 | nd | 9.9 | 0.7 |
| Z11-fg-phyllos-rich matrix | | 14.6 | | | 53.0 | 2.2 | 15.0 | 4.3 | 14.6 | bd | 4.0 | nd | 5.8 | 0.9 |
| Z8-fg-phyllos-rich matrix | | 18.9 | | | 50.7 | 2.9 | 14.4 | 5.1 | 14.2 | bd | 4.8 | nd | 6.8 | 0.9 |
| Z13-fg-phyllos-rich matrix | | 15.4 | | | 53.4 | 2.2 | 15.4 | 4.2 | 15.0 | bd | 3.4 | nd | 5.3 | 0.8 |
| Z9-cg-phyllos | | 6.3 | | | 59.2 | 1.3 | 17.4 | 2.6 | 15.6 | bd | 0.6 | nd | 3.2 | bd |
| Z12-cg-phyllos | | 5.2 | | | 59.5 | 1.0 | 17.8 | 2.4 | 16.5 | bd | bd | nd | 2.6 | bd |
| Z4-cg-phyllos | | 4.4 | | | 60.1 | 1.0 | 17.8 | 2.3 | 16.2 | bd | bd | nd | 2.4 | bd |
| Z14-Na-rich zone | | 13.5 | | | 50.9 | 4.2 | 14.0 | 4.8 | 13.6 | bd | 4.5 | 0.6 | 5.1 | 2.1 |
| Z15-Na-rich zone | | 25.0 | | | 36.4 | 4.8 | 9.4 | 3.7 | 9.7 | bd | 5.4 | nd | 4.5 | 0.8 |
| Z6-sulfide | | | | | 13.1 | 0.9 | 1.5 | 1.5 | 2.7 | bd | 32.0 | 1.8 | 19.6 | 25.4 |
| Z7-pyrrothite | | | | | 6.1 | bd | 1.0 | 0.4 | 0.7 | bd | 48.7 | nd | 41.7 | 1.5 |
| Z10- C-rich zone | | | 38.3 | 0.9 | 32.7 | 2.6 | 8.5 | 4.0 | 7.8 | bd | 1.5 | 0.4 | 2.9 | 0.5 |
| **Grain C002-FO019** | | | | | | | | | | | | | | |
| G-global zone | | 14.3 | | | 53.4 | 0.9 | 14.9 | 3.3 | 16.1 | bd | 3.7 | bd | 6.6 | 1.2 |
| I-global zone | | 17.9 | | | 54.1 | 0.9 | 14.1 | 3.4 | 15.1 | bd | 3.3 | bd | 8.3 | 0.8 |
| E-global zone | | 9.8 | | | 53.6 | 0.7 | 15.2 | 2.0 | 13.8 | bd | 5.1 | bd | 9.0 | 0.7 |
| K-global zone | | 12.6 | | | 56.4 | 0.8 | 15.6 | 0.5 | 15.6 | bd | 3.3 | bd | 6.9 | 0.8 |
| B-global zone | | 19.1 | | | 53.6 | 1.0 | 14.5 | 3.3 | 15.2 | bd | 3.9 | bd | 7.4 | 1.1 |
| C-global zone | | 21.0 | | | 50.5 | 1.3 | 13.5 | 2.8 | 15.2 | bd | 6.6 | bd | 8.9 | 1.3 |
| E6-large olivine | | 1.2 | | | 55.3 | bd | 30.5 | bd | 13.6 | bd | bd | bd | bd | bd |
| E7-olivine | <1000 | | | | 56.7 | bd | 30.0 | bd | 13.0 | bd | bd | bd | bd | bd |
| I2-olivine | <1000 | | | | 56.6 | bd | 29.0 | bd | 12.5 | bd | 0.7 | bd | 0.6 | bd |
| I3-olivine | <1000 | | | | 54.5 | 0.6 | 27.7 | 0.7 | 12.8 | bd | 1.6 | bd | 1.6 | 0.5 |
| g8-matrix | | 14.2 | | | 55.6 | 0.7 | 14.8 | 2.7 | 16.0 | bd | 2.9 | bd | 6.4 | 0.9 |
| g9-matrix | | 13.3 | | | 57.4 | 0.7 | 15.7 | 1.8 | 15.8 | bd | 2.2 | bd | 5.8 | 0.7 |
| b5-matrix | | 18.6 | | | 53.2 | 1.0 | 14.6 | 3.9 | 15.2 | bd | 3.9 | bd | 7.5 | 1.1 |
| c8- matrix | | 10.8 | | | 56.1 | 0.9 | 15.7 | 2.5 | 16.2 | bd | 2.3 | bd | 5.5 | 0.8 |
| c9-matrix | | 23.5 | | | 51.3 | 0.8 | 14.5 | 3.4 | 15.7 | bd | 4.8 | bd | 8.8 | 0.7 |
| i8-matrix | | 18.3 | | | 53.2 | 0.9 | 14.6 | 3.3 | 15.6 | bd | 3.8 | bd | 7.5 | 1.1 |
| i9-matrix | | 11.3 | | | 55.9 | 0.6 | 15.5 | 2.9 | 15.8 | bd | 2.4 | bd | 6.2 | 0.7 |
| k7-matrix | | 12.8 | | | 56.4 | 0.8 | 15.6 | 0.5 | 15.6 | bd | 3.3 | bd | 6.9 | 0.8 |
| G6-pyrrhotite | <1000 | | | | 3.3 | bd | bd | 0.4 | 0.6 | bd | 52.8 | bd | 40.3 | 1.9 |
| G7-Fe$_2$Ni metal | <1000 | | | | 4.0 | bd | 1.0 | 0.8 | 1.3 | bd | bd | bd | 32.1 | 58.9 |
| C1-(Fe, Ni)$_3$S$_2$ sulfide | <1000 | | | | 1.7 | bd | bd | bd | bd | bd | 41.4 | bd | 22.0 | 34.4 |
| G4-magnetite | <1000 | | | | 58.3 | 0.6 | 2.1 | 0.9 | 1.7 | bd | 1.6 | bd | 34.5 | 0.4 |
| I6-magnetite | <1000 | | | | 55.2 | 0.8 | 0.8 | 0.9 | 1.1 | bd | 2.0 | bd | 38.8 | 0.5 |
| K4-magnetite | <1000 | | | | 58.7 | bd | 0.4 | bd | 0.6 | bd | 0.5 | bd | 39.5 | bd |
| K5-magnetite | | | | | 58.6 | bd | 2.7 | 1.7 | 2.5 | bd | 0.4 | bd | 33.7 | bd |
| B2-magnetite | | | | | 58.0 | 0.4 | 2.6 | 0.7 | 2.6 | bd | 1.2 | bd | 34.2 | bd |
| Ca1- small carbonate | <500 | 11.9 | | | 65.1 | bd | 1.4 | bd | 1.5 | bd | 1.7 | 16.3 | 1.3 | 0.4 |
| C3-C-rich zone | <500 | | 52.5 | 0.9 | 32.5 | 0.6 | 5.9 | bd | 5.0 | bd | 1.3 | bd | 1.0 | 0.4 |
| C4-C-rich zone | <500 | | 57.5 | 1.1 | 24.6 | 1.1 | 5.6 | 2.4 | 5.9 | bd | 1.2 | bd | 0.4 | bd |
| C5-C-rich zone | <500 | | 65.7 | 2.1 | 21.5 | 1.1 | 2.5 | 0.0 | 2.1 | bd | 3.3 | bd | 1.0 | 0.8 |
| **Grain A0064-FO021** | | | | | | | | | | | | | | |

7

**Table 1** (*continued*)

| | counts | C ind | C | N | O | Na | Mg | Al | Si | P | S | Ca | Fe | Ni |
|---|---|---|---|---|---|---|---|---|---|---|---|---|---|---|
| Global left zone | | 24.1 | | | 52.4 | 1.2 | 11.8 | 2.7 | 12.5 | bd | 6.6 | 0.2 | 11.5 | 1.1 |
| Global right zone | | 15.6 | | | 54.9 | 1.2 | 12.9 | 2.1 | 12.4 | 0.6 | 3.8 | 1.2 | 9.0 | 1.1 |
| | | | | | | | | | | | | | | |
| Ol1-rounded Olivine | | 1.2 | | | 56.6 | bd | 29.4 | 0.0 | 13.0 | bd | bd | nd | 0.6 | bd |
| Ol2-platelet Olivine | | | | | 57.1 | bd | 28.0 | 0.0 | 13.7 | bd | bd | nd | 0.7 | bd |
| | | | | | | | | | | | | | | |
| Z3-compact matrix | | 11.6 | | | 57.8 | 2.3 | 14.3 | 1.5 | 13.7 | bd | 2.5 | nd | 7.0 | 0.7 |
| Z11-compact matrix | | 8.3 | | | 58.1 | 1.1 | 14.9 | bd | 13.5 | bd | 3.0 | nd | 8.3 | 0.9 |
| Z14-compact matrix | | 8.9 | | | 58.6 | 1.0 | 15.2 | bd | 13.7 | bd | 2.6 | | 8.1 | 0.9 |
| | | | | | | | | | | | | | | |
| Z4-no-compact matrix | | 23.7 | | | 49.6 | 1.8 | 10.3 | 1.4 | 12.3 | bd | 9.3 | nd | 13.7 | 1.5 |
| Z5-no-compact matrix | | 26.2 | | | 48.5 | 1.7 | 9.6 | 1.6 | 11.1 | bd | 10.4 | nd | 14.6 | 2.2 |
| | | | | | | | | | | | | | | |
| Ca6-large carbonate | | 16.6 | | | 58.9 | 0.4 | bd | bd | 0.7 | bd | bd | 21.5 | 0.5 | 0.7 |
| Ca7-small carbonate | | 15.5 | | | 58.6 | bd | 1.1 | bd | 1.6 | bd | bd | 21.1 | 1.2 | bd |
| | | | | | | | | | | | | | | |
| Pho8-small phosphate | <1000 | 21.7 | | | 43.6 | 2.7 | 6.9 | 1.7 | 5.9 | 4.1 | 4.2 | 3.1 | 5.7 | 0.5 |
| Pho1-large phosphate | | 5.0 | | | 60.5 | 2.0 | 1.2 | bd | 0.9 | 10.7 | bd | 20.8 | 2.4 | 0.5 |
| | | | | | | | | | | | | | | |
| FeS-19-large sulfide | <1000 | | | | bd | bd | 0.8 | bd | 1.1 | bd | 51.1 | bd | 45.0 | 2.0 |
| FeS-22-sulfide | | | | | 0.0 | 0.7 | bd | bd | 1.9 | bd | 51.4 | bd | 44.7 | 1.1 |
| | | | | | | | | | | | | | | |
| mt20-magnetite | <1000 | | | | 57.0 | bd | 0.4 | bd | 1.2 | nd | 0.5 | bd | 40.8 | bd |
| mt21-magnetite | <1000 | | | | 59.8 | bd | bd | bd | 0.6 | nd | 0.7 | bd | 38.5 | bd |
| | | | | | | | | | | | | | | |
| C6-C-rich zone | <1000 | | 47.2 | 2.0 | 30.9 | 1.4 | 7.1 | bd | 6.3 | bd | 1.2 | bd | 3.6 | bd |
| C7-C-rich zone | <500 | | 33.7 | 0.8 | 38.7 | 0.6 | 7.6 | 1.8 | 7.5 | bd | 2.7 | bd | 5.6 | 0.4 |
| C8-C-rich zone | <500 | | 29.6 | 0.7 | 42.9 | 1.1 | 9.7 | 1.0 | 8.1 | bd | 1.2 | bd | 4.8 | bd |
| C9-C-rich zone | <1000 | | 60.8 | nd | 20.7 | 3.0 | 3.0 | 0.0 | 2.9 | 0.6 | 4.8 | bd | 3.3 | 1.0 |
| C10-C-rich zone | <500 | | 55.8 | nd | 22.3 | 2.5 | 3.7 | 0.0 | 4.0 | 0.7 | 2.6 | bd | 6.6 | 1.8 |
| C12-C-rich zone | <500 | | 46.8 | nd | 26.5 | 2.4 | 5.8 | 0.0 | 5.0 | 1.3 | 3.7 | bd | 7.0 | 1.5 |
| C13-C-rich zone | <1000 | | 47.3 | nd | 24.6 | 2.8 | 4.5 | 0.0 | 6.0 | 0.9 | 5.1 | bd | 6.4 | 2.4 |

**Table 2**

Composition (at%) of different areas of sections A0064-FO021 and C002-FO019 measured using JEOL 200 kEV TEM in conventional mode. The locations of the different areas are indicated by red circles in all figures (including Fig. S4 for analyse 12 section A0064-FO021). No compositions are reported for section A0064-FO019 due to a contamination caused by the double tilt TEM grid holder. The carbon content is indicated for low-C phases but does not contribute to the totals sum. It is reported for C-rich phases and contributes to the totals. Bd is indicated when %at < 0.2 %.

| | C ind | C | O | Na | Mg | Al | Si | P | S | Ca | Mn | Fe | Ni |
|---|---|---|---|---|---|---|---|---|---|---|---|---|---|
| **Grain C002-FO019** | | | | | | | | | | | | | |
| 1- olivine | 1.2 | | 59.0 | bd | 27.0 | bd | 13.4 | bd | bd | bd | 0.3 | bd | bd |
| 2- olivine | 1.6 | | 58.6 | bd | 27.3 | bd | 13.3 | bd | bd | bd | 0.3 | 0.2 | bd |
| 3- olivine | 1.3 | | 60.3 | bd | 26.8 | bd | 12.5 | bd | bd | bd | 0.2 | bd | bd |
| 4- sulfide | 12.6 | | 24.8 | bd | 1.0 | bd | 1.9 | bd | 30.9 | bd | bd | 39.2 | 1.9 |
| 5- altered sulfide | 24.9 | | 62.0 | bd | 8.8 | 0.3 | 10.6 | bd | 5.5 | 0.3 | bd | 11.7 | 0.5 |
| 6- sulfide | 2.8 | | 5.5 | bd | 0.4 | bd | 0.9 | bd | 36.7 | bd | bd | 23.2 | 33.2 |
| 7- sulfide | 7.0 | | 12.0 | bd | 1.5 | bd | 1.9 | bd | 34.5 | bd | bd | 21.0 | 28.9 |
| 8- sulfide | 7.1 | | 13.9 | bd | 1.2 | 0.3 | 1.9 | bd | 38.8 | bd | bd | 42.1 | 1.6 |
| | | | | | | | | | | | | | |
| **Grain A0064-FO021** | | | | | | | | | | | | | |
| 9- phyllo nodule | 7.0 | | 61.7 | 0.5 | 15.0 | 1.8 | 14.1 | bd | 1.3 | bd | bd | 5.3 | bd |
| 10- C-rich nodule | | 68.3 | 19.0 | 1.2 | 2.4 | bd | 2.6 | bd | 2.4 | bd | bd | 3.3 | 0.6 |
| 11- C-rich nodule | | 86.7 | 10.0 | 0.6 | 0.6 | bd | 0.6 | bd | 1.0 | bd | bd | 0.4 | bd |
| 12- cg-phyllos | 12.6 | | 66.4 | 0.8 | 13.3 | 0.3 | 12.6 | bd | 1.3 | bd | bd | 4.7 | 0.2 |
| 13- porous-fibrous matrix | 20.0 | | 64.5 | 0.8 | 12.2 | 0.8 | 11.9 | bd | 1.8 | bd | bd | 7.1 | 0.4 |
| 14- compact matrix | 15.2 | | 63.9 | 0.6 | 11.8 | 0.2 | 11.4 | bd | 3.5 | bd | bd | 7.8 | 0.5 |
| 15- phyllo around apatite | 4.0 | | 65.4 | 0.4 | 15.7 | 1.4 | 12.9 | bd | 0.4 | bd | bd | 3.5 | bd |
| 16- apatite | 6.8 | | 61.8 | 1.4 | 0.6 | bd | 0.6 | 12.3 | bd | 22.6 | 0.4 | 0.2 | bd |
| 17- rectangular olivine | 1.3 | | 58.9 | bd | 27.3 | bd | 12.9 | bd | bd | bd | bd | 0.2 | bd |

associated to a rough FeNi-rich metal mineral (FeNi-G7) reported in ternary diagram Fig. 4 – along the taenite solid solution and 2/ another sulfide has an chemical composition near (Fe, Ni)$_3$S$_2$. Such chemical compositions were also observed within the sub-μm sulfides. Nano-sulfides tend to form clusters heterogeneously distributed in the matrix, alternating with sulfide-poor regions where nanosulfides are absent or isolated. TEM observations of the small sulfides reveal the presence of both pyrrhotite and Ni-rich sulfides but also of grains that are heterogeneous with a Ni-rich sulfide composition for a part of the grain, and a pyrrhotite-rich composition for the other part of the grain (Fig. S3). Some sulfides are euhedral (Fig. S3), whereas others show different features of alteration (Fig. 8). Some pyrrhotite and Ni-rich sulfides that

**Table 3**

Composition (at%) of different areas of sections A0064-FO019, A0064-FO021 and C002-FO019 extracted from EDS-hyperspectral maps obtained in STEM mode using the Titan 300 keV TEM. The locations of the different areas are indicated by numbered white rectangles on all figures except for analyses of section A0064-FO021 map 10. The latter correspond to the analyses of different parts of a C-rich nanosphere. The carbon content is indicated for low-C (LC) phases but does not contribute to the totals. It is reported for C-rich phases, where it contributes to the totals. Analyses with low-counts are reported to give indications about the analysed phases.

| | | C ind | C | O | Na | Mg | Al | Si | P | S | Ca | Mn | Fe | Ni |
|---|---|---|---|---|---|---|---|---|---|---|---|---|---|---|
| **Grain A0064-FO019** | | | | | | | | | | | | | | |
| **MAP 1** | | | | | | | | | | | | | | |
| 1 - sulfide | | 14.0 | | 16.2 | 0.2 | 2.8 | 0.5 | 5.0 | 0.0 | 36.0 | 0.2 | 0.2 | 38.4 | 0.6 |
| 4 - fg matrix | | 9.7 | | 58.5 | 0.7 | 13.1 | 2.5 | 21.6 | 0.0 | 0.1 | 0.0 | 0.1 | 3.2 | 0.2 |
| 6 - sulfide | | 0.0 | | 12.9 | 0.2 | 2.2 | 0.6 | 3.9 | 0.0 | 40.5 | 0.1 | 0.0 | 39.4 | 0.4 |
| 11 – fg matrix | | 17.5 | | 60.4 | 1.1 | 10.7 | 2.7 | 20.4 | 0.0 | 1.2 | 0.0 | 0.1 | 3.1 | 0.4 |
| **MAP 2** | | | | | | | | | | | | | | |
| 3 - cg phyllos | | 6.5 | | 62.4 | 0.5 | 14.6 | 1.7 | 17.5 | 0.0 | 0.3 | 0.0 | 0.0 | 3.0 | 0.1 |
| 5 - cg-phyllos | | 3.5 | | 61.4 | 0.7 | 15.4 | 1.8 | 17.6 | 0.0 | 0.2 | 0.0 | 0.1 | 2.8 | 0.0 |
| 6 - fg-phyllos | | 14.4 | | 60.8 | 1.0 | 10.4 | 2.9 | 19.3 | 0.0 | 1.2 | 0.0 | 0.0 | 4.0 | 0.3 |
| 7 - cg-phyllos | | 3.3 | | 62.6 | 0.6 | 15.4 | 1.6 | 16.9 | 0.1 | 0.2 | 0.0 | 0.0 | 2.7 | 0.0 |
| 9 - cg-phyllos | LC | 4.0 | | 61.9 | 0.7 | 15.6 | 1.2 | 17.5 | 0.0 | 0.1 | 0.0 | 0.0 | 3.1 | 0.0 |
| 11 – cg-phyllos | | 6.3 | | 62.0 | 0.6 | 15.4 | 1.7 | 17.5 | 0.0 | 0.1 | 0.0 | 0.0 | 2.6 | 0.1 |
| 12 - fg-phyllos | | 15.6 | | 61.5 | 1.1 | 11.0 | 2.8 | 18.0 | 0.2 | 1.4 | 0.0 | 0.1 | 3.8 | 0.3 |
| 18 - C-rich nodule | LC | | 81.7 | 14.8 | 1.5 | 0.2 | 0.7 | 0.4 | 0.0 | 0.5 | 0.0 | 0.0 | 0.1 | 0.0 |
| **MAP 3 – fg-phyllos** | | | | | | | | | | | | | | |
| 1- fg phyllos | | 11.7 | | 64.7 | 0.3 | 10.5 | 1.9 | 19.0 | 0.0 | 0.9 | 0.0 | 0.0 | 2.4 | 0.3 |
| **MAP 4 – cg-phyllos** | | | | | | | | | | | | | | |
| 3- cg-phyllos | | 7.2 | | 57.5 | 0.6 | 16.1 | 1.5 | 20.2 | 0.1 | 0.2 | 0.1 | 0.0 | 3.7 | 0.1 |
| **Grain C002-FO019** | | | | | | | | | | | | | | |
| **MAP 2 - spiral sulfide** | | | | | | | | | | | | | | |
| 1 - core | LC | | 59.6 | 29.5 | 0.0 | 3.1 | 0.0 | 5.7 | 0.0 | 0.8 | 0.1 | 0.0 | 1.2 | 0.0 |
| 2 - global | LC | 12.9 | | 59.8 | 0.5 | 12.5 | 1.9 | 7.5 | 0.0 | 7.0 | 0.3 | 0.2 | 10.3 | 0.0 |
| 7- NiFeS-rich spiral | LC | 27.7 | | 50.2 | 0.0 | 2.3 | 0.0 | 0.4 | 0.0 | 17.2 | 0.0 | 0.0 | 28.6 | 1.3 |
| 8 - FeS-rich spiral | LC | 6.5 | | 61.1 | 0.3 | 11.5 | 1.4 | 5.2 | 0.0 | 7.9 | 0.8 | 0.4 | 11.4 | 0.0 |
| 9 - matrix | LC | 3.7 | | 71.9 | 0.0 | 8.6 | 2.1 | 15.1 | 0.0 | 0.5 | 0.1 | 0.0 | 1.5 | 0.2 |
| **MAP 3** | | | | | | | | | | | | | | |
| 10 - olivine | | 0.0 | | 63.2 | 0.1 | 23.6 | 0.1 | 12.7 | 0.0 | 0.0 | 0.0 | 0.1 | 0.1 | 0.0 |
| **MAP 6 - altered sulfide** | | | | | | | | | | | | | | |
| 1 - pyrrhotite | | 0.0 | | 8.8 | 0.0 | 0.4 | 0.0 | 1.2 | 0.0 | 41.1 | 0.0 | 0.1 | 47.6 | 0.9 |
| 3 - pyrrhotite | | 12.7 | | 13.1 | 0.0 | 0.2 | 0.0 | 1.9 | 0.0 | 36.0 | 0.3 | 0.7 | 45.4 | 1.9 |
| 4 - matrix | | 9.2 | | 62.3 | 0.6 | 13.7 | 1.8 | 16.5 | 0.1 | 1.1 | 0.0 | 0.1 | 3.8 | 0.2 |
| 5 - matrix | | 10.9 | | 58.9 | 0.6 | 12.1 | 2.3 | 17.8 | 0.0 | 0.8 | 0.1 | 0.2 | 7.0 | 0.2 |
| 6 - sulfide | | 0.0 | | 15.7 | 0.0 | 0.0 | 0.0 | 0.6 | 0.0 | 34.4 | 0.2 | 0.0 | 46.8 | 2.3 |
| 8 - altered sulfide | LC | 0.0 | | 51.5 | 0.0 | 5.3 | 0.0 | 0.0 | 0.0 | 10.5 | 1.0 | 0.0 | 30.3 | 1.4 |
| 9 -altered sulfide | | 17.8 | | 57.7 | 0.8 | 9.0 | 1.9 | 13.7 | 0.1 | 4.1 | 0.5 | 0.0 | 11.9 | 0.4 |
| **MAP 7 - altered sulfide part 2** | | | | | | | | | | | | | | |
| 2 - matrix | LC | 8.7 | | 59.1 | 1.3 | 15.1 | 2.6 | 16.5 | 0.0 | 1.3 | 0.0 | 0.0 | 3.9 | 0.3 |
| 5 - altered sulfide | LC | 0.0 | | 18.0 | 3.0 | 9.0 | 2.9 | 8.3 | 0.0 | 15.0 | 0.0 | 2.0 | 39.9 | 2.1 |
| **MAP 9 - core sulfide** | | | | | | | | | | | | | | |
| 1- core | LC | 3.9 | | 4.8 | 0.0 | 0.0 | 0.3 | 0.1 | 0.0 | 15.7 | 0.0 | 0.0 | 63.7 | 15.4 |
| 3 - core | | 10.2 | | 7.0 | 0.0 | 0.0 | 0.0 | 0.4 | 0.0 | 21.8 | 0.0 | 0.0 | 54.5 | 16.3 |
| 4 - sulfide | | 0.0 | | 5.6 | 0.0 | 0.1 | 0.0 | 0.9 | 0.1 | 40.8 | 0.1 | 0.1 | 32.2 | 20.2 |
| 6 - sulfide | | 4.6 | | 6.6 | 0.3 | 0.2 | 0.1 | 0.5 | 0.0 | 37.8 | 0.3 | 0.0 | 26.1 | 28.1 |
| 8 - global | | 0.3 | | 6.8 | 0.0 | 0.2 | 0.0 | 0.8 | 0.0 | 38.8 | 0.0 | 0.0 | 34.8 | 18.7 |
| 10 - sulfide rim | | 10.5 | | 20.2 | 0.0 | 1.6 | 0.5 | 2.1 | 0.0 | 34.4 | 0.1 | 0.0 | 39.9 | 1.2 |
| **MAP 10 - pyrrhotite** | | | | | | | | | | | | | | |
| 1- pyrrhotite | | 2.8 | | 8.7 | 0.0 | 0.5 | 0.0 | 1.3 | 0.0 | 45.3 | 0.0 | 0.0 | 43.5 | 0.6 |
| 2 - Ni-rich rim | LC | 1.7 | | 9.0 | 0.6 | 0.0 | 0.0 | 0.0 | 0.0 | 42.0 | 0.2 | 0.0 | 25.0 | 23.1 |
| 3 - pyrrhotite | | 3.0 | | 8.6 | 0.2 | 0.2 | 0.5 | 1.0 | 0.0 | 45.5 | 0.0 | 0.1 | 43.1 | 0.9 |
| 6 - pyrrhotite | | 3.1 | | 6.5 | 0.4 | 0.4 | 0.1 | 0.4 | 0.0 | 44.0 | 0.0 | 0.0 | 47.6 | 0.8 |
| **MAP 12 - global** | | | | | | | | | | | | | | |
| 1 - pentlandite | | 5.1 | | 16.0 | 0.0 | 1.4 | 0.2 | 2.4 | 0.0 | 33.4 | 0.0 | 0.1 | 21.1 | 25.3 |
| 2 - sulfide | | 1.8 | | 13.3 | 0.0 | 2.0 | 0.5 | 1.8 | 0.0 | 38.5 | 0.0 | 0.2 | 43.2 | 0.5 |
| 5- olivine | | 0.5 | | 58.5 | 0.1 | 26.7 | 0.1 | 14.2 | 0.0 | 0.0 | 0.0 | 0.3 | 0.1 | 0.0 |
| 7 - olivine | | 1.4 | | 60.1 | 0.1 | 25.9 | 0.1 | 13.1 | 0.0 | 0.0 | 0.1 | 0.3 | 0.3 | 0.0 |
| 9 - sulfide | | 5.3 | | 26.0 | 0.0 | 5.1 | 1.0 | 5.4 | 0.0 | 29.8 | 0.0 | 0.1 | 31.8 | 0.8 |
| **Grain A0064-FO021** | | | | | | | | | | | | | | |
| **MAP 1- phosphate zone** | | | | | | | | | | | | | | |
| 1- matrix | LC | 2.7 | | 64.3 | 0.2 | 15.5 | 1.4 | 15.4 | 0.0 | 0.2 | 0.1 | 0.0 | 2.9 | 0.0 |
| 2 - phosphate | | 11.0 | | 50.3 | 1.5 | 0.5 | 0.1 | 1.1 | 16.0 | 0.0 | 29.9 | 0.4 | 0.2 | 0.0 |
| 5 - phosphate + alteration | | 9.5 | | 55.3 | 0.8 | 7.3 | 0.4 | 8.6 | 8.4 | 0.6 | 16.4 | 0.1 | 1.9 | 0.1 |
| **MAP 2- phosphate zone** | | | | | | | | | | | | | | |
| 1 – cg-phyllos | | 2.9 | | 64.0 | 0.2 | 15.9 | 1.3 | 15.2 | 0.0 | 0.2 | 0.1 | 0.0 | 3.0 | 0.0 |
| 3 - fg-phyllos | | 3.2 | | 63.9 | 0.4 | 13.5 | 1.7 | 15.0 | 0.0 | 0.8 | 0.0 | 0.1 | 4.6 | 0.1 |
| **MAP 3 - sulfide** | | | | | | | | | | | | | | |
| 1 - pyrrhotite int | | 3.1 | | 6.2 | 0.0 | 0.0 | 0.0 | 1.2 | 0.0 | 48.4 | 0.0 | 0.0 | 43.6 | 0.5 |
| 3 - pyrrhotite rim | | 2.5 | | 5.8 | 0.0 | 0.2 | 0.0 | 0.8 | 0.0 | 48.4 | 0.0 | 0.0 | 44.4 | 0.4 |
| 4 - sulfide | | 14.4 | | 26.6 | 0.0 | 4.4 | 0.7 | 3.9 | 0.0 | 30.5 | 0.0 | 0.0 | 17.1 | 16.8 |

**Table 3** (*continued*)

|  | C ind | C | O | Na | Mg | Al | Si | P | S | Ca | Mn | Fe | Ni |
|---|---|---|---|---|---|---|---|---|---|---|---|---|---|
| 5 - matrix | 5.2 |  | 67.6 | 0.4 | 12.9 | 1.5 | 13.8 | 0.0 | 0.3 | 0.0 | 0.0 | 3.4 | 0.0 |
| **MAP 4 - sulfide/phosphide** |  |  |  |  |  |  |  |  |  |  |  |  |  |
| 1- (Fe.Ni)$_2$P | 2.4 |  | 4.6 | 0.0 | 0.0 | 0.3 | 0.8 | 31.3 | 1.3 | 0.0 | 0.0 | 15.3 | 46.4 |
| 2 - pyrrhotite | 2.6 |  | 5.6 | 0.0 | 0.0 | 0.0 | 0.4 | 0.0 | 49.6 | 0.0 | 0.1 | 43.8 | 0.5 |
| 3 - matrix | 5.2 |  | 67.8 | 0.1 | 11.7 | 1.5 | 12.1 | 0.0 | 1.4 | 0.1 | 0.1 | 5.0 | 0.1 |
| **MAP 7 - global zone** |  |  |  |  |  |  |  |  |  |  |  |  |  |
| 1 - pentlandite | 0.0 |  | 5.9 | 0.0 | 0.5 | 0.3 | 1.4 | 0.0 | 43.7 | 0.1 | 0.1 | 25.5 | 22.4 |
| 2 - pyrrhotite | 0.0 |  | 22.9 | 0.2 | 0.5 | 0.4 | 1.0 | 0.0 | 35.8 | 0.0 | 0.1 | 37.1 | 1.9 |
| 7 - pentlandite | 6.4 |  | 24.6 | 0.4 | 4.7 | 0.8 | 7.5 | 0.0 | 27.7 | 0.1 | 0.0 | 16.0 | 18.2 |
| 8 - pyrrhotite | 2.7 |  | 25.5 | 0.0 | 4.2 | 0.8 | 5.9 | 0.0 | 31.9 | 0.0 | 0.0 | 30.8 | 0.9 |
| 5- C rich zone |  | 63.8 | 22.7 | 1.4 | 2.6 | 1.8 | 3.5 | 0.0 | 1.9 | 0.3 | 0.0 | 1.8 | 0.1 |
| 14 - phyllos | 4.5 |  | 62.0 | 0.3 | 15.0 | 1.8 | 15.9 | 0.0 | 0.7 | 0.0 | 0.0 | 4.2 | 0.1 |
| 10- Ca inclusions |  | 24.1 | 39.4 | 1.2 | 7.2 | 0.9 | 8.5 | 0.1 | 7.4 | 2.8 | 0.1 | 6.8 | 1.2 |
| **MAP 8 - rectangular olivine** |  |  |  |  |  |  |  |  |  |  |  |  |  |
| 1 - olivine | 0.1 |  | 55.8 | 0.0 | 28.7 | 0.1 | 15.1 | 0.0 | 0.0 | 0.0 | 0.1 | 0.1 | 0.0 |
| 3 - olivine | 0.2 |  | 55.3 | 0.0 | 29.1 | 0.1 | 15.2 | 0.0 | 0.0 | 0.0 | 0.1 | 0.1 | 0.0 |
| **MAP 9- C rich nodule** |  |  |  |  |  |  |  |  |  |  |  |  |  |
| 1- C-rich nodule |  | 80.4 | 15.3 | 0.6 | 0.6 | 0.8 | 0.7 | 0.0 | 1.3 | 0.0 | 0.0 | 0.2 | 0.0 |
| **MAP 10 - C rich nodule** |  |  |  |  |  |  |  |  |  |  |  |  |  |
| 1- C-rich nodule |  | 79.9 | 15.7 | 1.2 | 0.1 | 0.7 | 0.3 | 0.0 | 2.0 | 0.0 | 0.0 | 0.1 | 0.0 |
| 2- C-rich nodule |  | 81.6 | 14.3 | 1.0 | 0.2 | 0.7 | 0.3 | 0.0 | 1.8 | 0.0 | 0.0 | 0.1 | 0.0 |
| **MAP 11 -** |  |  |  |  |  |  |  |  |  |  |  |  |  |
| 1 - pyrrhotite | 0.0 |  | 2.2 | 0.0 | 0.0 | 0.0 | 0.5 | 0.0 | 48.8 | 0.0 | 0.1 | 47.8 | 0.7 |
| 4 - altered rim | 0.0 |  | 3.5 | 0.0 | 0.1 | 0.0 | 0.5 | 0.1 | 48.3 | 0.0 | 0.1 | 46.7 | 0.8 |
| 5 - Ni rich rim | 6.7 |  | 12.6 | 0.0 | 0.3 | 0.0 | 0.5 | 0.0 | 40.4 | 0.2 | 0.2 | 28.6 | 17.2 |
| 7 - Ni rich rim | 4.3 |  | 24.9 | 0.0 | 3.3 | 0.8 | 4.3 | 0.0 | 31.1 | 0.0 | 0.0 | 28.1 | 7.5 |
| 8 - altered rim | 2.0 |  | 6.5 | 0.0 | 0.2 | 0.0 | 0.6 | 0.0 | 45.8 | 0.1 | 0.0 | 45.1 | 1.5 |
| 11 - matrix | 3.8 |  | 61.0 | 0.2 | 12.9 | 2.2 | 15.2 | 0.1 | 1.7 | 0.0 | 0.1 | 6.4 | 0.2 |

were initially euhedral show engulfment indicative of dissolution (Fig. 8 a, b, c). EDS analyses of those sulfides are reported in a Fe-S-Ni ternary diagram (Fig. 4) and show that both pyrrhotite and Ni-rich sulfides are depleted in S and that some sulfides are highly enriched in Ni.

Another pyrrhotite-type sulfide shows features of alteration with the sulfide becoming progressively porous and fibrous (Fig. 8 d, e, f and associated maps 6 and 7). Part of it is completely replaced by a mixture of Si-Mg rich material mixed with more Fe-S-Ni rich fibrous material. Another Ni-rich sulfide shows 1/ an altered rim of Ni-poor pyrrhotite-type composition and 2/ a central core enriched in C, Fe, Ni and depleted in S (Fig. 9 a, b, c, d).

Finally, an unusual cluster of 20 nm-sized concentrically layered nodules with a carbon-rich core was observed (Fig. 9e), sometimes associated with a spiral shaped linear structure. The concentrically layered structures (Fig. 9f) are globally enriched in Fe-S-Mg and O. They show alternating layers of heavy material (potentially Fe and S) and more light material (potentially Mg-rich material). These layers show a very low content in Ni although Ni can be present in the spiral-shaped linear (Fe-Mg-S rich) structures that are associated to the nodules. The cores of those nodules are highly enriched in C and show also a lower concentration in O than the layered structures (Fig. 9g and h, Table 3).

Numerous 500 nm to 1.5 μm sized magnetite are observed with a larger abundance in the right part of the section. Rounded, partly euhedral, euhedral and plaquette magnetite were observed (Fig. 5). SEM-EDS analyses reported in Table 1 show a O/Fe ratio above that of magnetite (4/3) due to O-rich matrix contamination. A Si versus O/Fe correlation gives a O/Fe ratio of the analyzed magnetite of 1.38. One ~ 500 nm sized calcite grain was observed (Fig. 5). Map 12 in Fig S3 reveals that Ca-rich nm-sized regions are also heterogeneously distributed within the matrix. We were not able to identify the corresponding phases.

Relatively large (up to 500 nm) C-rich zones were observed at SEM scale (Fig. 5) but only one C-rich nanosphere was observed at TEM scale. In addition, carbon map shows a diffuse distribution of carbon at small scale in the section (e.g. Fig. S3). Due to the small size of the C-rich zones, their EDS-SEM analyses are contaminated by X-ray signals from the surrounding areas.

### 3.1.3. Fragment A0064-FO021

The thick section of fragment A0064-FO021 is approximately of 40 μm length over 15 to 4.5 μm height (Fig. 10). It shows a completely different texture from A0064-FO019 and C0002-FO019 with the presence of two different regions: one with a relatively compact very fine-grained matrix (delimited by a yellow border on Fig. 10) and one with a very porous, fractured fibrous matrix. Numerous minerals are also observed and will be described in the following: carbonates, olivines, phosphates and magnetites. The compact fine-grained matrix seems to be less crystallized than the fibrous porous matrix, but they have similar compositions (Fig. 11a and b, analyses 13 and 14 in Table 2). Saponite and serpentine-type phyllosilicates were observed in the fibrous matrix with an interlayer width of 1 nm and 0.7 nm. At the several micrometer scale, the compositions of the porous and compact matrices are different (see Table 1, analyses of zone Z4 or Z5 and Z3, Fig. 10) with a higher (Fe + S)/Si ratio (~2.5 and 1.5 respectively) in the porous matrix related to its higher content in sulfide and a higher C content in the porous matrix (up to 2 times richer). In the fibrous porous region, some cg-phyllos were observed but with a relatively limited patch size (<1 μm) (Fig. S4). A few observed interlayer widths (around 7 Å) suggest that the observed cg-phyllos is from the serpentine phyllosilicate family. Local STEM analyses of the matrix reveal content in Fe around 3–4 at%. They are reported in a Si+Al-Fe-Mg ternary diagram and lie between the saponite solid solution line and the serpentine solid solution line with an enrichment toward the Fe endmember. The composition of cg-phyllos is close to that of cg-phyllos from A0064-FO019 and the composition of the fg-phyllos is close to that of fg-phyllos from A0064-FO019. The Na and Al contents of fg- and cg-phyllos are around 0.5 and 1–2 at%.

Two large olivine minerals were observed in the porous matrix, one (~2 μm) is anhedral whereas the other shows a rectangular shape of 2 by 1 μm (Fig. 11g). Both have an extremely low content of Fe (<0.5 at%) (see SEM-EDS analyses in Table 1 and TEM analyses 17 in Table 2).

Two different phosphate minerals were also observed in the porous matrix. One, (Pho-8 in Fig. 10) only observed by SEM, is about 2 by 1 μm large and is surrounded by cracks. Its EDS composition showing P, Na, Ca, Fe, S, Mg and Si reveals 1/ that the phosphate is either very thin and/ or mixed with the matrix, 2/ that it is a Na-rich phosphate. The second phosphate grain (Pho-1 in Fig. 10) is larger (2 × 2 μm) but its TEM
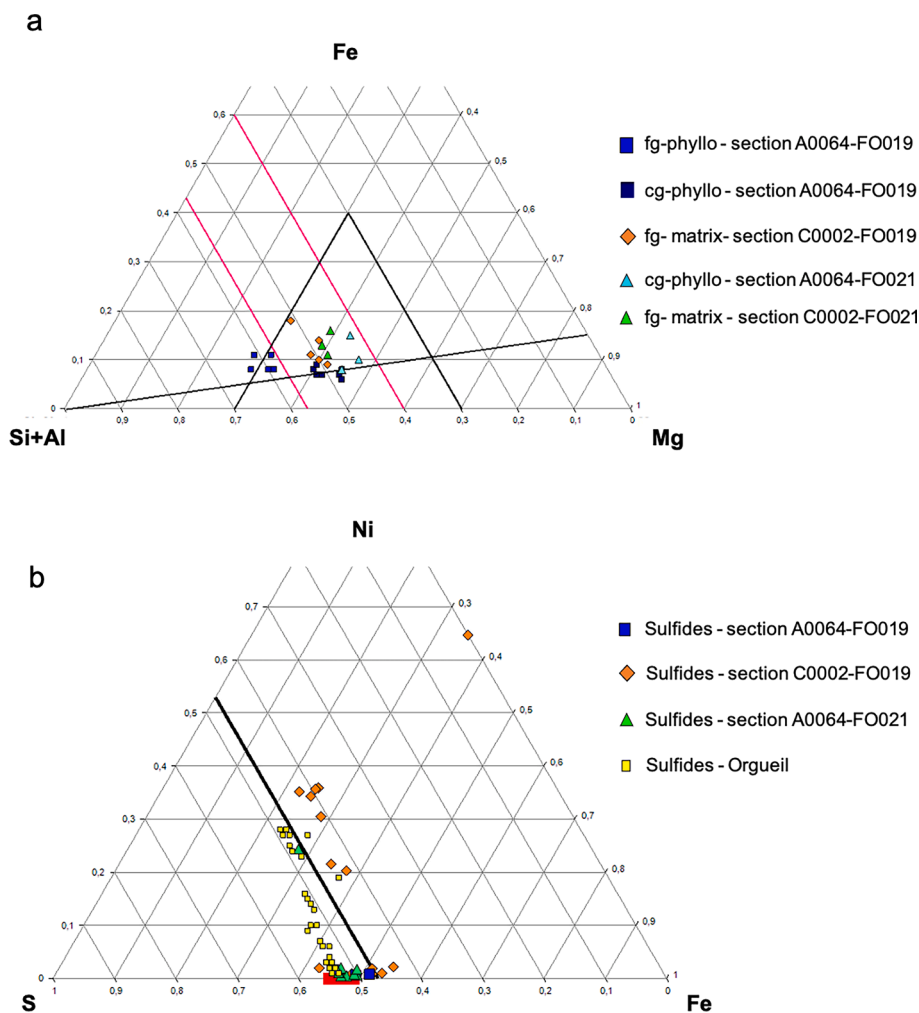
**Fig. 4.** a) Si+Al-Fe-Mg ternary diagram showing individual TEM/EDS analyses of fg-phyllos, cg-phyllos and fine-grained matrix from sections A0064-FO019, A0064-FO021, C0002-FO019. Additional SEM/EDS analyses of cg-phyllos were added when possible. To minimize the contamination of the matrix/phyllosilicates analyses by the nanosulfides, matrix/phyllosilicates analyses with >1,2 at% S were discarded. The upper bold pink line corresponds to the Mg–Fe serpentine solid solution and the lower bold pink line to the Mg–Fe smectite solid solution. The black triangle is similar to that in Fig. 10 from Tomeoka and Buseck (1988) where TEM/EDS analyses of phyllosilicate from Orgueil are reported. The black line is defined by a Fe/(Mg + Fe) = 15 atomic % as in Tomeoka and Buseck (1988). b) Fe–Ni–S ternary diagram showing individual TEM/EDS and SEM/EDS analyses of sulfides from sections A0064-FO019, A0064-FO021, C0002-FO019. Analyses of sulfides are only reported when contamination by adjacent matrix was minimal (e.g. O < 10 at%, very low content in Mg and Si). EPMA analyses of sulfides from Orgueil (Berger et al., 2016) are shown for comparison. The red bold line corresponds to the pyrrhotite solid solution and the black bold line to the pentlandite ([Fe,Ni]$_9$S$_8$) solid solution.

observation reveals that it is composed of several smaller euhedral minerals (Fig. 12b). This phosphate aggregate is walled on one side by a 500 nm width rim of cg-phyllos free of sulfide grains that is surrounded by the porous sulfide-rich fibrous matrix (see Fig. 12c). This Ca-phosphate shows a low content of Na and Fe (2 and 2.4 at% respectively, analyses 8 in Table 1, Fig. 12a). Part of Fe is related to a minor contribution of the matrix in the analyses. Indeed, STEM-EDS map (Fig. 12d) reveals 1/ presence of matrix-rich material (Mg, Si, Fe-rich material) between the grains and 2/ presence of alteration features within the phosphate minerals.

Two large calcites (from 1 to 2 μm) were observed in the left part of the section (in the same region as the olivines) within the porous fibrous matrix. Map 7 in Fig S5 reveals that Ca-rich nm-sized regions are also heterogeneously distributed within the matrix. We were not able to identify the corresponding phases. In addition, several large (1 μm) isolated euhedral magnetite grains were observed in both the porous fibrous and the compact matrix.

Large pyrrhotite minerals were observed (up to 2 μm) in addition to numerous pyrrhotite and Ni-rich sulfides dispersed in both the porous

and the compact matrix. Fig. S5 show that Ni-rich sulfides, pyrrhotites and Ni- and Fe- zoned sulfides can be present within a 1 μm large region (analyses 1, 2, 7 and 8 in Table 3, map 7). SEM and TEM observations show also the presence of pyrrhotite with alteration features. For example, Fig. 11h and i show a pyrrhotite with a rim containing Ni-rich lamellae, whose limits seem to follow a particular crystallographic orientation, suggesting exsolution. The rim is porous and vesiculated (Fig. 11h). Diffraction of the vesiculated rim and the center of the grain point toward a 4C pyrrhotite structure. Finally, a P, Fe and Ni-rich but O-depleted mineral (100 by 200 nm sized) was observed in contact with a large (~1 μm) pyrrhotite showing a "porous" rim (limits in red in Fig. 13a). This mineral seems to be composed of several crystals. Local STEM analyses give a stoichiometry of (Fe,Ni)$_2$P, which could be compatible with one of the stoichiometric polymorphs, allabogdanite or barringerite, but no crystallographic identification was made.

Diffuse carbon and relatively large (up to 1 μm) C-rich zones were observed at the SEM scale (Fig. 10) in the porous matrix. Some C-rich nodules (200–300 nm) were observed by TEM both in the compact and in the porous matrix (Fig. 11d and e and Fig. 11f, for the compact and the
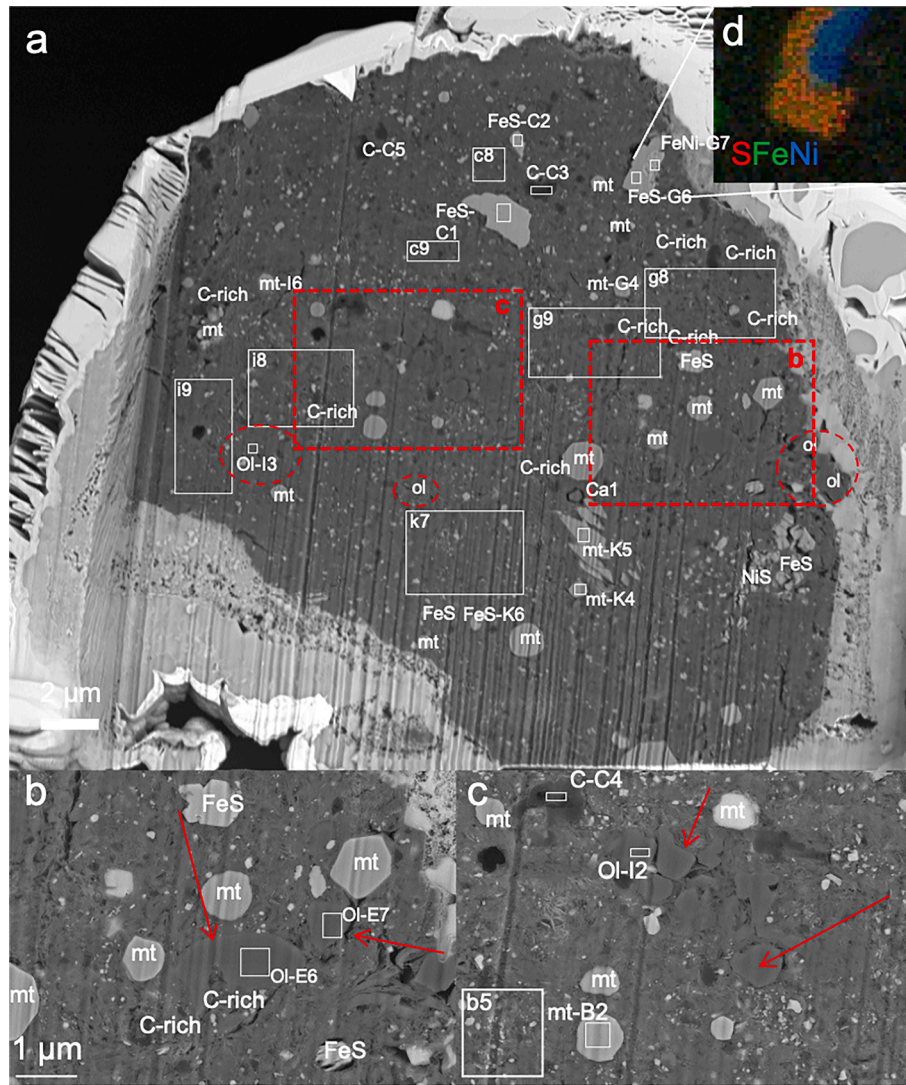
**Fig. 5.** BSE images of a) the thick slice extracted from grain C0002-FO019. The white layers surrounding the section corresponds to the platinum deposit. b and c) details of the two largest olivine-rich areas shown by the two red boxes in (a). Scale is similar on b and c. Red arrows indicate the sub-µm sized olivines. Red circled zones indicate additional olivine-rich zones. The numbered white rectangles correspond to zones analyzed by EDS (Table 1). The indicated minerals were identified by X-ray analyses. Some are reported in Table 1. d) composite X-ray map of S (red), Fe (green) and Ni (blue) of the Fe-Ni-rich minerals. Abbreviations: mt for magnetite, Ol for olivine, FeS for sulfides and FeNi for metal, Ca for calcite.
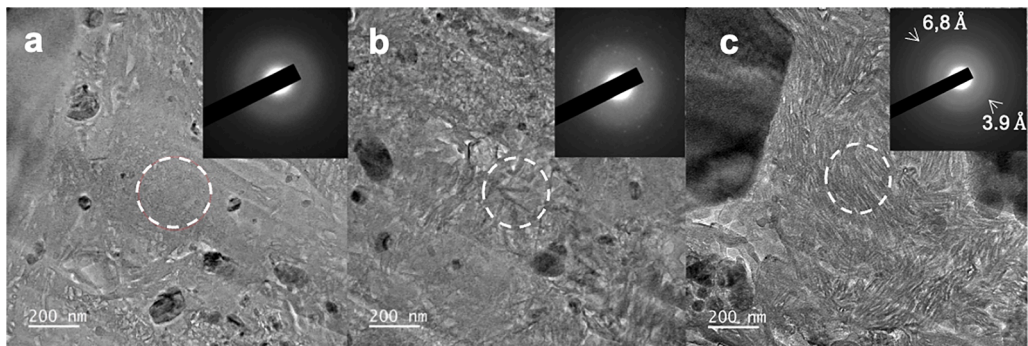


**Fig. 6.** (a–c) Bright field TEM images of different zones of section C0002-FO019 showing different degrees of crystallinity. The dotted white circles correspond to zones from which the reported diffractograms were acquired. In (a), the electron diffraction pattern shows large diffuse rings indicative of the amorphous nature of the material whereas in (b), the electron diffraction pattern shows more or less intense rings with spots and in (c) clear rings are visible. Numbers corresponds to d-spaces.
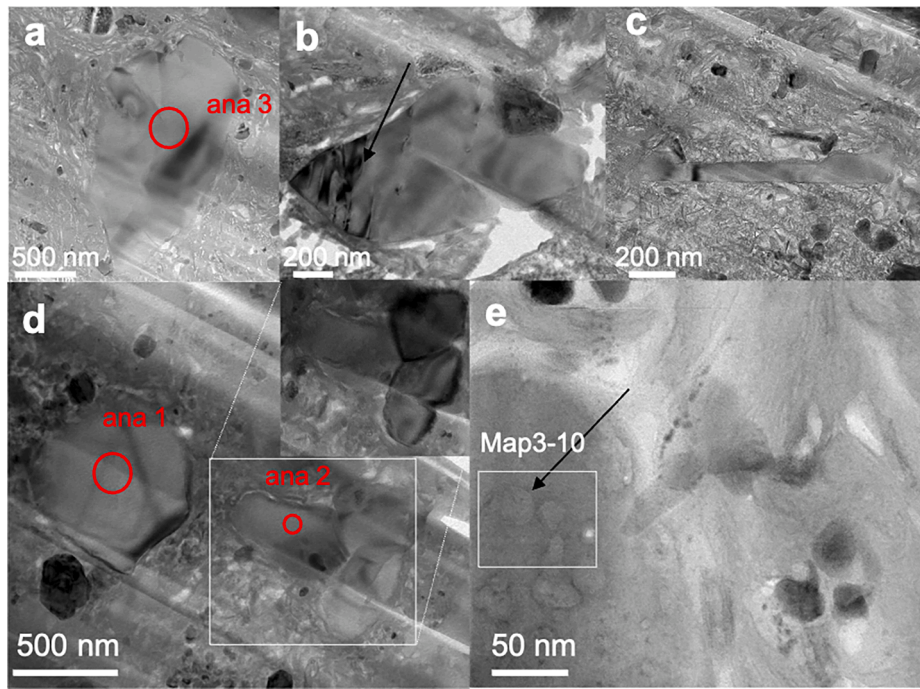
**Fig. 7.** Bright field TEM images of different olivines from section C0002-FO019. Black arrows indicate the presence of defects (b) and of pores inside the olivine (e). The white box in (d) shows the presence of a triple junction between three sub-μm olivines, also seen with a different tilt in the top right inset in (d). The numbered red circles indicate JEOL TEM analyses acquired in conventional mode (Table 2) and the white rectangles in (e) correspond to zones from which EDS analyses were extracted from the STEM-X-ray maps (Table 3).
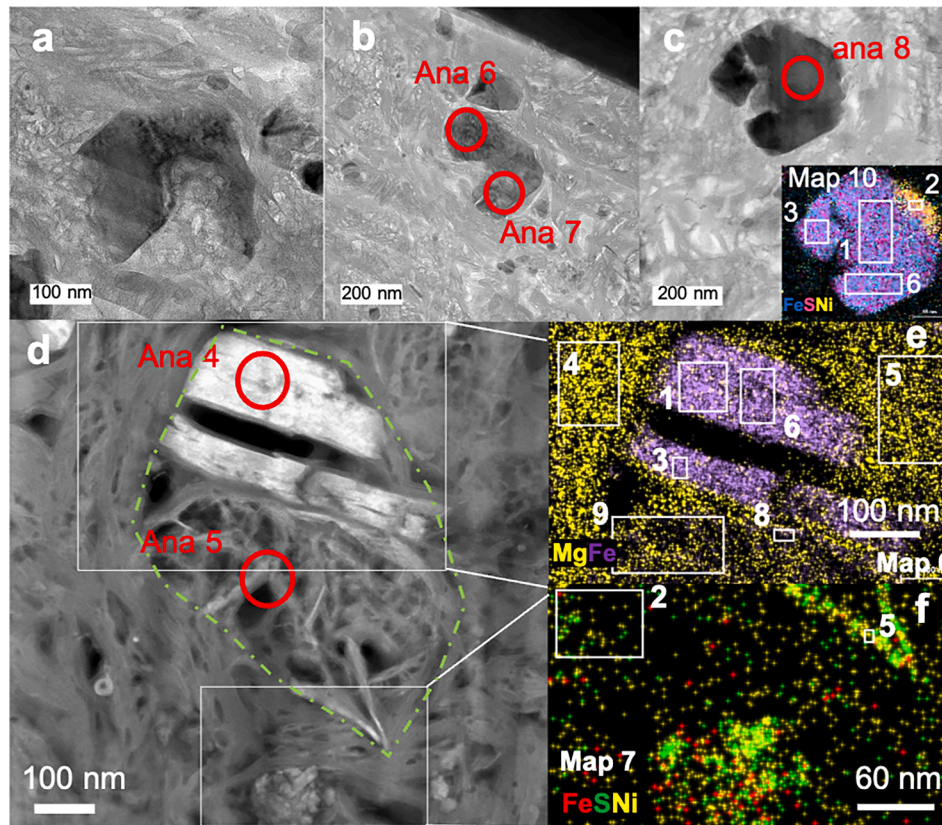


**Fig. 8.** (a–c) Bright field TEM images of three altered sulfides in section C0002-FO019. The bottom right insert in (c) shows the STEM composite X-ray map 10 of Fe (blue), S (pink) and Ni (yellow) of the sulfides. (d) DF-STEM of an altered sulfide in section C0002-FO019. (e) STEM composite X-ray map 6 of Mg (yellow) and Fe (purple) of the top part of the sulfide in (d) and (f) STEM composite x-ray map 7 of Fe (red), S (green) and Ni (yellow) of the bottom part of the sulfide (white boxes in (d) indicates the location of the two maps 6 and 7. The numbered red circles indicate JEOL TEM analyses acquired in conventional mode (Table 2), whereas the white rectangles correspond to zones from which EDS analyses were extracted from the STEM-X-ray maps 6, 7 for section C0002-FO019 (Table 3).
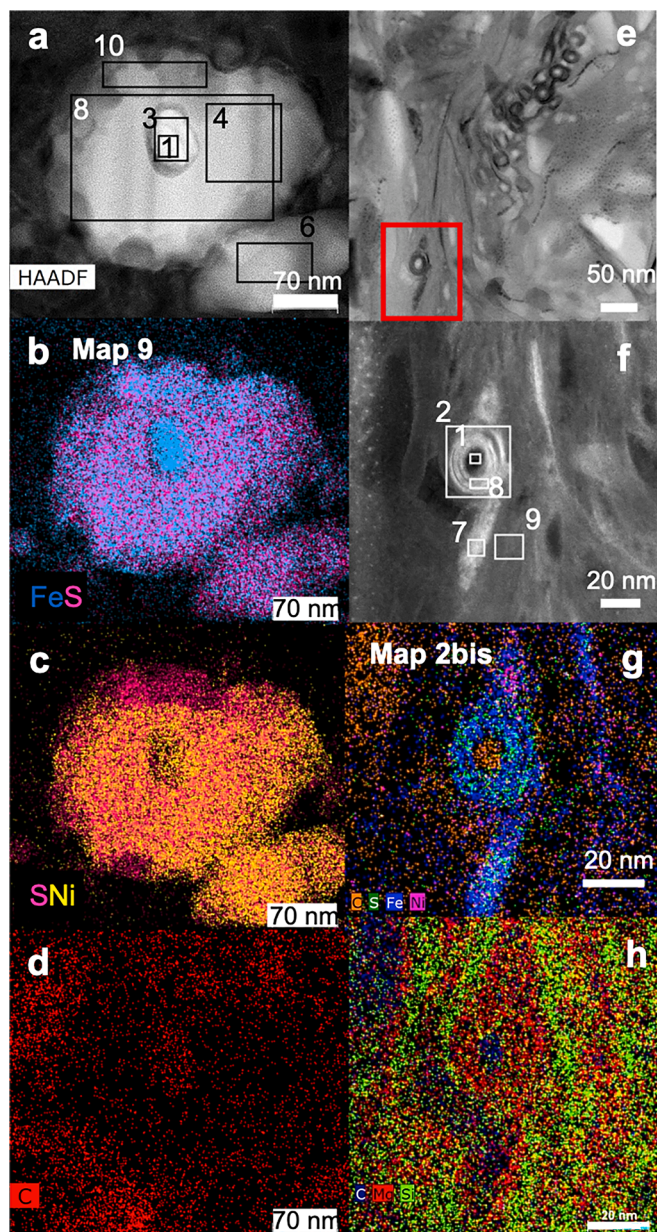
**Fig. 9.** (a) HAADF-STEM image and (b-d) STEM composite x-maps of Fe (blue) and S (pink) (b), of S (pink) and Ni (yellow) (c) and of C (red) (d) of a sulfide showing a C-bearing FeNi core in section C0002-FO019. (e) BF-STEM images of 20 nm-sized concentrically layered nodules with a carbon-rich core in section C0002-FO019, (f-h) HAADF-STEM image (f) and STEM composite X-ray maps of C (orange), S (green), Fe (purple), Ni (pink) (g) and of C (purple), Mg (red), Si (green) (h) of one of these nodules associated with a spiral shaped linear structure. The red box in the top left image (e) indicate the spiral-shaped nodule mapped in (g-h). White and black rectangles correspond to zones from which EDS analyses were extracted from the STEM-X-ray maps 9 and 2 bis (Table 3).

porous matrix respectively). No nanosphere with a central vesicle was observed in this section. Local TEM and STEM analyses of C-rich nodules are reported in Table 2 and 3 with a O/C ratio between 5 and 9. They also show one nodule with Na and S enrichments up to 1 and 2 at%, respectively.

## 3.2. IR characteristics of each slice

In the following, we will present first the main characteristics of the mean IR spectra of each section and then we will present the combined

results of the SEM and IR mapping of each section.

### 3.2.1. Mean spectra of slices from fragment A0064-FO019, C0002-FO019, A0064-FO021

The IR mean spectra of each section are reported in Fig. 14. Overall, the three sections show the presence of IR vibrational features characteristic of the presence of OM, ad- or absorbed water, phyllosilicate structural hydroxyls (M—OH), phosphates, and silicates. Detailed attribution of each band is given in Table 4 for each section.

Positions of the different vibrational bands are slightly different from those given in Dionnet et al. (2023) principally because the IR positions given in Dionnet et al., (2023) are extracted from the mean IR reflectance spectra of the whole surfaces of the fragments, whereas the position given in Table 4 are based on the IR transmission spectra of the 2.5 μm thick sections extracted from each corresponding bigger fragment. However, as shown below, the IR variability reported in Dionnet et al. (2023) between the three fragments is also found in the three sections.

### 3.2.2. IR/SEM combination results

For each section, we 1/ used the IR map of the section to better understand the variability of the IR signature over the section and 2/ combined the SEM images with the IR mapping in order to better understand this variability. For section A0064-FO021, the IR mapping of the section was not of a very good quality because of the thickness of the platinum compared with the height of the section. We thus focused on section from A0064-FO019 and C0002-FO019 grains. The IR spectrum over the map of grain C0002-FO019 does not show large differences at the probed pixel sizes except in regions richer in olivine. Fig. S6 shows the olivine band area distribution over the section, which is in relatively good agreement with the olivine distribution shown by the SEM-BSE image. One IR spectra of an olivine-rich region is shown for example. It shows a relatively intense 875 cm$^{-1}$ band indicative of the presence of the tiny olivines (Salisbury et al., 1991, Beck et al., 2014).

Both the IR spectra and SEM/TEM observations of section from A0064-FO019 show at a relatively large scale two different types of phyllosilicate structures (cg and fg-phyllos). In Fig. 15, in addition to the SEM-BSE image of the section (Fig. 15a), we report the distribution (Fig. 15b) of the ratio of the C—H bending (1330-1432 cm$^{-1}$ range) over the SiO stretching band areas (857–1154 cm$^{-1}$ range). This ratio is a proxy for the abundance of OM relative to silicates. The distribution (Fig. 15c) of the ratio of the C=O stretching (1685–1737 cm$^{-1}$ range) over the CH bending band areas (1330–1432 cm$^{-1}$ range), and the distribution of the C-O stretching (1230–1300 cm$^{-1}$ range) over the CH bending band areas are also reported (Fig. 15d). These ratios are used to study the spatial distribution of variabilities in chemical structures of the OM. We used CH bending at ~1400 cm$^{-1}$ instead of the stretching mode (~3000 cm-1) to be as close as possible to the spectral range of the C=O (~1700 cm$^{-1}$) and C-O stretching modes (~1260 cm$^{-1}$), and of the Si-O stretching mode (~1000 cm$^{-1}$). In this way, we get two advantages: 1/ we use a range of the spectrum where the signal to noise ratio is similar for the four bands, 2/ the diffraction of the IR light behaves similarly for the considered bands, minimizing potential diffraction artifacts and thus making the visualization and the comparison of the distribution of the different functionality of the OM more relevant. Zones with a low CH$_{bending}$/SiO$_{stretching}$ and high C=O$_{stretching}$/CH$_{bending}$ and C-O$_{stretching}$/CH$_{bending}$ ratios correspond to areas rich in cg-phyllos on SEM-BSE images whereas zones with a high CH$_{bending}$/SiO$_{stretching}$ and low C=O$_{stretching}$/CH$_{bending}$ and C-O$_{stretching}$/CH$_{bending}$ ratios correspond to areas rich in fg-phyllos in SEM-BSE images. Mean IR spectra of representative regions of each zone were extracted from the hyperspectral map (Fig. 15e). Spectrum 1 corresponds to that of a zone very rich in cg-phyllos whereas spectrum 2 corresponds to that of a zone very rich in fg-phyllos. The vibrational bands and their attributions for both spectra are given in Table 4H.
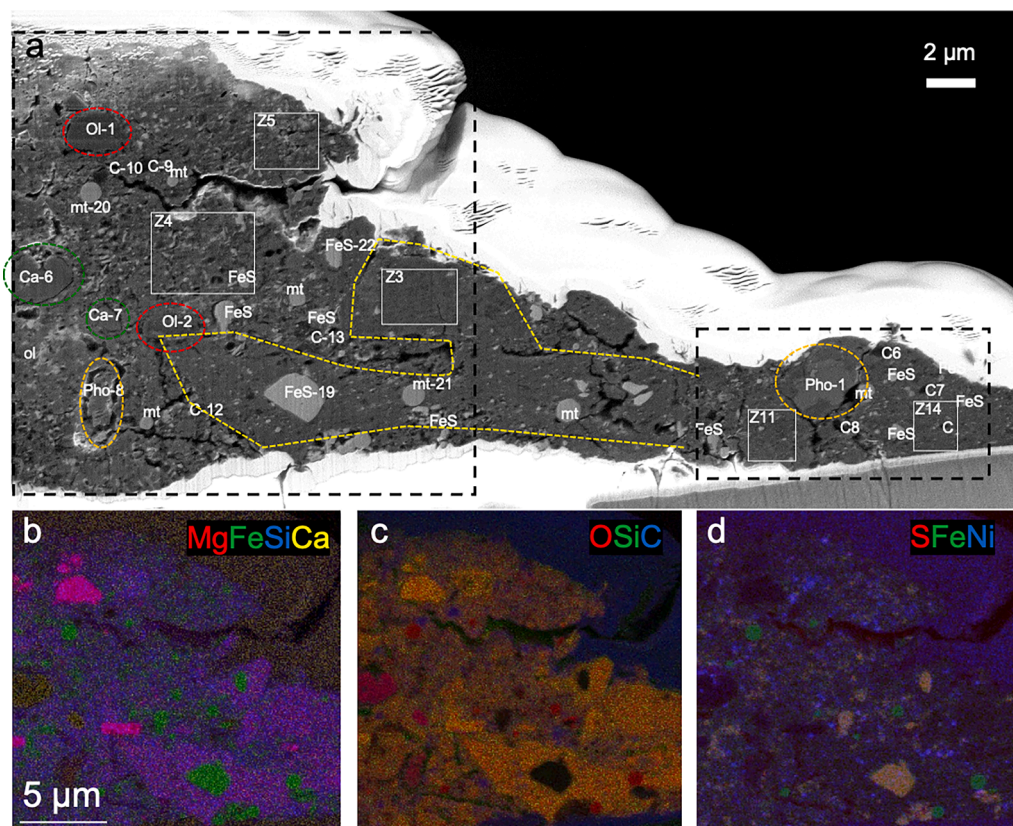
**Fig. 10.** a) BSE images of a) the thick slice extracted from grain A0064-FO021. The white layers surrounding the section correspond to the platinum deposit. b) composite X-ray map of Mg (red), Fe (green), Si (blue) and Ca (yellow) showing the presence of olivine in pink, magnetite and sulfides in green, calcite and phosphate in orange/brown. c) composite X-ray map of O (red), Si (green) and C (blue) showing the presence of magnetite in red, calcite and phosphate in pinked red and carbon rich zones in purple blue. d) composite X-ray map of S(red), Fe (green) and Ni (blue) showing the presence of magnetite in green, Fe-rich sulfide in orange and Ni-rich sulfide in purple. On BSE images, red, green and purple dashed-line circles indicate olivine, calcite and phosphate rich regions respectively. The yellow dashed line circles the compact fine-grained region. The limit of this region is not well defined in the right part of the sample. Left black dashed-line rectangle indicates the analyzed zone corresponding to the X-ray maps (b-d). Left and right black dashed-line rectangles also indicate zones analyzed by EDS (Table 1) as global left and right zone respectively. The numbered white rectangles correspond to zones analyzed by EDS (Table 1). The indicated minerals were identified by X-ray analyses. Some are reported in Table 1. Abbreviations: same as Fig. 5, Ca for calcite, Pho for phosphate.

## 4. Discussion

### 4.1. Mineralogical evidence for variably altered lithologies

As expected by the three different reflectance IR signatures of the grains (Dionnet et al., 2023), the sections extracted from those fragments show very distinctive mineralogy and structure.

#### 4.1.1. Evidence for different lithologies in sections A0064-FO019, C0002-FO019 and A0064-FO021

Sections from grain A0064-FO019, C0002-FO019 and A0064-FO021 show large differences in terms of structure and mineralogy.

##### 4.1.1.1. Porosity and grain sizes.
Comparisons between TEM BF images (Fig. 16) of the three sections at the same scale show clear differences in term of grain sizes and porosity. Section C0002-FO019 has a finer-grained and compact texture compared with section A0064-FO019, which shows very large clusters (>several micrometers) of cg-phyllos distributed in regions rich in fg-phyllos and small sulfides. The fine-grained compact lithology of section A0064-FO021 compares well with that of C0002-FO019, whereas the other lithology exhibits numerous fractures and important porosity, is unique and not similar to either C0002-FO019 or A0064-FO019.

##### 4.1.1.2. Chemical composition at a global scale.
EDS-SEM analyses show that some regions of section A0064-FO019 are more enriched in Na (up

to ∼ 5 at %) than section C0002-FO019 and section A0064-FO021 (∼0.9 at% and 1.5 at%, respectively). The slight enrichment of section A0064-FO019 in Al (∼3,8 at%) with section A0064-FO021 or section C0002-FO019 (∼2,4 at% and ∼ 2,5 at%) has to be taken with caution because of the possible Al contamination from the EDS-SEM holder. Finally, no large difference in the Mg/Si ratio (around 1 ± 0.1) are noticed between A0064-FO019, C0002-FO019 and A0064-FO021. For Fe, S and C, the comparison is more difficult because of the very heterogeneous distribution of their content between the different zones. Notice that, for all sections, zones enriched in sulfides (from Fe and S maps) show higher carbon contents (probably due to the presence of organics or carbonates).

##### 4.1.1.3. Mineralogy.
Major differences in term of mineralogy exist between the three sections. Concerning the silicates, section from A0064-FO019 show well-crystallized cg-phyllos with a composition between the saponite and the serpentine solid solution in addition to fg-phyllos showing a higher saponite contribution (based on EDS chemical analyses). In contrast, section from C0002-FO019 shows anhydrous silicates embedded in a fg-grained matrix poorly crystallized with a composition between the saponite and the serpentine solid solution. Fe-Ni-S rich phases from section C0002-FO019 seem to differ from section A0064-FO019 as 1/ one FeNi metal phase and one C-bearing FeNi metal associated to pyrrhotite/Ni-rich sulfides are present in C0002-FO019 and 2/sulfides are depleted in S and weakly enriched in Ni. In addition, TEM observations seem to reveal that sulfides from
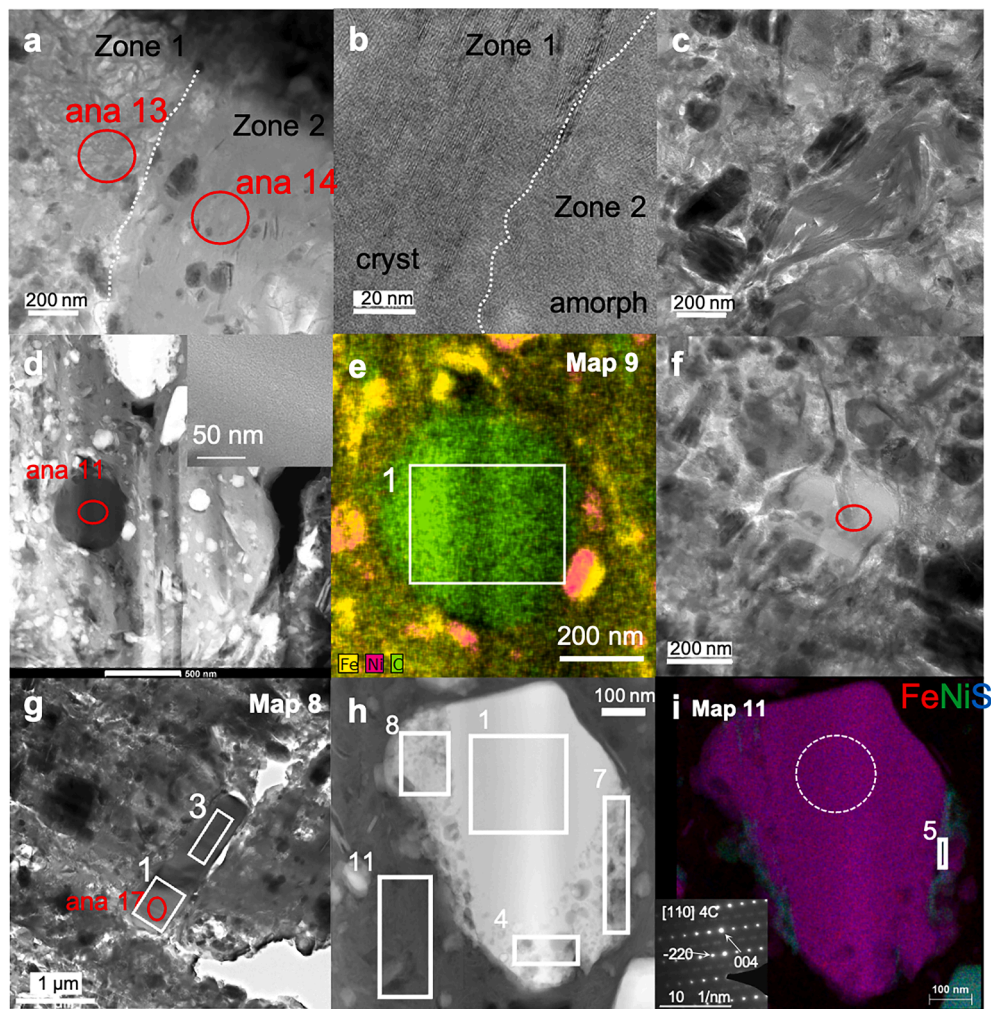
**Fig. 11.** TEM images from section A0064-FO021. (a) Bright field TEM image showing the contact between the porous (zone 1) and the compact (zone 2) regions of A0064-FO021 and close-up (b) of the contact showing the different degree of crystallinity between the two regions with the compact region amorphous and the porous region more crystalline. The crystalline region shows irregular interlayer widths between 0.7 nm and 1.1 nm. (c) Bright field TEM image of a nodule of phyllosilicate in the porous fine-grained region of section A0064-FO021. The interlayer width of the observed layers is around 0.7 nm indicative of serpentine-type phyllosilicate. A STEM composite X-ray map of this region is given in Fig. S5. (d) HAADF-STEM image of a C-rich nanosphere inside the compact fine-grained region of A0064-FO021. The high-resolution image in the top right insert shows the amorphous nature of the nanosphere (e) STEM composite x-ray map of Fe (yellow), Ni (pink) and C (green) showing the presence of heterogeneous Ni-poor and Ni-rich sulfides in contact with the C-rich nanosphere. (f) Bright field TEM images of a C-rich nanoparticle in section A0064-FO021. (g) Bright field TEM image of an olivine from section A0064-FO021. (h-i) HAADF-STEM image (h) and STEM composite X-ray map (i) of Fe (red), Ni (green) and S (blue) of a sulfide from section A0064-FO021. The left bottom insert in (i) gives the diffraction pattern of the white dotted circle region of the sulfide. Although determination of the superstructure of the pyrrhotite is uncertain due to analytical uncertainties, indexation of the diffraction pattern of both vesiculated rim and center of the sulfide corresponds to a 4C pyrrhotite structure. The numbered red circles indicate JEOL TEM analyses acquired in conventional mode (Table 2) whereas the white rectangle corresponds to the zone from which EDS analyses were extracted from the STEM-X-ray map 9 (e), 8 (g) and 11 (i) (Table 3). Abbreviations: amorph for amorphous, cryst for crystalline.

C0002-FO019 show more alteration features/chemical variability than sulfides from A0064-FO019. Indeed, whereas numerous sulfides from C0002-FO019 show the presence of engulfment indicative of dissolution, progressive replacement of sulfide by a Mg-Si-Fe-Ni-S fibrous material, or the presence of heterogeneous Ni-contents in sulfides (e.g. Fig. 8), sulfides from A0064-FO019 (e.g. Fig. 3) show more euhedral shapes and homogeneous composition. Mineralogy of section A0064-FO021 is also very different from section A0064-FO019 and slightly from section C0002-FO019. It shows two different regions: one with the presence of anhydrous silicates, calcite, hydrated Na-rich phosphate, apatite and of a FeNi phosphide associated to a pyrrhotite embedded in a fractured porous fg-grained matrix, where fg- and cg-phyllos are present. The second region shows only sulfides and magnetites embedded in a very poorly crystallized compact fine-grained matrix. Magnetite was principally observed in A0064-FO021 and C0002-FO019. Concerning the C-rich phase, no major mineralogical difference was deduced from

our observations between the three sections.

Sections A0064-FO019 and C0002-FO019 represent thus two very different lithologies. For section A0064-FO021, it is more difficult to identify it with a unique lithology, and it seems that two different lithologies are also present in this section.

### 4.1.2. Comparison with other lithologies from Ryugu and CI chondrites

*4.1.2.1. Comparison with other lithologies from Ryugu.* Observations of Ryugu samples (e.g. Nakamura et al., 2022b; Nakamura et al., 2022a; Yamaguchi et al., 2023; Matsumoto et al., 2022) reported the presence of different lithologies. The lithology referred to as the major Ryugu's lithology (Nakamura et al., 2022b) consists principally of minerals formed by aqueous alteration: saponite, serpentine, carbonates, sulfide and magnetite. Saponite and serpentine are Mg-rich phyllosilicates (Mg/
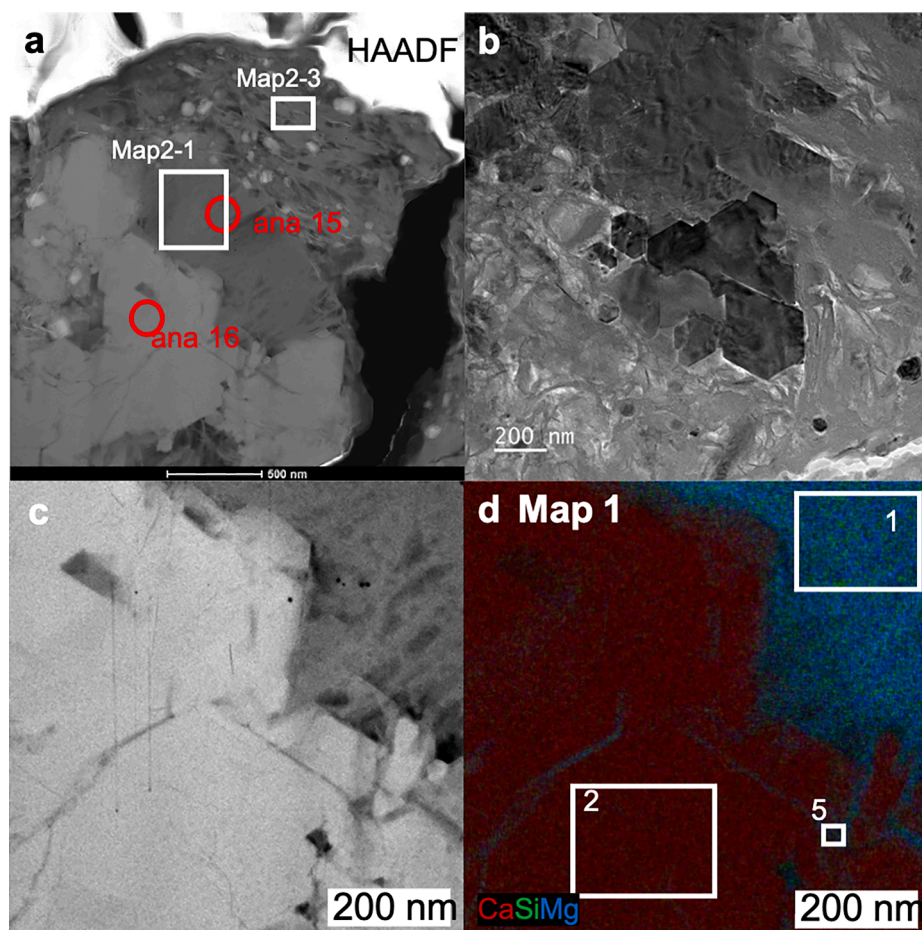
**Fig. 12.** (a) HAADF-STEM image of the right part of the Ca-phosphate from section A0064-FO021 surrounded by a rim of cg-phyllos and embedded in a fg-phyllos- and sulfide-rich matrix. (b) bright-field TEM image of the left part of the Ca-phosphate grain showing that it is constituted by several crystals. (c) HAADF-TEM image of one part of the phosphate with (d) its associated STEM composite X-ray map of Ca (red), Si (green) and Mg (blue). The numbered red circles indicate JEOL TEM analyses acquired in conventional mode (Table 2) whereas the white rectangles correspond to zones from which EDS analyses were extracted from the STEM-X-ray maps 1 (Table 3).

Mg + Fe ratios between 75 and 90) and are observed either as large cg-phyllos clusters or fg-phyllos (e.g. Nakamura et al., 2022a). Sulfide can be observed as large crystals of pyrrhotite but also as nano- to sub-μm sized crystals of pyrrhotite and pentlandite disseminated in the fg-grained-phyllos-rich matrix. Carbonates are dominated by dolomite with the presence of scarcer large breunnerites while Ca-carbonate is very rare (e.g. Loizeau et al., 2023). Magnetite occurs in very diverse morphologies such as framboids, plaquettes or spherules. Other accessory phases in this lithology were observed such as chlorite or Na-rich hydroxyapatite. Even if carbonates or magnetite were not observed, because of the limited sizes of our sections, the section A0064-FO019 is clearly related to this lithology with i) the same dichotomy of size between the cg- and the fg-phyllos, ii) the same composition of the phyllosilicates, iii) the same distribution and the same composition of the sulfide.

Other observed fragments of Ryugu show a very different mineralogy from the major Ryugu lithology (Nakamura et al., 2022a; Nakamura et al., 2022b; Yamaguchi et al., 2023; Matsumoto et al., 2022; Liu et al., 2022; Kawasaki et al., 2022; Nakashima et al., 2023). Indeed, several observations reported the presence of clasts (from 50 to 500 μm large) showing the presence of olivine, low-Ca pyroxene, or smaller silicates phases with sulfide inclusions resembling GEMS (Nakamura et al., 2022b; Nguyen et al., 2023). This lithology has been referred to as the least altered lithology. Micrometer-sized carbonate (calcite or aragonite), pyrrhotite/pentlandite, magnetite, phosphide, Al or Cr spinel, NaMg phosphate and tochilinite were observed in this lithology. Other

less altered lithologies related to this least altered lithology were also observed. Olivines observed in the less altered samples vary in composition from Fo78 to Fo98. These Fo98 forsteritic olivines are < 30 μm, porous and contain about ~ 0.5 at% Mn. Olivines from C0002-FO019 clearly look like those observed in this less altered lithology with the presence of Mn-rich (up to 0.3 at%) very forsteritic olivine (Fo > Fo98). Some of the observed forsterites show the porous texture observed by Nakamura et al. (2022) in larger olivines. but contrary to sub-μm sized olivines observed by Matsumoto et al. (2022) in one less altered grain from Ryugu (C0002 plate-5 fragment-1), the edges of the sub-μm olivines from C0002-FO019 do not show alteration features. The matrix in which the olivines are embedded does not completely look like the one described by Nakamura et al. (2022) in its least altered lithology with i) a less porous texture, ii) the rarer GEMS-like structure that were not clearly observed in our sample. However, we clearly observed anhydrous minerals embedded in a poorly crystallized matrix. Specific observations were not reported elsewhere: i) presence of FeNi-rich metal associated with a pyrrhotite ii) presence of sub-μm sized sulfides showing alteration features and depleted in S. Although Na enrichment reported in the less altered lithology by Nakamura et al. (2022b) (ratio Na/Si twice that of the Sun) was not observed in our section, Na-rich phyllosilicates were observed locally as in the least altered fragment of Nakamura et al. (2022b). Finally, although the observed spiral structure observed in C0002-FO019 was difficult to analyze, its composition rich in Fe, S and Mg and its layered structure resemble that of tochilinite ($Fe^{2+}_{5-6}(Mg,Fe^{2+})_5S_6(OH)_{10}$), which structure consists of
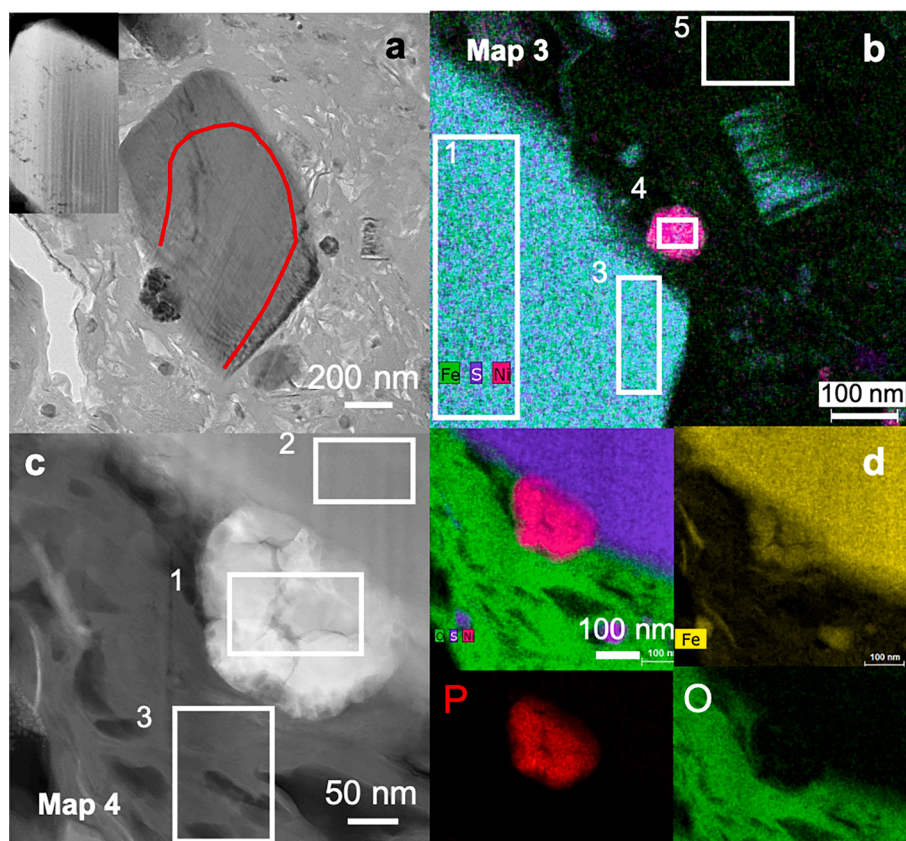
**Fig. 13.** (a) Bright field TEM image of a pyrrhotite embedded in the porous fine-grained matrix of section A0064-FO021. In the top left part of (a) is the HAADF-STEM image of the border of the sulfide showing its nanoporous texture. The red line delimits the porous rim. (b) STEM composite X-ray map of Fe (green), S (purple) and Ni (pink) of the right part of image (a) showing the right part of the large pyrrhotite, a Ni-rich sulfide and an altered lath-shaped sulfide. (c) STEM-HAADF image of a phosphide attached to the bottom of the pyrrhotite with in (d) its associated STEM composite X-ray map of O (green), S (purple) and Ni (pink) and its X-ray map of Fe, P and O. The white rectangles correspond to zones from which EDS analyses were extracted from the STEM-X-ray maps 3 and 4 (Table 3).

layers of iron sulfide alternating with layers of brucite (e.g. Villalon et al., 2021). Tochilinite was observed in the least altered fragment by Nakamura et al. (2022). A micro-sized calcite was also observed in C0002-FO019. In conclusion, section C0002-FO019 is not identical to the least altered lithology described by Nakamura et al. (2022b) but it belongs to the group of less altered lithologies related to the most pristine lithology. Finally, although the compact fine-grained lithology of section A0064-FO021 is of small size and was not showing any anhydrous minerals, this lithology was showing very poorly crystalized material and can thus be related to this group of less altered lithologies.

The porous fractured fg-grained lithology of section A0064-FO021 has many characteristics of the less altered lithologies but shares also some similarities with the major Ryugu lithology. Indeed, as the less altered lithologies, it shows i) the presence of μm-sized forsteritic olivine, ii) the presence of calcite, iii) the presence of Na,Mg-phosphate (as observed by Nakamura et al. 2022b), iv) the porous/fractured texture and v) the presence of (Fe,Ni)$_2$P polymorphs allabogdanite or barringerite associated with pyrrhotite (as observed by Nakamura et al., 2022b). The NaMg-phosphate is rimmed with cracks that seems similar to the shrunk texture observed by Matsumoto et al. (2022) or Nakamura et al. (2022b). However, as in the major lithology of Ruygu, we also observed apatite surrounded by cg-phyllos, and the presence of fg-phyllos. So, although this lithology is a bit particular, the presence of anhydrous minerals and phosphide suggest that it belongs to the group of the less altered lithologies.

In the three sections, the observed diffuse distribution of C intimately mixed with phyllosilicates and the presence of nanoglobules/C-rich nanoparticles is similar to what was observed in Ryugu grains (Yabuta et al., 2023, Le Guillou et al., 2022).

*4.1.2.2. Comparison with CI carbonaceous chondrites.* In our sections, as observed in other Ryugu samples (e.g. Nakamura et al., 2022b), no ferrihydrite, nor sulfate was observed in contrast to what is generally observed in CI chondrites, where they are thought of as terrestrial weathering products (e.g. Gounelle and Zolensky, 2001; Nakamura et al., 2022b, Yamaguchi et al., 2023). Instead of ferrihydrite, sub-μm sulfides were observed in all sections, certainly because they escaped terrestrial alteration (Yamaguchi et al., 2023).

Concerning the carbon distribution, carbon was observed as diffuse matter in the matrix and as solid or hollow nanospheres and nanoparticles in CI chondrites (e.g. Le Guillou et al., 2014; Garvie and Buseck, 2006) but also in CM chondrites, Tagish Lake meteorite, and in some CR chondrites and primitive 3.0 meteorites (e.g. Garvie and Buseck, 2004, De Gregorio et al., 2013). As observed in our sample, Na and N enrichment of the nanospheres were previously reported in an Orgueil nanoglobule (Le Guillou et al., 2014).

Section A0064-FO019, representative of the major Ryugu lithology, clearly shares numerous similarities in terms of mineralogy and structure with CI chondrites, and in particular with the Orgueil meteorite (Tomeoka and Buseck, 1988; Zolensky et al., 1993; Kerridge, 1976). The distribution of the phyllosilicates with large clusters of cg-phyllos associated with finer less oriented phyllosilicates has been observed in Orgueil by Tomeoka and Buseck (1988). They also reported presence of Fe-bearing Mg-rich phyllosilicates with intergrowth of serpentine and saponite with widely dispersed ferrihydrite. The irregularly shaped clusters ranging from 1 to 30 μm were relatively free of ferrihydrite. Based on TEM-EDS compositions and making the assumption that major portion of the Fe in the Orgueil matrix resides in the ferrihydrite, they extrapolated the average composition of the matrix with a Fe/(Fe + Mg)
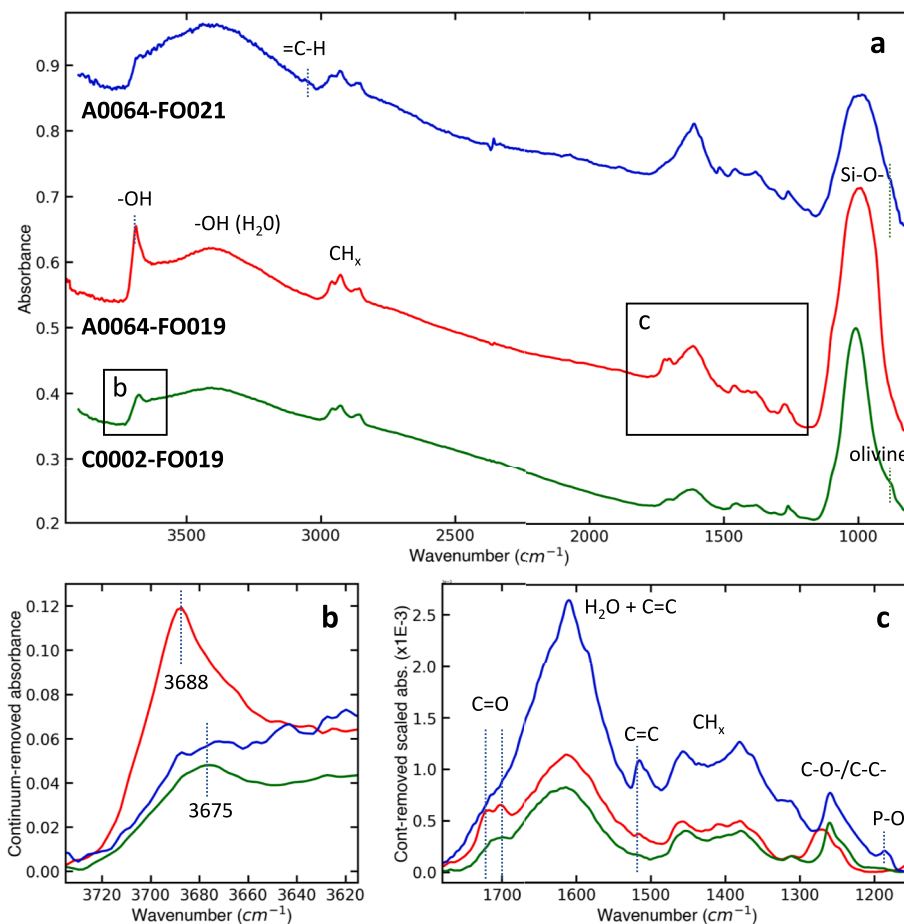
**Fig. 14.** (a) Transmission IR spectra of the three sections C0002-FO019, A0064-FO019 and A0064-FO021. Note that the spectra were shifted for clarity. (b) and (c) zoom on the 3620–3710 $cm^{-1}$ and on the 1100–1800 $cm^{-1}$ regions, respectively. Notice that for (b) and (c), the continuum was removed from the FT-IR spectra. Colors in (b) and (c) corresponds to colors in (a). Vibrational modes of interest are labeled in the different panels.

around 15 % at and with a ratio of 50 % saponite and 50 % serpentine. In Section A0064-FO019, Fe-bearing Mg-rich phyllosilicates were observed with the same size distribution. However, sub-μm sulfides were observed in the fg phyllosilicates instead of ferrihydrite. In addition, EDS analyses are almost comparable with an extrapolated Fe/(Fe + Mg) ratio around 15 % at and an average composition between the saponite and the serpentine solid solution (ratio 50:50). TEM-EDS analyses of phyllosilicates in section A0064-FO019 show a content in Fe less spread toward Fe endmember than in Tomeoka and Buseck (1988). They also show a difference in composition between the fg and the cg phyllosilicates with a higher saponite component in the fg-grained phyllo, which was not reported by Tomeoka and Buseck (1988).

Sulfides observed in CI chondrites are generally larger than several μm, whereas the observed sulfides in this study are <500 nm (e.g. Kerridge et al., 1979; Bullock et al., 2005; Berger et al., 2016). The only large sulfide analysed in A0064-FO019 is a pyrrhotite as observed in Orgueil. Sub-μm sulfides are rarer in CI chondrites. In larger sulfides from CI chondrites, Bullock et al. (2005) reported principally 1/ pyrrhotite in the Orgueil, Ivuna, Tonk and Alais chondrites and 2/ pyrrhotite and pentlandite in Ivuna, Tonk and Alais. Pyrrhotites have a hexagonal or lath-shaped morphology. The pyrrhotites show varying degrees of corrosion and pentlandite occurs as inclusions in pyrrhotite and as isolated grains. Berger et al. (2016) reported an extensive study of the sulfides from Orgueil, Ivuna, Tonk and Alais. They are reported in the Fe-Ni-S ternary diagram on Fig. 4. Even if the number of sulfides analyzed in section A0064-FO019 is low, they seem to be similar to those observed in Orgueil with a slightly more important Fe/S ratio (close to that of FeS) in contrast to those observed in C0002-FO019 and A0064-

FO021, whose compositions seem clearly different with a higher Fe/S ratio (in particular for C0002-FO019 in both Ni-poor and Ni-rich sulfide). Berger et al., (2016) and Dai and Bradley (2001) studied extensively the crystal structure of the sulfides in both CI chondrites and IDPs. Whereas Berger et al. (2016) found monoclinic 4C and 6C pyrrhotites and pentlandite in Orgueil, Dai and Bradley (2001) principally found pyrrhotite with an hexagonal structure in IDPs. Here, the diffraction study of the sulfides was limited and only a pyrrhotite with a 4C structure was observed in A0064-FO021, similarly to Orgueil.

Although magnetites were not observed in the section A0064-FO019 related to the Ruygu major lithology, those observed in the two other sections show the variety of morphologies observed in Orgueil meteorite (Hua and Buseck, 1998). However, we observed a lot of isolated micron-sized euhedral rounded magnetite in section C0002-FO019.

Although not abundant, anhydrous olivines are observed in Orgueil (e.g. Kerridge and MacDougall, 1976; Leshin et al., 1997). Depending on the observations techniques and the analysed CI chondrite, reported abundance varies between <0.01 % (Alfing et al., 2019) for olivine >5 μm to almost 3 to 6 % (Bland et al., 2004; King et al., 2015) with presence of 2.1 % of Fo100, 2.6 % of Fo80 and 1.1 % of Fo60 (Bland et al., 2004) for olivines of any sizes in Orgueil. The observed >5 μm olivines in Orgueil have usually angular shape with no alteration features and close to Fo98-100 composition (Alfing et al., 2019). The observed olivines in sections C0002-FO019 and A0064-FO021 are <1 μm and close to Fo100 with minor amount of Mn for those of C0002-FO019. Ratios of Mn/Fe at% (between 1 and 3) in the measured olivines compare with those reported in low-iron manganese-enriched (LIME) olivines from interplanetary dust particles (IDPs), ameboid

**Table 4**

Maximum peak positions (cm$^{-1}$) and attributions of the different vibrational bands for sections A0064-FO019, A0064-FO021 and C002-FO019. Attributions of the bands are based on Gadallah et al. (2012) and references therein, Ristein et al. (1998), Grishko and Duley (2002) and Jäger et al. (2008). Abbreviation sh is for shoulder.

| Components | A0064-FO021 | A0064-FO019 | A0064-FO019 cg-phyllos | A0064-FO019 fg-phyllos | C0002-FC019 | Detailed Attributions |
|---|---|---|---|---|---|---|
| **Silicate** | | | | | | |
| -Si-O stretchings | 982 | 990 | 978 | 1000 | 1008 | |
| | + sh. at ~ 1100 (relatively large band) | + sh. at ~ 1100 | + sh. at ~ 1100 | + sh. at ~ 1100 | + sh. at ~ 1100 (relatively the sharpest band) | |
| | + sh. 880 | | | | + sh. 874 | |
| MO-H stretchings | ~3680 | 3688 | 3688 | 3688 | 3675 | |
| **H$_2$O*** | | | | | | |
| HO-H stretching** | 3385 (relatively the highest H$_2$O abundance) | 3390 | 3390 | 3390 | 3395 | |
| H-O–H bending | Major contributor to the 1610 large band | Major contributor to the 1614 large band | Major contributor to the 1600 large band | Major contributor to the 1611 large band | Major contributor to the 1613 large band | |
| **Organic matter** | | | | | | |
| –CH$_2$– and –CH$_3$ stretchings | 2855–2860 | 2857 | 2853–2857 (noisy) | 2857 | 2857 | sym –CH$_2$ stretch |
| | 2865–2870 (noisy) | 2871 | (very weak) | 2871 | 2869 | sym –CH$_3$ stretch |
| | 2927 | 2927 | 2925 | 2927 | 2927 | asym –CH$_2$ stretch |
| | 2957–2960 | 2958 | (very weak) | 2958 | 2956 | asym –CH$_3$ stretch |
| | sh. ~ 2990 (weak) | sh. ~ 2990 (weak) | | | | olefinic = CH and/or = CH$_2$ |
| | 3040–3050 (weak) | | | | | aromatic –CH |
| –CH$_2$– and –CH$_3$ bendings | 1363 | sh. at 1361 | (noisy) | sh. at 1361 | sh. at 1361 | sym. bending of different –CH$_3$ moiety types |
| | + 1381 | + 1380–1387 | | + 1380–1387 | + 1378 | |
| | sh. ~ 1411 (very weak) | 1411 | 1411 | 1407–1417 (noisy) | sh. ~ 1411 (very weak) | olefinic = CH$_2$ bending |
| | 1457 (large band + sh. 1465) | 1460 (large band + sh.) | 1459 | 1461 | 1453 (large band + sh. 1465) | CH$_2$ + asym. –CH$_3$ bending |
| **double bonded C** | | | | | | |
| C = C (and possibly C = N) | Contribute to the 1610 large band | Contribute to the 1611 large band | Contribute to the 1600 large band | Contribute to the 1611 large band | Contribute to the 1612 large band | Mixed contributions of C = C and possibly some C = N bonds: non-conjugated, conjugated, and aromatic. |
| | + faint sh. at ~ 1640 | + faint sh. at ~ 1640 | | + faint sh. at ~ 1640 | + faint sh. at ~ 1640 | |
| | + sh. ~ 1583 | + sh. ~ 1581 | | + sh. ~ 1581 | + faint sh. ~ 1580 | |
| | + sh. 1537 | + sh. 1537 | | + sh. 1537 | + faint sh. ~ 1537 | |
| | + 1516 + sh 1505 (distinct protruding band***) | + weak band at 1516 | | + weak band at 1516 | + very weak band at 1517 | |
| C = O | Some contribution to the left shoulder of the 1610 band | Some contribution to the left shoulder of the 1614 band | | | Some contribution to the left shoulder of the 1613 band | |
| | +very weak sh. ~ 1715 | +1702 + 1720 (Distinct protruding double band) | 1702 + 1720 (Distinct protruding double band) | 1703 + 1720 (Distinct protruding double band) | +1706 | |
| **Other bands** | | | | | | |
| -C-O- + -C–C- stretchings | 1260 | 1273 | 1273 | 1273 | 1260 | |
| | + faint sh. ~ 1239 | +sh. 1246 | + sh. 1246 | + sh. 1246 | + sh. 1239 | |
| Not attributed precisely | 1312 | 1310 | 1318 | 1310 | 1312 | |
| | 1180–1185 | | | | | *possible phosphate* |
| | 1880, 2010 & 2070 | | | | | *possible C = C* |

* Mainly corresponding to terrestrial water molecules adsorbed on the surface of the grains constituting the sample. However, the presence of some interlayer water in phyllosilicates is not excluded and may contribute to this band.

** Some organic –OH modes (from alcohol and carboxylic acid moieties), may contribute to this band, but it is impossible to assess it.

*** the band that is notably shifted toward 1500 cm$^{-1}$ may indicate that the C = C vibration correspond here to aromatic rings containing O.

olivine aggregates (AOAs), Stardust grains and meteorite matrices (Klöck et al., 1989; Weisberg et al., 2004; Zolensky et al., 2006). The analytical uncertainties do not allow the distinction between LIME from IDPs and those from AOAs, which are less Mn rich but rule out a connection with chondrule olivines (e.g. Weisberg et al., 2004). The observation of one triple junction between olivines is indicative of a high equilibrium temperature, comparable to those observed in AOAs from CO3.0 meteorite (Han and Brearley, 2015).

Finally, observations of Ryugu sections C0002-FO019 and A0064-FO021 reveal the presence of phases (or the possible presence for the tochilinite) that are not usually observed in CI chondrites. 1/ Tochilinite and presence of Al-Na-rich phyllosilicates are usually observed in CM

chondrites (e.g. Tomeoka and Buseck, 1985). 2/FeNi metal is observed in ordinary chondrites (Kimura et al., 2008), CH/CB or CR chondrites (e. g Weisberg et al., 1993; Meibom et al., 1999) and some were observed in CM chondrites (e.g. Rubin et al., 2007; Kimura et al., 2011; Palmer and Lauretta, 2011; Hewins et al., 2014). 3/ (Fe,Ni)$_2$P polymorphs were very rarely observed (once observed in UCAMMs, Dobrică et al., 2012). Other phosphides, such as schreibersite were observed in the reduced enstatite chondrite group (e.g. Lin and ElGoresy, 2002) but also occasionally in other carbonaceous chondrites (e.g. CM group, Kimura et al., 2011; CO group, Rubin and Grossman, 1985). 4/ It is noticeable that we observed in section C0002-FO019 a whisker olivine. Mg-rich olivines (Fo$_{98-100}$) and enstatite platelets/whiskers were previously observed in the Paris
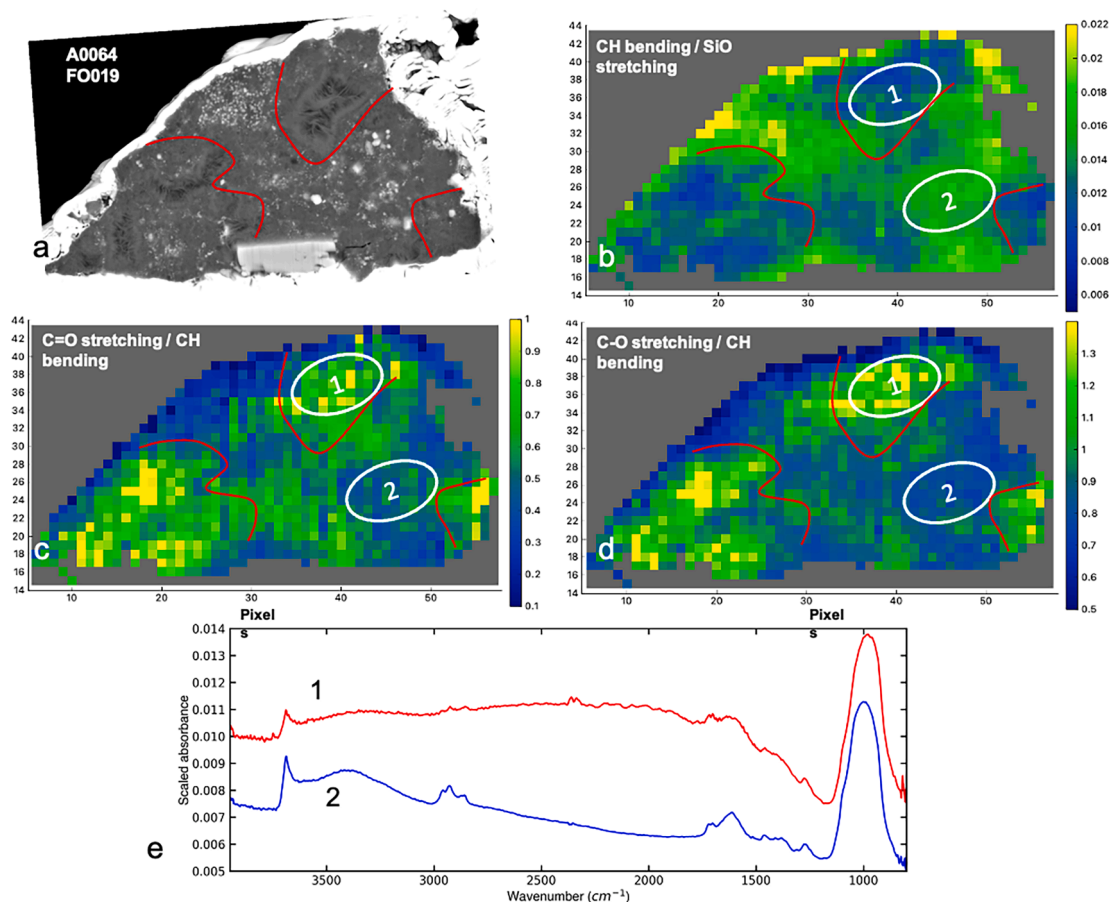
**Fig. 15.** Combined SEM image and IR transmission maps of section A0064-FO019. (a) BSE image of section A0064-FO019. (b) distribution of the ratio of the CH bending over the SiO stretching band areas (between 1330 and 1432 cm$^{-1}$ and between 1154 and 857 cm$^{-1}$, respectively). (c) distribution of the ratio the C=O stretching over the CH bending band areas (between 1685 and 1737 cm$^{-1}$ and between 1330 and 1432 cm$^{-1}$, respectively). (d) distribution of the C-O stretching over the CH bending band areas (between 1230 and 1300 cm$^{-1}$ and between 1330 and 1432 cm$^{-1}$, respectively). (e) Mean IR spectra of areas 1 and 2 in b-c-d extracted from the hyperspectral maps. Spectrum 1 corresponds to that of a zone very rich in cg-phyllos whereas spectrum 2 corresponds to that of a zone very rich in fg-phyllos.
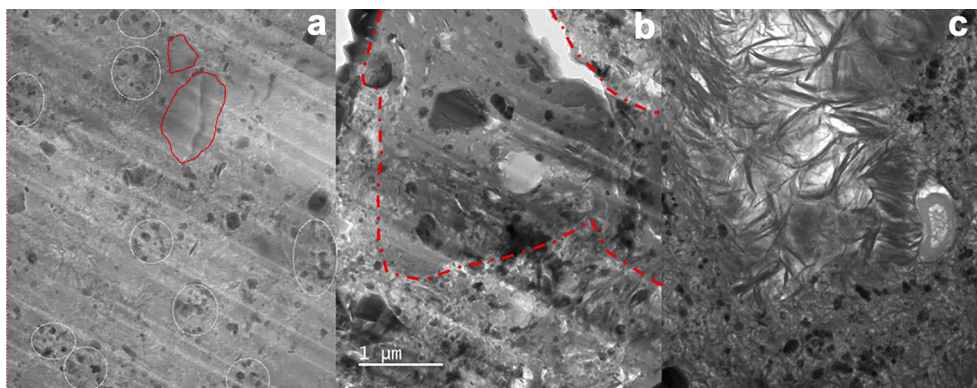


**Fig. 16.** Bright field TEM images of sections (a) C0002-FO019, (b) A0064-FO021 and (c) A0064-FO019. The scale bar is the same for the three images. In (a), white dotted-lines delimit ghosts of GEMS-like structures, i.e. zones enriched in nanosulfides and the red line delimits the borders of two olivines. In (b), the red dotted line delimits the porous fine-grained rich and the compact amorphous regions.

meteorite (Leroux et al., 2015; Villalon et al., 2021) whereas only pyroxene platelets/whiskers were observed in IDPs (Bradley et al., 1983).

### 4.2. Evolution of the IR signature as a function of lithology

The IR mean signature of the observed three sections (Fig. 14 and Table 4) looks like those of Ruygu reported in Nakamura, et al. (2022b),

Dartois et al. (2023) and those of CI chondrites (e.g. Beck et al., 2014; Dartois et al., 2023). Positions and shapes of the different peaks are globally compatible with the presence of Mg-rich Fe-bearing phyllosilicates (partially crystallized), OM and ad-or absorbed water (on the asteroid or due to Earth contamination) (e.g. Beck et al., 2010, 2014; Dionnet et al., 2018; Kebukawa et al., 2010, 2011; Yabuta et al., 2023). The main organic content of the 3 sections have the same "backbone"

structure, as can be deduced from the C—H signatures (stretch. and bend.) and the main C═C and C═O signatures. This "backbone" shows a signature consistent with typical IOM spectra (e.g. Orthous-Daunay et al., 2023; Yabuta et al., 2023) and some hydrogenated amorphous carbon materials produced in laboratory and containing small amount of oxygen and/or nitrogen (e.g. Gadallah et al., 2012; Jäger et al., 2008; Grishko and Duley, 2002; Ristein et al., 1998). However, they also show a variability in the peak band position, shape or width that was also reported in Dartois et al. (2023) on their crushed analyzed grains of Ryugu. Here, as the sample was not crushed, the relationship between phases distributions/compositions/mineralogy observed by SEM and TEM are used 1/ to define the IR spectra of different lithologies and 2/ to better interpret the IR signature variability of the sample. In particular, based on the classification of our sections, we can define the IR signature of section A0064-FO019 as the IR signature of the major Ryugu lithology and the IR signature of section C0002-FO019 as the IR signature of one of the less altered Ryugu lithologies.

### 4.2.1. IR signature of the main Ryugu lithology

The mean IR spectra of section A0064-FO019 represents a mixing between the IR spectrum of cg-phyllos and fg-phyllos (Fig. 15 and Table 4). The cg-phyllos peak maximum position is around 978 cm$^{-1}$, which is close to that of serpentine (mean peak around 955 or 988 cm$^{-1}$, secondary peak around 1079 and 1069 cm$^{-1}$ for the lizardite or antigorite, respectively), whereas the fg-phyllos peak maximum position is around 1000 cm$^{-1}$, which is closer to saponite (mean peak around 1003 cm$^{-1}$) (Beck et al., 2014; Salisbury et al., 1991). These positions of the peak maximum are in agreement with the measured composition of the cg- and fg-phyllos (Fig. 4), which points toward a saponite rich component in the fg-phyllos, whereas the cg-phyllos seems to show a serpentine rich component. The large Si-O-Si asymmetric band of section A0064-FO019 peaks around 990 cm$^{-1}$, which can be understood as a mixing between the two types of phyllosilicates at the scale of our section. Reported IR spectra of Orgueil give a peak band position around 1010 cm$^{-1}$ (e.g. Beck et al., 2014), which is slightly different from the Si—O—Si maximum band position of section A0064-FO019. A very minor shoulder is also visible around 1100 cm$^{-1}$ which was also reported by Beck et al. (2014) in Orgueil and Saponite. A secondary peak around 1176 cm$^{-1}$ in Orgueil was interpreted as resulting from the presence of sulfate in the Orgueil sample. It is not visible in our section A0064-FO019.

Here, mean IR signatures of A0064-FO019, and of both fg- or cg-phyllos show a position around 3688 cm$^{-1}$ for the maximum of the M—OH peak. Beck et al. (2014) also reported a sharp absorption around 3690 cm$^{-1}$ (in reflectance) in Orgueil. IR signatures of pixels from section A0064-FO019 show a slight correlation between the Si—O—Si peak position with the M—OH peak position (Fig. 17). Pixels with a peak position close to 1008 cm$^{-1}$ show a M—OH position close to 3683 cm$^{-1}$ whereas pixels with a peak position close to 975 cm$^{-1}$ show a M—OH close to 3685 cm$^{-1}$ (here M—OH positions are extracted by an asymmetric gaussian fit, which explains why they differ from the average spectrum). As Takir et al. (2013) reported a slightly more higher wavenumber for the M—OH peak position for serpentine polymorph (and in particular for the lizardite – 3688 cm$^{-1}$) than for saponite (3673 cm$^{-1}$), the observed correlation in section A0064-FO019 could be attributed to the higher abundance of serpentine component in the cg-phyllos. However, it is also known that the M—OH band probes the local cationic environment of the hydroxyl groups in the octahedral layer of the phyllosilicates. M—OH peak position can shift toward higher wavenumber with a Mg-enrichment of the phyllosilicate (e.g. Calvin and King, 1997; Beck et al., 2014). So, the M—OH position at higher wavenumber of the cg-phyllos could also be partially attributed to their slightly higher content in Mg compared with the fg-phyllos.

The IR signature of the molecular water-OH between 3100 and 3600 cm$^{-1}$ seems to be more intense in the fg-phyllos-rich region than in the cg-phyllos-rich region, which could be attributed to either 1/ a higher
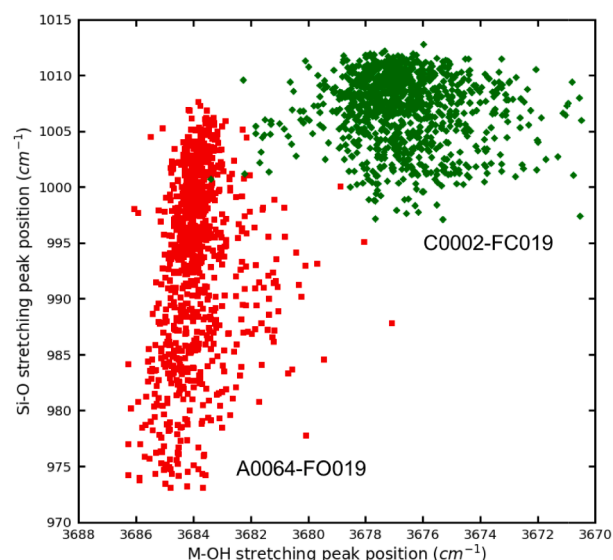


**Fig. 17.** SiO versus M—OH stretching peak positions (cm$^{-1}$) of all pixels extracted from IR transmission maps of sections C0002-FO019 and A0064-FO019.

absorption of water in the saponite rich regions as interlayers water, or 2/ a higher adsorption of water in the fine-grained porous matrix.

In CI chondrites and Ryugu, OM occurs as diffuse fine material intimately intricated with phyllosilicates and as individual particles (including the nanospheres) (e.g. Le Guillou et al., 2014; Yabuta et al., 2023). In the FIB sections of Orgueil reported by Le Guillou et al. (2014), no difference between OM from the cg-phyllos and the fg-phyllos was reported. Yabuta et al. (2023) and Le Guillou et al. (2022) reported that both in Orgueil and Ruygu 1/ the diffuse OM is the main carrier of carbon, 2/ the individual particles are more aromatic than the diffuse OM. However, Le Guillou et al. (2022) showed that the OM from Orgueil contains more oxygenated functional groups than Ryugu. In cg-phyllos from section A0064-FO019, the two distinct features are the protruding double band at 1720 and 1703 cm$^{-1}$ that corresponds to carbonyl (C═O) moieties and the shift and broadening of the band at 1260–1270 cm$^{-1}$ that probably corresponds to the –C—O– stretching mode contribution. It seems to indicate an enhancement of ester and/or carboxylic acid moieties. A slight enhancement of the band at 1410 cm$^{-1}$ that corresponds to olefinic = CH$_2$ bending can also be noticed in section A0064-FO019 which may also indicate a slight increase in olefinic moieties. So here, both SEM-EDS (Fig. 2) and IR analysis (Figs. 14, 15) performed in-situ at local scale show that cg-phyllos seem to present 1/ a lower content in OM and 2/ a difference in the composition of the OM with the fg-phyllos, with a higher content in oxygen-rich functional groups.

### 4.2.2. IR signature of less altered lithologies from Ryugu

Sections C0002-FO019 and A0064-FO021 belong to less altered lithologies than the major Ryugu lithology and show IR spectra different from that of section A0064-FO019.

i. The Si—O—Si vibration band widths and positions vary depending on the lithology (i.e. of the observed sections). Si-O-Si peak is thinner for section C0002-FO019 than for section A0064-FO019 (Fig. 14) with a maximum around 1008 cm$^{-1}$ closer to the peak maximum of saponite or of the fg-phyllos of section A0064-FO019 (Fig. 15). The dispersion of the position of Si—O—Si vibrational band is almost absent for C0002-FO019 whereas it spreads from 974 cm$^{-1}$ to 1008 cm$^{-1}$ for A0064-FO019 (Fig. 17). The smaller width of the Si—O—Si vibration band in section C0002-FO019 can be attributed to the more homogeneous composition/structure of its matrix than section

A0064-FO019. In contrast, A0064-FO021 shows a large Si-O-Si vibrational band and a position of the peak maximum around 982 cm$^{-1}$ which is quite different from sections C0002-FO019 and A0064-FO019. The width and the shift of the band could be possibly related to either 1/ the presence of two different lithologies, 2/ the structure of both lithologies that are different from the two others sections, i.e. a very fractured porous matrix in contact with a compact very fine-grained partially amorphous matrix, 3/ the presence of a small content of cg-phyllos.

It is important to note that sections C0002-FO019 and A0064-FO021, which are proxies for the less altered lithologies, show the very specific band at 870–880 cm$^{-1}$ (more intense for C0002-FO019) probing the presence of the anhydrous olivine in the sections (Fig. 14), as also shown by the SEM and TEM analysis.

The weak band at 1184 cm$^{-1}$ only visible in the IR signature of A0064-FO021 (Fig. 14) can be attributed to the presence of phosphate in this section (Jastrzebski et al., 2011).

ii. The M—OH vibrational peak position varies also depending on the observed lithology. Fig. 14 shows that peak position varies from 3688 cm$^{-1}$ for the major Ryugu lithology (section A0064-FO019) to 3676 cm$^{-1}$ for our least altered lithology (section C0002-FO019). The difference of the mean position of the M—OH position of section C0002-FO019 with section A0064-FO019 is difficult to explain by different Mg/Fe content of the phyllosilicates/fine-grained matrix as these ratios are close for both sections. It could rather be explained by a very different structure and possibly a slightly different composition (e.g. in Al and Na content).

In addition, the difference of M—OH peak intensity between the two sections A0064-FO019 and C0002-FO019 (Fig. 14) could probe a different degree of crystallinity and/or alteration degree as shown by the mineralogy of both sections, with a higher degree of alteration and crystallinity for section A0064-FO019. Section A0064-FO021 shows a weaker M—OH band correlated to an intense molecular H—OH vibrational band. This larger molecular water-OH vibrational could be explained either by the more amorphous/less altered nature of section A0064-FO021 but also by the very porous and fractured structure of one of its lithologies which could favor the ab or adsorption of water. This water explains the higher intensity of the 1600 cm$^{-1}$ band, compared with the two other spectra.

iii. Finally, the three sections also show some differences in terms of their OM IR signatures (Fig. 14). Section C0002-FO019, i.e. one of the less altered lithologies shows an OM IR signature relatively similar to the fg-phyllos-rich portion of section A0064-FO019 (Fig. 15). Similarly to the fg-phyllos of section A0064-FO019, it shows a lower abundance of oxygen-rich functional groups than the cg-phyllos of section A0064-FO019. Section A0064-FO021 is also very different from the two other sections. A small aromatic =C—H band appears clearly at ∼ 3050 cm$^{-1}$, together with a particularly prominent 1516 cm$^{-1}$ band with a right shoulder at 1504 cm$^{-1}$, and a small but clear band at 1184 cm$^{-1}$. The band at 1516 cm$^{-1}$ is faintly present in the right wing of the 1614 cm$^{-1}$ band in the two other sections. As such, it can be attributed to some particular aromatic cycle vibration contributing to the whole C=C band and reflecting the large diversity of configurations that must exist in an IOM-like material. However, its protruding shape in A0064-FO021 spectrum is particularly intriguing. It seems more plausible to attribute it to a specific component that is added to the IOM-like material. According to the three distinguished bands cited above, compared to the IOM-like material, this specific component is particularly rich in aromatic rings that are hydrogenated (bands at ∼3050 cm$^{-1}$ and at 1184 cm$^{-1}$) and contain oxygen similarly to polyfurans (double band at 1504–1516 cm$^{-1}$, Alakhras & Holze (2007)). Finally, it also shows a slight decrease in the C=O vibrational band

abundance. As section A0064-FO021 presents a very fractured lithology which could result from an impact, we propose that its OM could have been modified upon moderate impact heating that, in a favorable local environment, triggered or catalyzed the conversion of part of the carbonyl (C=O) moieties into oxygen-containing aromatic rings.

*4.2.3. Large-scale spectroscopic implications*

As shown by Dionnet et al. (2023) or Brunetto et al., (2023), IR reflective surface measurements of Ryugu asteroid fragment show slight variations in the positions and shape of the ∼10 µm (∼1000 cm$^{-1}$) band. Although those variations are easily comparable with IR signature of other meteorites or parent bodies (Brunetto et al., 2023), the mineralogical origin of those variations are usually more difficult to interpret. Here, we have chosen grains showing variations in the reflectance IR positions and shape of the 10 µm band (Dionnet et al., 2023). Thanks to the correlated IR/SEM/TEM studies of our sections, we show that those variations are related to the degree of alteration of the fragment, i.e. are indicative of the lithology of the grains. The 10 µm IR signature of the grain could thus be used in the future to fingerprint the lithologies, their degree of alteration and their probable mineralogy.

Similarly, a survey in IR reflectance spectroscopy of the position of the ∼2.7 µm (∼3700 cm$^{-1}$) band has been realized on a large number of Ryugu particles (Le Pivert-Jolivet et al., 2023). This survey showed a variation of the position of the 2.7 µm band in the IR signature of the grains from both chambers A and C, which was mainly related to different degrees of space weathering. We show here that variations of the 2.7 µm band may also be related to different mineralogies indicative of different degree of alteration, i.e. different lithologies. Further studies will thus be needed at smaller scale to better evaluate the relative contribution of the space weathering and/or variations of the mineralogy of the grains to the variations of the 2.7 µm band.

*4.3. Implications for the history of asteroid Ryugu*

The initial analyses of Ryugu material have revealed that most of the Ryugu parent body has been extensively altered but preservation of anhydrous material in some lithologies indicates that some of the initial material has been preserved from aqueous alteration. Our study of variably altered lithologies of Ruygu gives clues on the processes that took place at the beginning (section sections C0002-FO019 and A0064-FO021) and during the subsequent evolution of aqueous alteration on the parent body (section A0064-FO019).

*4.3.1. Onset of alteration on Ryugu parent body*

Despite olivine being fairly sensitive to aqueous alteration, previous studies reported the presence of 10 to 30 µm sized olivines preserved in Ryugu, suggesting that they survived the alteration processes because of their large size (Kawasaki et al., 2022; Liu et al., 2022; Nakamura et al., 2022b; Matsumoto et al., 2022). Here, in our least altered lithologies, (sections C0002-FO019 and A0064-FO021) not only large but also sub-µm olivines are preserved. The presence of sub-micrometer sized olivines with no alteration features suggests an extremely low degree of alteration, as proposed also by Matsumoto et al. (2022). This very low degree of alteration is also consistent with preservation of FeNi metal or phosphide, which, as suggested by Nakamura et al. (2022) indicates a water poor and H$_2$-rich environment, with a very low W/R ratio. In addition, the coexistence of phases indicative of oxidizing or reduced conditions within the same µm-sized region (e.g. phosphate and phosphide, FeNi metal and magnetite) points toward a very local environment of alteration.

However, the presence of alteration features in sulfides (sections C0002-FO019 and A0064-FO021), even more sensitive to alteration, such as replacement by phyllosilicates (Fig. 8d), Ni-depletion in rims of Ni-rich sulfides (Fig. 9) and vesiculation of the outer rim of pyrrhotite (Fig. 11h and i) argues that aqueous alteration has already begun

(Fig. 11). The formation of Ni-S-Fe enriched phyllosilicate (Fig. 8d) from sulfide alteration may be related to the formation of tochilinite by alteration of sulfide as suggested by Le Guillou and Brearley (2014) in CR 3.0 carbonaceous chondrite or Leroux et al. (2015) for the Paris CM chondrites. Tochilinite formation from sulfide was also observed in the aqueous alteration experiments of IDPs described in Nakamura-Messenger et al., (2011).

Nakamura-messenger et al. (2011) showed that aqueous alteration of anhydrous porous IDPS led first to the alteration of GEMS with the transformation of amorphous silicates from GEMS into saponite/serpentine, the alteration of nano-sized kamacite and pyrrhotite grains into tochillinite followed by the alteration of Mg-rich pyroxene (enstatite) and finally the alteration of forsterite. Here, in sample C0002-FO019 and A0064-FO021, we only observed forsterite whereas both low-Ca pyroxene and forsterite were observed in the least altered lithology from Nakamura et al., (2022b). In addition with the observation of features of alteration in sulfides, this suggests that the onset of aqueous alteration has already begun and led to the disappearance of low-Ca pyroxene, with the preservation of forsterite.

The presence of amorphous and partially crystallized material (sections C0002-FO019 and A0064-FO021) is commonly observed in primitive solar system material either in type 3.0 carbonaceous chondrites (anhydrous lithology in Paris, C03.0, CR3.0) (e.g. Brearley, 1993; Greshake, 1997; Hewins et al., 2014; Leroux et al., 2015; Abreu and Brearley, 2010; Le Guillou and Brearley, 2014) or in IDPs and UCAAMs (e.g. Bradley et al., 1988; Dobrică et al., 2012). Nakamura et al., (2022b) observed a very porous lithology with GEMS-like amorphous silicates resembling the chondritic porous IDPs (Bradley, 1994), the least altered lithology of Paris (Leroux et al., 2015) or the UCAAMs (Dobrică et al., 2012). Other primitive type 3.0 carbonaceous chondrites present matrices containing less porous amorphous material with embedded sulfides (Brearley, 1993; Greshake, 1997; Hewins et al., 2014; Leroux et al., 2015; Abreu and Brearley, 2010; Le Guillou and Brearley, 2014). GEMS in anhydrous IDPs are amorphous silicates with embedded metal and sulfide objects, usually embedded/rimmed with organic carbon (Ishii et al., 2018). GEMS in UCAMMs differs from GEMS in IDPs as they are enriched in S and present only inclusions of sulfide (Dobrică et al., 2012). The GEMS-like objects described in Ryugu by Nakamura et al., (2022b) or in the least lithology of Paris (Leroux et al., 2015; Ohtaki et al., 2021; Villalon et al., 2021) also present some differences with GEMS from IDPs such as 1/ the absence of FeNi nanoparticle, 2/ trace of poorly crystallized phyllosilicate, that have been interpreted as resulting from aqueous alteration (Nakamura et al., 2022b). The genetic relationships between GEMS like objects found in Paris, or C3.0 primitive meteorites and GEMS from IDPs are discussed in details in Ohtaki et al. (2021) and Villalon et al., 2021. The origins and the filiation of these different types of amorphous materials are thus still under debate (e.g. Keller and Messenger, 2011; Brearley, 1993; Bradley et al., 1999; Ohtaki et al., 2021; Villalon et al., 2021) but are usually interpreted 1/ as resulting from the accretion of primitive amorphous nebular condensates or interstellar grains and 2/ as the initial starting material from which meteorites formed (e.g. Brearley, 1993).

The amorphous/partially crystallized material with cluster of nano-sulfides in section C0002-FO019 exhibit a texture intermediate between a porous aggregate of GEMS-like material and a more compact amorphous/partially crystallized texture. This suggests that clusters of nanosulfides are remnants of individual sub-μm amorphous units such as GEMS-like objects (Fig. 16). As the least altered lithology reported by Nakamura et al., (2022b) presents highly porous aggregates of GEMS-like material, the sulfide-poor interstitial amorphous material between these GEMS-like ghosts can be viewed as an interstitial filling between the GEMS-like units. If the different lithologies of Ryugu are genetically related, this interstitial filling must have formed on the parent body at the onset of aqueous alteration. The variable degree of crystallinity of the matrix observed in section C0002-FO019 (Fig. 6a, b and c) suggests the precipitation of a gel-like material in the pores that progressively

crystallized as phyllosilicates. As proposed by Le Guillou and Brearley (2014), the initial amorphous material was most likely hydrated, which is supported by the micrometer scale variation in the degree of phyllosilicate crystallinity. This interpretation agrees with the above observations of incipient local alteration. Finally, presence of fg-phyllos and minor cg-phyllos in the porous fine-grained lithology of section A0064-FO021 in coexistence with olivines argue for a slightly more advanced stage of alteration for this lithology than for section C0002-FO019.

In nano-to micro sulfides from our least altered lithology, which present features of alteration, the unaltered portion of those sulfides may be inherited directly from the solar nebula. These primary sulfides show depletion in S and enrichment in Ni, of enigmatic origin, compared to pyrrhotite and/or pentlandite (Fig. 4). Both SEM and TEM analyses give consistent results and sulfides from other lithologies have the usual chondritic composition of sulfides, suggesting that these compositions are not the result of an analytical artifact. The presence of μm- sized FeNi metal (Fig. 5) or <100 nm C-bearing FeNi metal surrounded by pyrrhotite (Fig. 9) or Ni-rich sulfides, could be the trace of the sulfidation of FeNi metal in the nebula (e.g. Lauretta et al., 1996, 1997, 1998), although the reaction products of experimental sulfidation differs to some extent from our observations. For example, we did not observe different layers of sulfide surrounding a kamacite core as formed in the sulfidation experiments of Lauretta et al. (1998). This may be due to different sulfidation conditions or different scales of observations. Thus, a possible explanation for the observed sulfide compositions in our least altered lithology would be the combination of two incomplete processes: the progressive sulfidation of FeNi metal in the nebula and the onset of aqueous alteration in the Ryugu parent body. A dedicated study of the structure of the sulfides and comparison with those found in CI chondrites and IDPs (Dai and. Bradley, 2001; Berger et al., 2016) would bring additional information about the nebula versus aqueous alteration processes that led to their formation.

In our least altered lithology, the presence of calcite and magnetite is probably related to their formation during the very onset of alteration, in line with oxygen isotopic composition of calcite and early magnetite (Fujiya et al., 2023; Kita et al., 2022; Aléon et al., 2023). The observation of nm-sized areas with a high Ca content heterogeneously distributed in the matrix (Fig. S3 or S5) of sections C0002-FO019 and A0064-FO021 may be related to the presence of Ca-carbonate precursors of nebular origin such as hydrated amorphous nanocarbonates, which have been experimentally produced by non-equilibrium condensation of a solar gas at low temperature (Toppani et al., 2005). Although magnetites in our least altered lithology differ in morphology from those studied previously, they may have precipitated from a gel-like material, as suggested from TEM observations and water content of magnetite spherulites (Aléon et al., 2023; Dobrică et al., 2023). The onset of alteration could also lead to the formation of various Na-rich phyllosilicates (Nakamura et al., 2022b), as observed in section C0002-FO019. The observation of enigmatic Fe-S-Mg-O layered nodules with a C-rich core may also be related to this onset of aqueous alteration or be of pre-accretionary origin. As they were not observed in the least altered lithology (Nakamura et al., 2022b), we favored a relationship with the beginning of alteration, maybe related with the formation of tochilinite.

### 4.3.2. Advanced aqueous alteration on Ryugu

Based on studies of CI chondrites, numerous authors suggest the first formation of cg-phyllos followed by their evolution into fine-grained material (e.g. Tomeoka and Buseck, 1985, 1988; Buseck and Hua, 1993 and compilations in Morlok et al., 2006).

The observation of different stages of alteration from the least altered lithology (Nakamura et al., 2022b and section C0002-FO019) to the CI-type lithology (section A0064-FO019) rather suggests the formation of fg-phyllos with embedded nano-sulfides before cg-phyllos. Indeed, crystallization of the initial amorphous silicate together with alteration of primary nano- and micro-sulfides during the onset of alteration is expected to produce a fine-grained weakly crystallized phyllosilicate

enriched in S. In the CI-type lithology section A0064-FO019, sub-µm sulfides associated with fine-grained phyllosilicates are different from those of the less altered lithology (sections C0002-FO019 and A0064-FO021). They are euhedral and have compositions of regular pyrrhotite observed in CI, which indicates a secondary origin. So contrary to CM chondrites, where the mobility of S led to formation of tochilinite intermixed with phyllosilicate (Leroux et al., 2015), the conditions of aqueous alteration in Ryugu probably favored the precipitation of a second generation of sulfides associated with fine-grained phyllosilicates.

By contrast cg-phyllos are devoid of nanosulfides indicating a drastically different mechanism of formation, not directly derived from the initial S-rich amorphous silicates. We rather suggest a late precipitation of well crystallized cg-phyllos in larger remaining fractures/veins/pores, with phyllosilicates layers radiating inward from the edges (Fig. 3). The presence of more oxygenated functional groups in OM associated with cg-phyllos indeed suggests more oxidative conditions, eventually in a more water–rich environment. The Mg-enrichment of the cg-phyllos supports a late formation, in line with the idea that early alteration produces more iron-rich phyllosilicates, whereas late alteration produces more Mg-rich minerals due to the late alteration of Mg-rich anhydrous minerals, more resistant to alteration. This late formation of cg-phyllos associated with a more O-rich OM indicates that part of the OM in Ryugu also formed late, either during the precipitation of cg-phyllos or by trapping of mobile organic species in the cg-phyllos, possibly from water soluble OM (e.g. hydrophilic molecules, Vinogradoff et al., 2017). The similarity of the OM IR signature between fg-phyllos and fine-grained matrix from our less altered sections supports formation of fg-phyllos from the initial amorphous matrix of the less altered lithology before the formation of cg-phyllos and associated OM. This implies that different generations of OM are mixed in bulk analyses of Ryugu and possibly other CI-related material. The occurrence of different OM in different mineralogical context at the µm scale must thus be taken into account in future studies.

Finally, section A0064-FO019 shows a higher concentration in diffuse Na, which may result from the redistribution of Na from the Na-rich phyllosilicates present in the least altered lithology, in agreement with extremely short-scale cations diffusions at the beginning of alteration whereas the late stage of alteration favor larger scale processes.

### 4.3.3. Impact evidence

Finally, the combination of the observation of a fractured lithology with the presence of cracks around phosphates and the composition of the OM in A0064-FO021 points toward a slight modification of this lithology by very mild shock (Nakamura et al., 2022b). The presence of such features of impact in the less altered sample is in line with the origin of Ryugu as a reaccumulation of material altered to different degree coming from a parent-body that was disrupted by an impact (Nakamura et al., 2022b; Yamaguchi et al., 2023).

### 4.3.4. Outer solar system origin of primitive Ryugu material

The study of our least altered lithology of Ryugu gives clues to the nature of the initial primitive material from which the major Ryugu lithology could have formed.

Our observations and those of Nakamura et al., (2022b) indicate that the least altered material is mainly composed of highly porous aggregates of sub-µm amorphous silicate units, akin GEMS-like object in UCAMMs or Paris' least altered lithology. The ubiquitous presence of such amorphous material related to UCAMMs or Paris' least altered lithology and their alteration products in Ryugu is in agreement with an outer solar system origin for most of the material accreted in the parent body of asteroid Ryugu (Kemper et al., 2005; van Boekel et al., 2004; Dobrică et al., 2012).

Similarly to UCAMMs and Paris, but contrary to IDPs, the amount of FeNi metal inclusions is limited in amorphous silicate and nano-inclusions are instead dominated by sulfides (Dobrică et al., 2012;

Leroux et al., 2015; Bradley, 1994). The primary nature of those sulfides indicates that the difference between Ryugu, UCAMMS and IDPs is due to nebular processes, for example, a different amount of sulfidation (Dobrică et al., 2012). The occurrence of FeNi phosphide is also quite interesting as it was very rarely observed in meteorites and even less in carbonaceous chondrites. Its observation in UCAMMs (Dobrică et al., 2012) points also toward a common origin of the primitive material of Ryugu with cometary type material.

The presence in the least altered lithology of Ryugu of sub-µm whiskers/platelets olivines and Mn-enriched olivines indicates the preservation of nebular dust condensed at high temperature in the inner region of the protoplanetary disk. The presence of high temperature material is also supported by the occurrence of olivine with triple junction annealed at high temperature. Such morphologies of anhydrous minerals were also observed in the Paris meteorite or anhydrous IDPs (Leroux et al., 2015; Villalon et al., 2021; Bradley et al., 1983) and argue again for a common origin for those classes of objects. The observed anhydrous material in our less altered lithology of Ruygu is extremely fine-grained (sub-µm), in agreement with other observations of anhydrous material related to refractory inclusions or chondrules (Liu et al., 2022; Kawasaki et al., 2022; Nakamura et al., 2022b; Nakashima et al., 2023). Together with the oxygen isotopic distribution in olivine and pyroxene from Ryugu (Kawasaki et al., 2022), the extremely fine-grained nature of the high temperature material observed in Ryugu is similar to that observed in Stardust sample from comet Wild2 and IDPs (Bradley et al., 1983, 1988; Zolensky et al., 2006). The presence of such very small high-temperature material from the inner solar system can be attributed to very efficient transport from the innermost toward the outermost solar system where the parent body of Ryugu and comets accreted.

## 5. Conclusion

The first combination of IR spectroscopy, SEM and TEM on slices extracted from three fragments of Ryugu showing a different IR reflectance signature revealed different lithologies. Each different lithology has its own IR signature, indicative of the mineralogy of the section but also of its history in the Ryugu parent body. The different observed lithologies are comparable to those already observed in Ryugu by Nakamura et al. (2022b). Two lithologies (section C0002-FO019 and the compact fine-grained lithology of section A0064-FO021) are close to the least altered lithology with anhydrous minerals embedded in a partially amorphous matrix. It presents different unequilibrated phases and shows the onset of aqueous alteration in very local micrometer-sized regions. One lithology (section A0064-FO019) resembling the major Ryugu lithology as well as CI chondrites shows an advanced stage of alteration. The last one (the fractured lithology of section A0064-FO021) belongs to the group of the less altered lithologies but shows a slightly more advanced stage of alteration and features of very mild impact. We suggest the following chronology of formation and evolution for Ryugu: (1) accretion of highly porous aggregates of GEMS-like units with fine-grained high-temperature anhydrous silicates, (2) onset of alteration with the dissolution of the sulfides and development of amorphous/partially crystallized material in the pores, (3) crystallisation of fg-phyllos with a second generation of sulfide, (4) later crystallisation of cg-phyllos devoid of nano-sulfides in a more water-rich and oxidizing environment. Formation of other minor phases, such as phosphates, carbonates or magnetite probably occurred during the last two phases.

In the least altered lithology, the mineralogy presents similarities with that of anhydrous interplanetary dust particles, UCAAMs and of some very little altered carbonaceous chondrites, which suggest that the Ryugu parent body sampled material related to comets, as suggested by other mineralogical, or isotopic studies (e.g. Nakamura et al., 2022b; Kawasaki et al., 2022) but also by studies investigating the link between the reflectance IR spectra of Ryugu anhydrous ingredients with that of

primitive asteroids and comets (Brunetto et al., 2023). Some mineralogical observations, such as those of the layered nodules need more advanced studies to be fully understood.

Ryugu thus formed from the reaccumulation of material issued from a parent-body accreted in the outer solar system and later disrupted by an impact (Nakamura et al., 2022b; Yamaguchi et al., 2023; McCain et al., 2023). This material with different degrees of alteration comes from different regions of the parent body with different local alteration conditions, possibly issued from different depths inside the parent body.

## Data availability

Research Data associated with this article can be accessed through Zenodo at https://doi.org/10.5281/zenodo.8321594.

## CRediT authorship contribution statement

## Declaration of competing interest

The authors declare that they have no known competing financial interests or personal relationships that could have appeared to influence the work reported in this paper.

## Acknowledgments

## Appendix A. Supplementary material

Supplementary Material: Six supplementary figures can be found in the online version. Fig. S1 provide a cartoon summarizing the analytical procedure followed in this study. Fig. S2 to Fig. S5 provides additional SEM and TEM/STEM images of the three sections whereas Fig. S6 provides additional IR map of the section C0002-FO019. Supplementary material to this article can be found online at https://doi.org/10.1016/j.gca.2024.02.006.

## References

Abreu, N.M., Brearley, A.J., 2010. Early solar system processes recorded in the matrices of two highly pristine CR3 carbonaceous chondrites, MET 00426 and QUE 99177. Geochim. Cosmochim. Acta 74, 1146–1171.

Alakhras, F., Holze, R., 2007. In situ UV–vis- and FT-IR-spectroscopy of electrochemically synthesized furan–thiophene copolymers. Synthetic Metals 157, 109–119.

Aléon J., Mostefaoui S., Bureau H., Vangu D., Khodja H., 2023. The Hayabusa2 Initial Analysis Chemistry Team, and the Hayabusa2 Initial Analysis Core. An exploration of hydrogen content in magnetite from asteroid Ryugu (abstract #1974). In: 54th Lunar and Planet. Sci. Conf.

Aléon-Toppani, A., Brunetto, R., Aleon, J., Dionnet, Z., Levy, D., Troadec, D., Rubino, S., Brisset, F., Borondics, F., King, A., 2021. A preparation sequence for multi-analysis of lm-sized extraterrestrial and geological samples. Meteorit. Planet. Sci. 56, 1151–1172.

Alfing, J., Patzek, M., Bischoff, A., 2019. Modal abundances of coarse-grained (>5 μm) components within CI-chondrites and their individual clasts – Mixing of various lithologies on the CI parent body(ies). Geochemistry 79, 125532.

Arakawa, M., Saiki, T., Wada, K., Ogawa, K., Kadono, T., Shirai, K., Sawada, H., Ishibashi, K., Honda, R., Sakatani, N., Iijima, Y., Okamoto, C., Yano, H., Takagi, Y., Hayakawa, M., Michel, P., Jutzi, M., Shimaki, Y., Kimura, S., Mimasu, Y., Toda, T., Imamura, H., Nakazawa, S., Hayakawa, H., Sugita, S., Morota, T., Kameda, S., Tatsumi, E., Cho, Y., Yoshioka, K., Yokota, Y., Matsuoka, M., Yamada, M., Kouyama, T., Honda, C., Tsuda, Y., Watanabe, S., Yoshikawa, M., Tanaka, S., Terui, F., Kikuchi, S., Yamaguchi, T., Ogawa, N., Ono, G., Yoshikawa, K., Takahashi, T., Takei, Y., Fujii, A., Takeuchi, H., Yamamoto, Y., Okada, T., Hirose, C., Hosoda, S., Mori, O., Shimada, T., Soldini, S., Tsukizaki, R., Iwata, T., Ozaki, M., Abe, M., Namiki, N., Kitazato, K., Tachibana, S., Ikeda, H., Hirata, N., Hirata, N., Noguchi, R., Miura, A., 2020. An artificial impact on the asteroid 162173 Ryugu formed a crater in the gravity-dominated regime. Science 368, 67–71.

Beck, P., Quirico, E., Montes-Hernandez, G., Bonal, L., Bollard, J., Orthous-Daunay, F.R., Howard, K.T., Schmitt, B., Brissaud, O., Deschamps, F., Wunder, B., Guillot, S., 2010. Hydrous mineralogy of CM and CI chondrites from infrared spectroscopy and their relationship with low albedo asteroids. Geochim. Cosmochim. Acta 74, 4881–4892.

Beck, P., Garenne, A., Quirico, E., Bonal, L., Montes-Hernandez, G., Moynier, F., Schmitt, B., 2014. Transmission infrared spectra (2–25 μm) of carbonaceous chondrites (CI, CM, CV–CK, CR, C2 ungrouped: Mineralogy, water, and asteroidal processes. Icarus 229, 263–277.

Berger, E.L., Lauretta, D.S., Zega, T.J., Keller, L.P., 2016. Heterogeneous histories of Ni-bearing pyrrhotite and pentlandite grains in the CI chondrites Orgueil and Alais. Meteorit. Planet. Sci. 51, 1813–1829.

Bland, P.A., Cressey, G., Menzies, O.N., 2004. Modal mineralogy of carbonaceous chondrites by X-ray diffraction and Mössbauer spectroscopy. Meteorit. Planet. Sci. 39, 3–16.

Bradley, J.P., 1994. Nanometer-scale mineralogy and petrography of fine-grained aggregates in anhydrous interplanetary dust particles. Geochim. Cosmochim. Acta 58, 2123–2134.

Bradley, J.P., Brownlee, D.E., Veblen, D.R., 1983. Pyroxene whiskers and platelets in interplanetary dust particles: evidence of vapor phase growth. Nature 301, 473–477.

Bradley, J.P., Sandford, S.A., Walker, R.M., Kerridge, J.F., Mathews, M.S., 1988. Meteorites and the Early Solar System. University of Arizona Press, Tucson, AZ, pp. 861–895.

Bradley, J.P., Keller, L.P., Snow, T.P., Hanner, M.S., Flynn, G.J., Gezo, J.C., Clemett, S.J., Brownlee, D.E., Bowey, J.E., 1999. An Infrared Spectral Match Between GEMS and Interstellar Grains. Science 285, 1716–1718.

Brearley, A.J., 1993. Matrix and fine-grained rims in the unequilibrated CO3 chondrite, ALHA77307: origins and evidence for diverse, primitive nebular dust components. Geochim. Cosmochim. Acta 57, 1521–1550.

Brunetto, R., Lantz, C., Fukuda, Y., Aléon-Toppani, A., Nakamura, T., Dionnet, Z., Baklouti, D., Borondics, F., Djouadi, Z., Rubino, S., Amano, K., Matsumoto, M., Fujioka, Y., Morita, T., Kukuiri, M., Kagawa, E., Matsuoka, M., Milliken, R., Yurimoto, H., Noguchi, T., Okazaki, R., Yabuta, H., Naraoka, H., Sakamoto, K., Tachibana, S., Yada, T., Nishimura, M., Nakato, A., Miyazaki, A., Yogata, K., Abe, M., Okada, T., Usui, T., Yoshikawa, M., Saiki, T., Tanaka, S., Terui, F., Nakazawa, S., Watanabe, S., Tsuda, Y., 2023. Ryugu's anhydrous ingredients and their spectral link to primitive dust from the outer Solar System. Astrophys. J. 951, L33.

Bullock, E.S., Gounelle, M., Lauretta, D.S., Grady, M.M., Russell, S.S., 2005. Mineralogy and texture of Fe–Ni sulfides in CI1 chondrites: Clues to the extent of aqueous alteration on the CI1 parent body. Geochim. Cosmochim. Acta 69, 2687–2700.

Buseck, P.R., Hua, X., 1993. Matrices of carbonaceous chondrite meteorites. Annu. Rev. Earth Planet. Sci. 21, 255–305.

Calvin, W.M., King, T.V.V., 1997. Spectral characteristics of iron-bearing phyllosilicates: Comparison to Orgueil (CIl), Murchison and Murray (CM2). Meteorit. Planet. Sci. 32, 693–701.

Cliff, G., Lorimer, G.W., 1975. The quantitative analysis of thin specimens. J. Microscopy 103, 203–207.

Dai, Z.R., Bradley, J.P., 2001. Iron-nickel sulfides in anhydrous interplanetary dust particles. Geochim. Cosmochim. Acta 65, 3601–3612.

Dartois, E., Kebukawa, Y., Yabuta, H., Mathurin, J., Engrand, C., Duprat, J., Bejach, L., Dazzi, A., Deniset-Besseau, A., Bonal, L., Quirico, E., Sandt, C., Borondics, F., Barosch, J., Cody, G.D., De Gregorio, B.T., Hashiguchi, M., Kilcoyne, D.A.L., Komatsu, M., Martins, Z., Matsumoto, M., Montagnac, G., Mostefaoui, S., Nittler, L. R., Ohigashi, T., Okumura, T., Remusat, L., Sandford, S., Shigenaka, M., Stroud, R., Suga, H., Takahashi, Y., Takeichi, Y., Tamenori, Y., Verdier-, P.M., Yamashita, S., Nakamura, T., Morita, T., Kikuiri, M., Amano, K., Kagawa, E., Noguchi, T., Naraoka, H., Okazaki, R., Sakamoto, K., Yurimoto, H., Abe, M., Kamide, K., Miyazaki, A., Nakato, A., Nakazawa, S., Nishimura, M., Okada, T., Saiki, T., Tachibana, S., Tanaka, S., Terui, F., Tsuda, Y., Usui, T., Watanabe, S., Yada, T., Yogata, K., Yoshikawa, M., 2023. Chemical composition of carbonaceous asteroid Ryugu from synchrotron spectroscopy in the mid- to far-infrared of Hayabusa2-returned samples. Astron. Astrophys. 671, A2.

De Gregorio, B.T., Stroud, R.M., Nittler, L.R., Alexander, C.M.O'D., Bassim, N.D., Cody, G.D., Kilcoyne, A.L.D., Sandford, S.A., Milam, S.N., Nuevo, M., Zega, T.J., 2013. Isotopic and chemical variation of organic nanoglobules in primitive meteorites. Meteorit. Planet. Sci. 48, 904–928.

Dionnet, Z., Aleon-Toppani, A., Baklouti, D., Borondics, F., Brisset, F., Djouadi, Z., Sandt, C., Brunetto, R., 2018. Organic and mineralogic heterogeneity of the Paris meteorite followed by FTIR hyperspectral imaging. Meteorit. Planet. Sci. 53, 2608–2623.

Dionnet, Z., Aléon-Toppani, A., Brunetto, R., Rubino, S., Suttle, M.D., Lantz, C., Avdellidou, C., Baklouti, D., Borondics, F., Djouadi, Z., Grieco, F., Héripré, E., Nakamura, T., Rotundi, A., Scheel, M., 2022. Multiscale correlated analysis of the Aguas Zarcas CM chondrite. Meteorit. Planet. Sci. 57, 965–988.

Dionnet Z., Rubino S., Aléon-Toppani A., Brunetto R., Tsuchiyama A., Lantz C., Djouadi Z., Baklouti D., Nakamura T., Borondics F., Sandt C., Heripre D., Mivumbi O., Matsumoto M., Amano K., Morita T., Yurimoto H., Noguchi T., Okazaki R., Yabuta H., Naraoka H., Sakamoto K., Tachibana S., Watanabe S., Tsuda Y., and the Hayabusa2-initial-analysis Stone team, 2023. Three-dimensional multi-scale assembly of phyllosilicates, organics and carbonates in small Ryugu fragments. Meteorit. Planet. Sci. http://doi.org/10.1111/maps.14068.

Dobrică, E., Engrand, C., Leroux, H., Rouzaud, J.-N., Duprat, J., 2012. Transmission electron microscopy of CONCORDIA UltraCarbonaceous Antarctic MicroMeteorites (UCAMMs): mineralogical properties. Geochim. Cosmochim. Acta 76, 68–82.

Dobrică, E., Ishii, H.A., Bradley, J.P., Ohtaki, K., Brearley, A.J., Noguchi, T., Matsumoto, T., Miyake, A., Igami, Y., Haruta, M., Saito, H., Hata, S., Seto, Y., Miyahara, M., Tomioka, N., Leroux, H., Le Guillou, C., Jacob, D., de la Peña, F., Laforet, S., Marinova, M., Langenhorst, F., Harries, D., Beck, P., Phan, T.H.V., Rebois, R., Abreu, N.M., Gray, J., Zega, T., Zanetta, P.-M., Thompson, M.S., Stroud, R., Burgess, K., Cymes, B.A., Bridges, J.C., Hicks, L., Lee, M.R., Daly, L., Bland, P.A., Zolensky, M.E., Frank, D.R., Martinez, J., Tsuchiyama, A., Yasutake, M., Matsuno, J., Okumura, S., Mitsukawa, I., Uesugi, K., Uesugi, M., Takeuchi, A., Sun, M., Enju, S., Takigawa, A., Michikami, T., Nakamura, T., Matsumoto, M., Nakauchi, Y., Yurimoto, H., Okazaki, R., Yabuta, H., Naraoka, H., Sakamoto, K., Tachibana, S., Yada, T., Nishimura, M., Nakato, A., Miyazaki, A., Yogata, K., Abe, M., Okada, T., Usui, T., Yoshikawa, M., Saiki, T., Tanaka, S., Terui, F., Nakazawa, S., Watanabe, S., Tsuda, Y., 2023. Nonequilibrium spherulitic magnetite in the Ryugu samples. Geochim. Cosmochim. Acta 346, 65–75.

Fujiya, W., Kawasaki, N., Nagashima, K., Sakamoto, N., Alexander, C.M.O'D., Kita, N.T., Kitajima, K., Abe, Y., Aléon, J., Amari, S., Amelin, Y., Bajo, K., Bizzarro, M., Bouvier, A., Carlson, R.W., Chaussidon, M., Choi, B.-G., Dauphas, N., Davis, A.M., Di Rocco, T., Fukai, R., Gautam, I., Haba, M.K., Hibiya, Y., Hidaka, H., Homma, H., Hoppe, P., Huss, G.R., Ichida, K., Iizuka, T., Ireland, T.R., Ishikawa, A., Itoh, S., Kleine, T., Komatani, S., Krot, A.N., Liu, M.-C., Masuda, Y., McKeegan, K.D., Morita, M., Motomura, K., Moynier, F., Nakai, I., Nguyen, A., Nittler, L., Onose, M., Pack, A., Park, C., Piani, L., Qin, L., Russell, S.S., Schönbächler, M., Tafla, L., Tang, H., Terada, K., Terada, Y., Usui, T., Wada, S., Wadhwa, M., Walker, R.J., Yamashita, K., Yin, Q.-Z., Yokoyama, T., Yoneda, S., Young, E.D., Yui, H., Zhang, A.-C., Nakamura, T., Naraoka, H., Noguchi, T., Okazaki, R., Sakamoto, K., Yabuta, H., Abe, M., Miyazaki, A., Nakato, A., Nishimura, M., Okada, T., Yada, T., Yogata, K., Nakazawa, S., Saiki, T., Tanaka, S., Terui, F., Tsuda, Y., Watanabe, S., Yoshikawa, M., Tachibana, S., Yurimoto, H., 2023. Carbonate record of the change in oxygen fugacity and gaseous species in asteroid Ryugu. Nat. Geosci. 16, 675–682.

Gadallah, K.A.K., Mutschke, H., Jäger, C., 2012. Mid-infrared spectroscopy of UV irradiated hydrogenated amorphous carbon materials. Astron. Astrophys. 544, A107.

Garvie, L.A.J., Buseck, P.R., 2004. Nanosized carbon-rich grains in carbonaceous chondrite meteorite. Earth Planet. Sci. Lett. 224, 431.

Garvie, L.A.J., Buseck, P.R., 2006. Carbonaceous materials in the acid residue from the Orgueil carbonaceous chondrite meteorite. Meteorit. Planet. Sci. 41, 633–642.

Gounelle, M., Zolensky, M.E., 2001. A Terrestrial Origin of Sulfate Veins in CI1 Chondrites. Meteorit. Planet. Sci. 36, 1321–11139.

Greshake, A., 1997. The primitive matrix components of the unique carbonaceous chondrite ACFER 094: a TEM study. Geochim. Cosmochim. Acta 61, 437–452.

Grishko, V.I., Duley, W.W., 2002. Infrared absorption and emission spectra of hydrogenated amorphous carbon prepared in the presence of oxygen, nitrogen, ammonia, and carbon monoxide. Astrophys. J. 568, 448–453.

Han, J., Brearley, A.J., 2015. Microstructural evidence for complex formation histories of amoeboid olivine aggregates from the ALHA77307 CO3.0 chondrite. Meteorit. Planet. Sci. 50, 904–925.

Hewins, R., Bourot-Denise, M., Zanda, B., Leroux, H., Barrat, J.A., Humayun, M., Gopel, C., Greenwood, R.C., Franchi, I.A., Pont, S., Lorand, J.P., Cournède, C., Gattacceca, J., Rochette, P., Kuga, M., Marrocchi, Y., Marty, B., 2014. The Paris meteorite, the least altered CM chondrite so far. Geochim. Cosmochim. Acta 124, 190–222.

Hopp, T., Dauphas, N., Abe, Y., Aléon, J., Alexander, C.M.O'D., Amari, S., Amelin, Y., Bajo, K.-I., Bizzarro, M., Bouvier, A., Carlson, R.W., Chaussidon, M., Choi, B.-G., Davis, A.M., Di Rocco, T., Fujiya, W., Fukai, R., Gautam, I., Haba, M.K., Hibiya, Y., Hidaka, H., Homma, H., Hoppe, P., Huss, G.R., Ichida, K., Iizuka, T., Ireland, T.R., Ishikawa, A., Ito, M., Itoh, S., Kawasaki, N., Kita, N.T., Kitajima, K., Kleine, T., Komatani, S., Krot, A.N., Liu, M.-C., Masuda, Y., McKeegan, K.D., Morita, M., Motomura, K., Moynier, F., Nakai, I., Nagashima, K., Nesvorný, D., Nguyen, A., Nittler, L., Onose, M., Pack, A., Park, C., Piani, L., Qin, L., Russell, S.S., Sakamoto, N., Schönbächler, M., Tafla, L., Tang, H., Terada, K., Terada, Y., Usui, T., Wada, S., Wadhwa, M., Walker, R.J., Yamashita, K., Yin, Q.-Z., Yokoyama, T., Yoneda, S., Young, E.D., Yui, H., Zhang, A.-C., Nakamura, T., Naraoka, H., Noguchi, T., Okazaki, R., Sakamoto, K., Yabuta, H., Abe, M., Miyazaki, A., Nakato, A., Nishimura, M., Okada, T., Yada, T., Yogata, K., Nakazawa, S., Saiki, T., Tanaka, S., Terui, F., Tsuda, Y., Watanabe, S., Yoshikawa, M., Tachibana, S., Yurimoto, H., 2022. Ryugu's nucleosynthetic heritage from the outskirts of the Solar System. Sci. Adv. 8, eadd8141.

Hua, X., Buseck, P.R., 1998. Unusual forms of magnetite in the Orgueil carbonaceous chondrite. Meteorit. Planet. Sci. 33, A215–A220.

Ishii, H.A., Bradley, J.P., Bechtel, H.A., Brownleec, D.E., Bustillo, K.C., Ciston, J., Cuzzie, J.N., Floss, C., Joswiak, D.J., 2018. Multiple generations of grain aggregation in different environments preceded solar system body formation. Proceed. Nat. Astron. Soc. 115, 6608–6613.

Jäger, C., Mutschke, H., Henning, Th., Huisken, F., 2008. Spectral properties of gas-phase condensed fullerene-like carbon nanoparticles from far-ultraviolet to infrared wavelengths. Astrophysi. J. 689, 249–259.

Jastrzębski, W., Sitarz, M., Rokita, M., Bułat, K., 2011. Infrared spectroscopy of different phosphates structures. Spectrochimica Acta Part A 79, 722–727.

Kawasaki, N., Nagashima, K., Sakamoto, N., Matsumoto, T., Bajo, K., Wada, S., Igami, Y., Miyake, A., Noguchi, T., Yamamoto, D., Russell, S.S., Abe, Y., Aléon, J., Alexander, C.M.O., Amari, S., Amelin, Y., Bizzarro, M., Bouvier, A., Carlson, R.W., Chaussidon, M., Choi, B.-G., Dauphas, N., Davis, A.M., Di Rocco, T., Fujiya, W., Fukai, R., Gautam, I., Haba, M.K., Hibiya, Y., Hidaka, H., Homma, H., Hoppe, P., Huss, G.R., Ichida, K., Iizuka, T., Ireland, T.R., Ishikawa, A., Ito, M., Itoh, S., Kita, N. T., Kitajima, K., Kleine, T., Komatani, S., Krot, A.N., Liu, M.-C., Masuda, Y., McKeegan, K.D., Morita, M., Motomura, K., Moynier, F., Nakai, I., Nguyen, A., Nittler, L., Onose, M., Pack, A., Park, C., Piani, L., Qin, L., Schönbächler, M., Tafla, L., Tang, H., Terada, K., Terada, Y., Usui, T., Wadhwa, M., Walker, R.J., Yamashita, K., Yin, Q.-Z., Yokoyama, T., Yoneda, S., Young, E.D., Yui, H., Zhang, A.-C., Nakamura, T., Naraoka, H., Okazaki, R., Sakamoto, K., Yabuta, H., Abe, M., Miyazaki, A., Nakato, A., Nishimura, M., Okada, T., Yada, T., Yogata, K., Nakazawa, S., Saiki, T., Tanaka, S., Terui, F., Tsuda, Y., Watanabe, S., Yoshikawa, M., Tachibana, S., Yurimoto, H., 2022. Oxygen isotopes of anhydrous primary minerals show kinship between asteroid Ryugu and comet 81P/*Wild2*. Sci. Adv. 8, eade2067.

Kebukawa, Y., Nakashima, S., Ishikawa, M., Aizawa, K., Inoue, T., Nakamura-Messenger, K., Zolensky, M.E., 2010. Spatial distribution of organic matter in the Bells CM2 chondrite using near-field infrared microspectroscopy. Meteorit. Planet. Sci. 45, 394–405.

Kebukawa, Y., Alexander, C.M.O'D., Cody, G.D., 2011. Compositional diversity in insoluble organic matter in type 1, 2 and 3 chondrites as detected by infrared spectroscopy. Geochim. Cosmochim. Acta 75, 3530–3541.

Keller, L.P., Messenger, S., 2011. On the origins of GEMS grains. Geochim. Cosmochim. Acta 75, 5336–5365.

Kemper, F., Vriend, W.J., Tielens, A.G.G.M., 2005. Erratum: "the Absence of Crystalline Silicates in the Diffuse Interstellar Medium" (ApJ, 609, 826 [2004]). Astrophys. J. 633, 534.

Kerridge, J.F., 1976. Major element composition of phyllosilicates in the Orgueil carbonaceous meteorite. Earth Planet. Sci. Lett. 29, 194–200.

Kerridge, J.F., MacDougall, J.D., 1976. Mafic silicates in the Orgueil carbonaceous meteorite. Earth Planet. Sci. Lett. 29, 341–348.

Kerridge, J.F., MacDougall, J.D., Marti, K., 1979. Clues to the origin of sulfide minerals in CI chondrites. Earth Planet. Sci. Lett. 43, 359–367.

Kimura, M., Grossman, J.N., Weisberg, M.K., 2008. Fe-Ni metal in primitive chondrites: Indicators of classification and metamorphic conditions for ordinary and CO chondrites. Meteorit. Planet. Sci. 43, 1161–1177.

Kimura, M., Grossman, J.N., Weisberg, M.K., 2011. Fe-Ni metal and sulfide minerals in CM chondrites: An indicator for thermal history. Meteorit. Planet. Sci. 46, 431–442.

King, A.J., Schofield, P.F., Howard, K.T., Russell, S.S., 2015. Modal mineralogy of CI and CI-like chondrites by X-ray diffraction. Geochim. Cosmochim. Acta 165, 148–160.

Kita N. T., Kitajima K., Kawasaki N., Nagashima K., Sakamoto N., Yurimoto H., the Hayabusa2 Initial Analysis Chemistry Team, and the Hayabusa 2 Initial Analysis Core, 2023. High precision SIMS oxygen isotope analyses of carbonates in Ryugu (abstract #1669). In: 54th Lunar and Planet. Sci. Conf.

Klöck, W., Thomas, K.L., McKay, D.S., Palme, H., 1989. Unusual olivine and pyroxene composition in interplanetary dust and unequilibrated ordinary chondrites. Nature 339, 126–128.

Lauretta, D.S., Kremser, D.T., Fegley, B., 1996. The rate of iron sulfide formation in the solar nebula. Icarus 122, 288–315.

Lauretta, D.S., Lodders, K., Fegley, B., 1997. Experimental simulations of sulfide formation in the solar nebula. Science 277, 358–360.

Lauretta, D.S., Lodders, K., Fegley, B., 1998. Kamacite sulfurization in the solar nebula. Meteorit. Planet. Sci. 33, 821–833.

Le Guillou, C., Bernard, S., Brearley, A.J., Remusat, L., 2014. Evolution of organic matter in Orgueil, Murchison and Renazzo during parent body aqueous alteration: In situ investigations. Geochim. Cosmochim. Acta 131, 368–392.

Le Guillou, C., Brearley, A., 2014. Relationships between organics, water and early stages of aqueous alteration in the pristine CR3.0 chondrite MET 00426. Geochim. Cosmochim. Acta 131, 344–367.

Le Guillou C., Bernard S., Leroux H., Noguchi T., Yurimoto H., Nakamura T., Yabuta H., Naraoka H., Okazaki R., Sakamoto K., Tachibana S., Watanabe S., Tsuda Y., and the Min-Pet Fine Sub-team, 2022. Organics and their relationship to phyllosilicates in Ryugu, Orgueil and Ivuna: in situ TEM and XANES study. Ryugu (abstract #2099). In: 53th Lunar and Planet. Sci. Conf.

Le Pivert-Jolivet, T., Brunetto, R., Pilorget, C., Bibring, J.-P., Nakato, A., Hamm, V., Hatakeda, K., Lantz, C., Loizeau, D., Riu, L., Yogata, K., Baklouti, D., Poulet, F., Aléon-Toppani, A., Carter, J., Langevin, Y., Okada, T., Yada, T., Hitomi, Y., Kumagai, K., Miyazaki, A., Nagashima, K., Nishimura, A., Usui, T., Abe, M., Saiki, T., Tanaka, S., Nakazawa, S., Tsuda, Y., Watanabe, S., 2023. Space weathering record and pristine state of Ryugu samples from MicrOmega spectral analysis. Nat. Astron. 7, 1–9.

Leroux, H., Cuvillier, P., Zanda, B., Hewins, R.H., 2015. GEMS-like material in the matrix of the Paris meteorite and the early stages of alteration of CM chondrites. Geochim. Cosmochim. Acta 17, 247–265.

Leshin, L.A., Rubin, A.E., McKeegan, K.D., 1997. The oxygen isotopic composition of olivine and pyroxene from CI chondrites. Geochim. Cosmochim. Acta 61, 835–845.

Lin, Y., El Goresy, A., 2002. A comparative study of opaque phases in Qingzhen (EH3) and MacAlpineHills 88136 (EL3): Representatives of EH and EL parent bodies Meteorit. Planet. Sci. 37, 577–599.

Liu, M.-C., McCain, K.A., Matsuda, N., Yamaguchi, A., Kimura, M., Tomioka, N., Ito, M., Uesugi, M., Imae, N., Shirai, N., Ohigashi, T., Greenwood, R.C., Uesugi, K., Nakato, A., Yogata, K., Yuzawa, H., Kodama, Y., Hirahara, K., Sakurai, I., Okada, I., Karouji, Y., Nakazawa, S., Okada, T., Saiki, T., Tanaka, S., Terui, F., Yoshikawa, M., Miyazaki, A., Nishimura, M., Yada, T., Abe, M., Usui, T., Watanabe, S., Tsuda, Y., 2022. Incorporation of $^{16}$O-rich anhydrous silicates in the protolith of highly hydrated asteroid Ryugu. Nature Astronomy 6, 1172–1177.

Loizeau, D., Pilorget, C., Riu, L., Brunetto, R., Bibring, J.-P., Nakato, A., Aléon-Toppani, A., Hatakeda, K., Yogata, K., Carter, J., Le Pivert-Jolivet, T., Yada, T., Okada, T., Usui, T., Langevin, Y., Lantz, C., Baklouti, D., Miyazaki, A., Nishimura, M., Nagashima, K., Kumagai, K., Hitomi, Y., Abe, M., Saiki, T., Tanaka, S., Nakazawa, S., Tsuda, Y., Watanabe, S., 2023. Constraints on Solar System early evolution by MicrOmega analysis of Ryugu carbonates. Nat. Astron. 7, 391–397.

Matsumoto M., Matsuno J., Tsuchiyama A., Nakamura T., Enokido Y., Miyake A., Enju S., Uesugi K., Takeuchi A., Yasutake M., Fujioka Y., Takigawa A., Okumu-ra S., Mitsukawa I., Sun M., Nakashima D., Morita T., Kikuiri M., Amano K., Kagawa E., Yurimoto H., Noguchi T., Okazaki R., Yabuta H., Naraoka H., Sakamoto K., Tachibana S., Watanabe S., Tsuda Y., 2022. Mineralogical analysis of various lithologies in coarse ryugu samples using transmission electron microscopy (abstract #1344). In: 53th Lunar and Planet. Sci. Conf.

McCain, K.A., Matsuda, N., Liu, M.-C., McKeegan, K.D., Yamaguchi, A., Kimura, M., Tomioka, N., Ito, M., Imae, N., Uesugi, M., Shirai, N., Ohigashi, T., Greenwood, R.C., Uesugi, K., Nakato, A., Yogata, K., Yuzawa, H., Kodama, Y., Hirahara, K., Sakurai, I., Okada, I., Karouji, Y., Nakazawa, S., Okada, T., Saiki, T., Tanaka, S., Terui, F., Yoshikawa, M., Miyazaki, A., Nishimura, M., Yada, T., Abe, M., Usui, T., Watanabe, S., Tsuda, Y., 2023. Early fluid activity on Ryugu inferred by isotopic analyses of carbonates and magnetite. Nat. Astron. 7, 309–317.

Meibom, A., Petaev, M.I., Krot, A.N., Wood, J.A., Keil, K., 1999. Primitive FeNi metal grains in CH carbonaceous chondrites formed by condensation from a gas of solar composition. J. of Geophys. Res. 104, 22053–22059.

Morlok, A., Bischoff, A., Stephan, T., Floss, C., Zinner, E., Jessberger, E.K., 2006. Brecciation and chemical heterogeneities of CI chondrites. Geochim. Cosmochim. Acta 70, 5371–5394.

Morota, T., Sugita, S., Cho, Y., Kanamaru, M., Tatsumi, E., Sakatani, N., Honda, R., Hirata, N., Kikuchi, H., Yamada, M., Yokota, Y., Kameda, S., Matsuoka, M., Sawada, H., Honda, C., Kouyama, T., Ogawa, K., Suzuki, H., Yoshioka, K., Hayakawa, M., Hirata, N., Hirabayashi, M., Miyamoto, H., Michikami, T., Hiroi, T., Hemmi, R., Barnouin, O.S., Ernst, C.M., Kitazato, K., Nakamura, T., Riu, L., Senshu, H., Kobayashi, H., Sasaki, S., Komatsu, G., Tanabe, N., Fujii, Y., Irie, T., Suemitsu, M., Takaki, N., Sugimoto, C., Yumoto, K., Ishida, M., Kato, H., Moroi, K., Domingue, D., Michel, P., Pilorget, C., Iwata, T., Abe, M., Ohtake, M., Nakauchi, Y., Tsumura, K., Yabuta, H., Ishihara, Y., Noguchi, R., Matsumoto, K., Miura, A., Namiki, N., Tachibana, S., Arakawa, M., Ikeda, H., Wada, K., Mizuno, T., Hirose, C., Hosoda, S., Mori, O., Shimada, T., Soldini, S., Tsukizaki, R., Yano, H., Ozaki, M., Takeuchi, H., Yamamoto, Y., Okada, T., Shimaki, Y., Shirai, K., Iijima, Y., Noda, H., Kikuchi, S., Yamaguchi, T., Ogawa, N., Ono, G., Mimasu, Y., Yoshikawa, K., Takahashi, T., Takei, Y., Fujii, A., Nakazawa, S., Terui, F., Tanaka, S., Yoshikawa, M., Saiki, T., Watanabe, S., Tsuda, Y., 2020. Sample collection from asteroid (162173) Ryugu by Hayabusa 2: Implications for surface evolution. Science 368, 654–659.

Nakamura, E., Kobayashi, K., Tanaka, R., Kunihiro, T., Kitagawa, H., Potiszil, C., Ota, T., Sakaguchi, C., Yamanaka, M., Ratnayake, D.M., Tripathi, H., Kumar, R., Avramescu, M.-L., Tsuchida, H., Yachi, Y., Miura, H., Abe, M., Fukai, R., Furuya, S., Hatakeda, K., Hayashi, T., Hitomi, Y., Kumagai, K., Miyazaki, A., Nakato, A., Nishimura, M., Okada, T., Soejima, H., Sugita, S., Suzuki, A., Usui, T., Yada, T., Yamamoto, D., Yogata, K., Yoshitake, M., Arakawa, M., Fujii, A., Hayakawa, M., Naoyuki, H., Naru, H., Honda, R., Honda, C., Hosoda, S., Iijima, Y., Ikeda, H., Ishiguro, M., Ishihara, Y., Iwata, T., Kawahara, K., Kikuchi, S., Kitazato, K., Matsumoto, K., Matsuoka, M., Michikami, T., Mimasu, Y., Miura, A., Morota, T., Nakazawa, S., Namiki, N., Noda, H., Noguchi, R., Ogawa, N., Ogawa, K., Okamoto, C., Ono, G., Ozaki, M., Saiki, T., Sakatani, N., Sawada, H., Senshu, H., Shimaki, Y., Shirai, K., Takei, Y., Takeuchi, H., Tanaka, S., Tatsumi, E., Terui, F., Tsukizaki, R., Wada, K., Yamada, M., Yamada, T., Yamamoto, Y., Yano, H., Yokota, Y., Yoshihara, K., Yoshikawa, M., Yoshikawa, K., Fujimoto, M., Watanabe, S., Tsuda, Y., 2022a. On the origin and evolution of the asteroid Ryugu: a comprehensive geochemical perspective. Proc. Jpn. Acad. Ser. B 98, 227–282.

Nakamura, T., Matsumoto, M., Amano, K., Enokido, Y., Zolensky, M.E., Mikouchi, T., Genda, H., Tanaka, S., Zolotov, M.Y., Kurosawa, K., Wakita, S., Hyodo, R., Nagano, H., Nakashima, D., Takahashi, Y., Fujioka, Y., Kikuiri, M., Kagawa, E., Matsuoka, M., Brearley, A.J., Tsuchiyama, A., Uesugi, M., Matsuno, J., Kimura, Y., Sato, M., Milliken, R.E., Tatsumi, E., Sugita, S., Hiroi, T., Kitazato, K., Brownlee, D., Joswiak, D.J., Takahashi, M., Ninomiya, K., Takahashi, T., Osawa, T., Terada, K., Brenker, F.E., Tkalcec, B.J., Vincze, L., Brunetto, R., Aléon-Toppani, A., Chan, Q.H. S., Roskosz, M., Viennet, J.-C., Beck, P., Alp, E.E., Michikami, T., Nagaashi, Y., Tsuji, T., Ino, Y., Martinez, J., Han, J., Dolocan, A., Bodnar, R.J., Tanaka, M., Yoshida, H., Sugiyama, K., King, A.J., Fukushi, K., Suga, H., Yamashita, S., Kawai, T., Inoue, K., Nakato, A., Noguchi, T., Vilas, F., Hendrix, A.R., Jaramillo-Correa, C., Domingue, D.L., Dominguez, G., Gainsforth, Z., Engrand, C., Duprat, J., Russell, S.S., Bonato, E., Ma, C., Kawamoto, T., Wada, T., Watanabe, S., Endo, R., Enju, S., Riu, L., Rubino, S., Tack, P., Takeshita, S., Takeichi, Y., Takeuchi, A., Takigawa, A., Takir, D., Tanigaki, T., Taniguchi, A., Tsukamoto, K., Yagi, T., Yamada, S., Yamamoto, K., Yamashita, Y., Yasutake, M., Uesugi, K., Umegaki, I., Chiu, I., Ishizaki, T., Okumura, S., Palomba, E., Pilorget, C., Potin, S.M., Alasli, A., Anada, S., Araki, Y., Sakatani, N., Schultz, C., Sekizawa, O., Sitzman, S.D., Sugiura, K., Sun, M., Dartois, E., De Pauw, E., Dionnet, Z., Djouadi, Z., Falkenberg, G., Fujita, R., Fukuma, T., Gearba, I.R., Hagiya, K., Hu, M.Y., Kato, T., Kawamura, T., Kimura, M., Kubo, M.K., Langenhorst, F., Lantz, C., Lavina, B., Lindner, M., Zhao, J., Vekemans, B., Baklouti, D., Bazi, B., Borondics, F., Nagasawa, S., Nishiyama, G., Nitta, K., Mathurin, J., Matsumoto, T., Mitsukawa, I., Miura, H., Miyake, A., Miyake, Y., Yurimoto, H., Okazaki, R., Yabuta, H., Naraoka, H., Sakamoto, K., Tachibana, S., Connolly, H.C., Lauretta, D.S., Yoshitake, M., Yoshikawa, M., Yoshikawa, K., Yoshihara, K., Yokota, Y., Yogata, K., Yano, H., Yamamoto, Y., Yamamoto, D., Yamada, M., Yamada, T., Yada, T., Wada, K., Usui, T., Tsukizaki, R., Terui, F., Takeuchi, H., Takei, Y., Iwamae, A., Soejima, H., Shirai, K., Shimaki, Y., Senshu, H., Sawada, H., Saiki, T., Ozaki, M., Ono, G., Okada, T., Ogawa, N., Ogawa, K., Noguchi, R., Noda, H., Nishimura, M., Namiki, N., Nakazawa, S., Morota, T., Miyazaki, A., Miura, A., Mimasu, Y., Matsumoto, K., Kumagai, K., Kouyama, T., Kikuchi, S., Kawahara, K., Kameda, S., Iwata, T., Ishihara, M., Ishiguro, M., Ikeda, H., Hosoda, S., Honda, R., Honda, C., Hitomi, Y., Hirata, N., Hirata, N., Hayashi, T., Hayakawa, M., Hatakeda, K., Furuya, S., Fukai, R., Fujii, A., Cho, Y., Arakawa, M., Abe, M., Watanabe, S., Tsuda, Y., 2022b. Formation and evolution of carbonaceous asteroid Ryugu: Direct evidence from returned samples. Science 379 (6634), eabn8671.

Nakamura-messenger, K., Clemett, S.J., Messenger, S., Keller, L.P., 2011. Experimental aqueous alteration of cometary dust. Meteorit. Planet. Sci. 46, 843–856.

Nakashima, D., Nakamura, T., Zhang, M., Kita, N.T., Mikouchi, T., Yoshida, H., Enokido, Y., Morita, T., Kikuiri, M., Amano, K., Kagawa, E., Yada, T., Nishimura, M., Nakato, A., Miyazaki, A., Yogata, K., Abe, M., Okada, T., Usui, T., Yoshikawa, M., Saiki, T., Tanaka, S., Nakazawa, S., Terui, F., Yurimoto, H., Noguchi, T., Yabuta, H., Naraoka, H., Okazaki, R., Sakamoto, K., Watanabe, S., Tachibana, S., Tsuda, Y., 2023. Chondrule-like objects and Ca-Al-rich inclusions in Ryugu may potentially be the oldest Solar System materials. Nat. Commun. 14, 532.

Nguyen, A.N., Mane, P., Keller, L.P., Piani, L., Abe, Y., Aléon, J., Alexander, C.M.O'D., Amari, S., Amelin, Y., Bajo, K.-I., Bizzarro, M., Bouvier, A., Carlson, R.W., Chaussidon, M., Choi, B.-G., Dauphas, N., Davis, A.M., Di Rocco, T., Fujiya, W., Fukai, R., Gautam, I., Haba, M.K., Hibiya, Y., Hidaka, H., Homma, H., Hoppe, P., Huss, G.R., Ichida, K., Iizuka, T., Ishikawa, A., Itoh, S., Kawasaki, N., Kita, N.T., Kitajima, K., Kleine, T., Komatani, S., Krot, A.N., Liu, M.-C., Masuda, Y., McKeegan, K.D., Morita, M., Motomura, K., Moynier, F., Nakai, I., Nagashima, K., Nesvorný, D., Nittler, L., Onose, M., Pack, A., Park, C., Qin, L., Russell, S.S., Sakamoto, N., Schönbächler, M., Tafla, L., Tang, H., Terada, K., Terada, Y., Usui, T., Wada, S., Wadhwa, M., Walker, R.J., Yamashita, K., Yin, Q.-Z., Yokoyama, T., Yoneda, S., Young, E.D., Yui, H., Zhang, A.-C., Nakamura, T., Naraoka, H., Noguchi, T., Okazaki, R., Sakamoto, K., Yabuta, H., Abe, M., Miyazaki, A., Nakato, A., Nishimura, M., Okada, T., Yada, T., Yogata, K., Nakazawa, S., Saiki, T., Tanaka, S., Terui, F., Tsuda, Y., Watanabe, S.-I., Yoshikawa, M., Tachibana, S., Yurimoto, H., 2023. Abundant presolar grains and primordial organics preserved in carbon-rich exogenous clasts in asteroid Ryugu. Sci. Adv. 9, eadh1003.

Ohtaki, K.K., Ishii, H.A., Bradley, J.P., Villalon, K.L., Davis, A.M., Stephan, T., Bustillo, K. C., Ciston, J., 2021. Search for meteoritic GEMS I: Comparison of amorphous silicates in Paris and Acfer 094 chondrite matrices and in anhydrous chondritic interplanetary dust particles. Geochim. Cosmochim. Acta 310, 320–345.

Orthous-Daunay, F.-R., Quirico, E., Beck, P., Brissaud, O., Dartois, E., Pino, T., Schmitt, B., 2023. Mid-infrared study of the molecular structure variability of insoluble organic matter from primitive chondrites. Icarus 223, 534–543.

Palmer, E.E., Lauretta, D.S., 2011. Aqueous alteration of kamacite in CM chondrites. Meteorit. Planet. Sci. 46, 1587–1607.

Ristein, J., Stief, R.T., Ley, L., Beyer, W., 1998. A comparative analysis of a-C: H by infrared spectroscopy and mass selected thermal effusion. J. Appl. Phys. 84, 3836–3847.

Rubin, A.E., Grossman, J.N., 1985. Phosphate-sulfide assemblages and Al/Ca ratios in type-3 chondrites. Meteorit. Planet. Sci. 20, 479–489.

Rubin, A.E., Trigo-RodríÀLguez, J.M., Huber, H., Wasson, J.T., 2007. Progressive aqueous alteration of CM carbonaceous chondrites. Geochim. Cosmochim. Acta 71, 2361–2382.

Rubino, S., Dionnet, Z., Aléon-Toppani, A., Brunetto, R., Nakamura, T., Baklouti, D., Djouadi, Z., Lantz, C., Mivumbi, O., Borondics, F., Lefrançois, S., Sandt, C., Capitani, F., Héripré, E., Troadec, D., Matsumoto, M., Amano, K., Morita, T., Yurimoto, H., Noguchi, T., Okazaki, R., Yabuta, H., Naraoka, H., Sakamoto, K., Tachibana, S., Watanabe, S., Tsuda, Y., 2023. Small grains from Ryugu: handling and analysis pipeline for Infrared Synchrotron Microspectroscopy. Proceedding Hayabusa symposium. Earth Planets Space 75, 4.

Salisbury, J.W., Walter, L.S., Vergo, N., D'Aria, D., 1991. Infrared (2.1–25 μm) Spectra of Minerals. Johns Hopkins University Press, Baltimore.

Sawada H., Okazaki R., Tachibana S., Sakamoto K., Takano Y., Okamoto C., Yano H., Miura Y.N., Abe M., Hasegawa, S., Noguchi T. and the Hayabusa2 SMP Team, 2017. Hayabusa2 sampler: Collection of asteroidal surface material. Space Sci. Rev. 208, 81–106.

Tachibana, S., Sawada, H., Okazaki, R., Takano, Y., Sakamoto, K., Miura, Y.N., Okamoto, C., Yano, H., Yamanouchi, S., Michel, P., Zhang, Y., Schwartz, S., Thuillet, F., Yurimoto, H., Nakamura, T., Noguchi, T., Yabuta, H., Naraoka, H., Tsuchiyama, A., Imae, N., Kurosawa, K., Nakamura, A.M., Ogawa, K., Sugita, S., Morota, T., Honda, R., Kameda, S., Tatsumi, E., Cho, Y., Yoshioka, K., Yokota, Y., Hayakawa, M., Matsuoka, M., Sakatani, N., Yamada, M., Kouyama, T., Suzuki, H., Honda, C., Yoshimitsu, T., Kubota, T., Demura, H., Yada, T., Nishimura, M., Yogata, K., Nakato, A., Yoshitake, M., Suzuki, A.I., Furuya, S., Hatakeda, K., Miyazaki, A., Kumagai, K., Okada, T., Abe, M., Usui, T., Ireland, T.R., Fujimoto, M., Yamada, T., Arakawa, M., Connolly Jr., H.C., Fujii, A., Hasegawa, S., Hirata, N., Hirata, N., Hirose, C., Hosoda, S., Iijima, Y., Ikeda, H., Ishiguro, M., Ishihara, Y., Iwata, T., Kikuchi, S., Kitazato, K., Lauretta, D.S., Libourel, G., Marty, B., Matsumoto, K., Michikami, T., Mimasu, Y., Miura, A., Mori, O., Nakamura-Messenger, K., Namiki, N., Nguyen, A.N., Nittler, L.R., Noda, H., Noguchi, R., Ogawa, N., Ono, G., Ozaki, M., Senshu, H., Shimada, T., Shimaki, Y., Shirai, K., Soldini, S., Takahashi, T., Takei, Y., Takeuchi, H., Tsukizaki, R., Wada, K., Yamamoto, Y., Yoshikawa, K., Yumoto, K., Zolensky, M.E., Nakazawa, S., Terui, F., Tanaka, S., Saiki, T., Yoshikawa, M., Watanabe, S., Tsuda, Y., 2022. Pebbles and sand on asteroid (162173) Ryugu: In situ observation and particles returned to Earth. Science 375, 1011–1016.

Takir, D., Emery, J.P., McSween, H.Y., Hibbitts, C.A., Clark, R.N., Pearson, N., Wang, A., 2013. Nature and degree of aqueous alteration in CM and CI carbonaceous chondrites. Meteorit. Planet. Sci. 48, 1618–1637.

Tomeoka, K., Buseck, P., 1985. Indicators of aqueous alteration in CM carbonaceous chondrites: microtextures of a layered mineral containing Fe, S, O and Ni. Geochim. Cosmochim. Acta 49, 2149–2163.

Tomeoka, K., Buseck, P.R., 1988. Matrix mineralogy of the Orgueil CI carbonaceous chondrite. Geochim. Cosmochim. Acta 52, 1627–1640.

Toplak, M., Birarda, G., Read, S., Sandt, C., Rosendahl, S.M., Vaccari, L., Demšar, J., Borondics, F., 2017. Infrared Orange: Connecting Hyperspectral Data with Machine Learning. Synchrotron Radiation News 30, 40–45.

Toppani, A., Robert, F., Libourel, G., de Donato, P., Barres, O., d'Hendecourt, L., Ghanbaja, J., 2005. A 'dry' condensation origin for circumstellar carbonates. Nature 437, 1121–1124.

van Boekel, R., Min, M., Leinert, C., Waters, L.B.F.M., Richichi, A., Chesneau, O., Dominik, C., Jaffe, W., Dutrey, A., Graser, U., Henning, T., de Jong, J., Kohler, R., de Koter, A., Lopez, B., Malbet, F., Morel, S., Paresce, F., Perrin, G., Preibisch, T., Przygodda, F., Scholler, M., Wittkowski, M., 2004. The building blocks of planets within the 'terrestrial' region of protoplanetary disks. Nature 432, 479–482.

Villalon, K.L., Ohtaki, K.K., Bradley, J.P., Ishii, H.A., Davis, A.M., Stephan, T., 2021. Search for meteoritic GEMS II: Comparison of inclusions in amorphous silicates from the Paris chondrite and from anhydrous chondritic interplanetary dust particles. Geochim Cosmochim. Acta 310, 346–362.

Vinogradoff, V., Le Guillou, C., Bernard, S., Binet, L., Cartigny, P., Brearley, A.J., Remusat, L., 2017. Paris vs. Murchison: Impact of hydrothermal alteration on organic matter in CM chondrites. Geochim. Cosmochim. Acta 212, 234–252.

Watanabe, S., Hirabayashi, M., Hirata, N., Hirata, N., Noguchi, R., Shimaki, Y., Ikeda, H., Tatsumi, E., Yoshikawa, M., Kikuchi, S., Yabuta, H., Nakamura, T., Tachibana, S., Ishihara, Y., Morota, T., Kitazato, K., Sakatani, N., Matsumoto, K., Wada, K., Senshu, H., Honda, C., Michikami, T., Takeuchi, H., Kouyama, T., Honda, R., Kameda, S., Fuse, T., Miyamoto, H., Komatsu, G., Sugita, S., Okada, T., Namiki, N., Arakawa, M., Ishiguro, M., Abe, M., Gaskell, R., Palmer, E., Barnouin, O.S., Michel, P., French, A., McMahon, J.W., Scheeres, D.J., Abell, P.A., Yamamoto, Y., Tanaka, S., Shirai, K., Matsuoka, M., Yamada, M., Yokota, Y., Suzuki, H., Yoshioka, K., Cho, Y., Tanaka, S., Nishikawa, N., Sugiyama, T., Kikuchi, H., Hemmi, R., Yamaguchi, T., Ogawa, N., Ono, G., Mimasu, Y., Yoshikawa, K., Takahashi, T., Takei, Y., Fujii, A., Hirose, C., Iwata, T., Hayakawa, M., Hosoda, S., Mori, O., Sawada, H., Shimada, T., Soldini, S., Yano, H., Tsukizaki, R., Ozaki, M., Iijima, Y., Ogawa, K., Fujimoto, M., Ho, T.-m, Moussi, A., Jaumann, R., Bibring, J.-P., Krause, C., Terui, F., Saiki, T., Nakazawa, S., Tsuda, Y., 2019. Hayabusa2 arrives at the carbonaceous asteroid 162173 Ryugu—A spinning top–shaped rubble pile. Science 364, 268–272.

Weisberg, M.K., Prinz, M., Clayton, R.N., Mayeda, T.K., 1993. The CR (Renazzo-type) carbonaceous chondrite group and its implications. Geochim. Cosmochim. Acta 57, 1567–1586.

Weisberg, M.K., Connolly Jr, H.C., Ebel, D.S., 2004. Petrology and origin of amoeboid olivine aggregates in CR chondrites. Meteorit. Planet. Sci. 39, 1741–1753.

Yabuta, H., Cody, G.D., Engrand, C., Kebukawa, Y., De Gregorio, B., Bonal, L., Remusat, L., Stroud, R., Quirico, E., Nittler, L., Hashiguchi, M., Komatsu, M., Okumura, T., Mathurin, J., Dartois, E., Duprat, J., Takahashi, Y., Takeichi, Y., Kilcoyne, D., Yamashita, S., Dazzi, A., Deniset-Besseau, A., Sandford, S., Martins, Z., Tamenori, Y., Ohigashi, T., Suga, H., Wakabayashi, D., Verdier-Paoletti, M., Mostefaoui, S., Montagnac, G., Barosch, J., Kamide, K., Shigenaka, M., Bejach, L., Matsumoto, M., Enokido, Y., Noguchi, T., Yurimoto, H., Nakamura, T., Okazaki, R., Naraoka, H., Sakamoto, K., Connolly Jr., H.C., Lauretta, D.S., Abe, M., Okada, T., Yada, T., Nishimura, M., Yogata, K., Nakato, A., Yoshitake, M., Iwamae, A., Furuya, S., Hatakeda, K., Miyazaki, A., Soejima, H., Hitomi, Y., Kumagai, K., Usui, T., Hayashi, T., Yamamoto, D., Fukai, R., Sugita, S., Kitazato, K., Hirata, N., Honda, R., Morota, T., Tatsumi, E., Sakatani, N., Namiki, N., Matsumoto, K., Noguchi, R., Wada, K., Senshu, H., Ogawa, K., Yokota, Y., Ishihara, Y., Shimaki, Y., Yamada, M., Honda, C., Michikami, T., Matsuoka, M., Hirata, N., Arakawa, M., Okamoto, C., Ishiguro, M., Jaumann, R., Bibring, J.-P., Grott, M., Schröder, S., Otto, K., Pilorget, C., Schmitz, N., Biele, J., Ho, T.-M., Moussi-Soffys, A., Miura, A., Noda, H., Yamada, T., Yoshihara, K., Kawahara, K., Ikeda, H., Yamamoto, Y., Shirai, K., Kikuchi, S., Ogawa, N., Takeuchi, H., Ono, G., Mimasu, Y., Yoshikawa, K., Takei, Y., Fujii, A., Iijima, Y., Nakazawa, S., Hosoda, S., Iwata, T., Hayakawa, M., Sawada, H., Yano, H., Tsukizaki, R., Ozaki, M., Terui, F., Tanaka, S., Fujimoto, M., Yoshikawa, M., Saiki, T., Tachibana, S., Watanabe, S.I., Tsuda, Y., 2023. Macromolecular organic matter in samples of the asteroid (162173) Ryugu. Science 379, eabn9057.

Yada, T., Abe, M., Okada, T., Nakato, A., Yogata, K., Miyazaki, A., Hatakeda, K., Kumagai, K., Nishimura, M., Hitomi, Y., Soejima, H., Yoshitake, M., Iwamae, A., Furuya, S., Uesugi, M., Karouji, Y., Usui, T., Hayashi, T., Yamamoto, D., Fukai, R., Sugita, S., Cho, Y., Yumoto, K., Yabe, Y., Bibring, J.-P., Pilorget, C., Hamm, V., Brunetto, R., Riu, L., Lourit, L., Loizeau, D., Lequertier, G., Moussi-Soffys, A., Tachibana, S., Sawada, H., Okazaki, R., Takano, Y., Sakamoto, K., Miura, Y.N., Yano, H., Ireland, T.R., Yamada, T., Fujimoto, M., Kitazato, K., Namiki, N., Arakawa, M., Naru, H., Yurimoto, H., Nakamura, T., Noguchi, T., Yabuta, H., Naraoka, H., Ito, M., Nakamura, E., Uesugi, K., Kobayashi, K., Michikami, T., Kikuchi, H., Naoyuki, H., Ishihara, Y., Matsumoto, K., Noda, H., Noguchi, R., Shimaki, Y., Shirai, K., Ogawa, K., Wada, K., Senshu, H., Yamamoto, Y., Morota, T., Honda, R., Honda, C., Yokota, Y., Matsuoka, M., Sakatani, N., Tatsumi, E., Miura, A., Yamada, M., Fujii, A., Hirose, C., Hosoda, S., Ikeda, H., Iwata, T., Kikuchi, S., Mimasu, Y., Mori, O., Ogawa, N., Ono, G., Shimada, T., Soldini, S., Takahashi, T., Takei, Y., Takeuchi, H., Tsukizaki, R., Yoshikawa, K., Terui, F., Nakazawa, S., Tanaka, S., Saiki, T., Yoshikawa, M., Watanabe, S., Tsuda, Y., 2022. Preliminary analysis of the Hayabusa2 samples returned from C-type asteroid Ryugu. Nat. Astron. 6, 214–220.

Yamaguchi, A., Tomioka, N., Ito, M., Shirai, N., Kimura, M., Greenwood, R.C., Liu, M.-C., McCain, K.A., Matsuda, N., Uesugi, M., Imae, N., Ohigashi, T., Uesugi, K., Nakato, A., Yogata, K., Yuzawa, H., Kodama, Y., Hirahara, K., Sakurai, I., Okada, I., Karouji, Y., Nakazawa, S., Okada, T., Saiki, T., Tanaka, S., Terui, F., Yoshikawa, M., Miyazaki, A., Nishimura, M., Yada, T., Abe, M., Usui, T., Watanabe, S., Tsuda, Y., 2023. Insight into multi-step geological evolution of C type asteroids from Ryugu particles. Nat. Astron. 7, 398–405.

Yokoyama, T., Nagashima, K., Nakai, I., Young, E.D., Abe, Y., Aléon, J., Alexander, C.M. O., Amari, S., Amelin, Y., Bajo, K., Bizzarro, M., Bouvier, A., Carlson, R.W., Chaussidon, M., Choi, B.-G., Dauphas, N., Davis, A.M., Di Rocco, T., Fujiya, W., Fukai, R., Gautam, I., Haba, M.K., Hibiya, Y., Hidaka, H., Homma, H., Hoppe, P., Huss, G.R., Ichida, K., Iizuka, T., Ireland, T.R., Ishikawa, A., Ito, M., Itoh, S., Kawasaki, N., Kita, N.T., Kitajima, K., Kleine, T., Komatani, S., Krot, A.N., Liu, M.-C., Masuda, Y., McKeegan, K.D., Morita, M., Motomura, K., Moynier, F., Nguyen, A., Nittler, L., Onose, M., Pack, A., Park, C., Piani, L., Qin, L., Russell, S.S., Sakamoto, N., Schönbächler, M., Tafla, L., Tang, H., Terada, K., Terada, Y., Usui, T., Wada, S., Wadhwa, M., Walker, R.J., Yamashita, K., Yin, Q.-Z., Yoneda, S., Yui, H., Zhang, A.-C., Connolly, H.C., Lauretta, D.S., Nakamura, T., Naraoka, H., Noguchi, T., Okazaki, R., Sakamoto, K., Yabuta, H., Abe, M., Arakawa, M., Fujii, A., Hayakawa, M., Naoyuki, H., Naru, H., Honda, R., Honda, C., Hosoda, S., Iijima, Y., Ikeda, H., Ishiguro, M., Ishihara, Y., Iwata, T., Kawahara, K., Kikuchi, S., Kitazato, K., Matsumoto, K., Matsuoka, M., Michikami, T., Mimasu, Y., Miura, A., Morota, T., Nakazawa, S., Namiki, N., Noda, H., Noguchi, R., Ogawa, N., Ogawa, K., Okada, T., Okamoto, C., Ono, G., Ozaki, M., Saiki, T., Sakatani, N., Sawada, H., Senshu, H., Shimaki, Y., Shirai, K., Sugita, S., Takei, Y., Takeuchi, H., Tanaka, S., Tatsumi, E., Terui, F., Tsuda, Y., Tsukizaki, R., Wada, K., Watanabe, S., Yamada, M., Yamada, T., Yamamoto, Y., Yano, H., Yokota, Y., Yoshihara, K., Yoshikawa, M., Yoshikawa, K., Furuya, S., Hatakeda, K., Hayashi, T., Hitomi, Y., Kumagai, K., Miyazaki, A., Nakato, A., Nishimura, M., Soejima, H., Suzuki, A., Yada, T., Yamamoto, D., Yogata, K., Yoshitake, M., Tachibana, S., Yurimoto, H., 2023. Samples returned from the asteroid Ryugu are similar to Ivuna-type carbonaceous meteorites. Science 379, eabn7850.

Zolensky, M.E., Barrett, R., Browning, L., 1993. Mineralogy and composition of matrix and chondrule rims in carbonaceous chondrites. Geochim. Cosmochim. Acta 57, 3123–3148.

Zolensky, M., Zega, T.J., Yano, H., Wirick, S., Westphal, A.J., Weisberg, M.K., Weber, I., Warren, J.L., Velbel, M.A., Tsuchiyama, A., Tsou, P., Toppani, A., Tomioka, N., Tomeoka, K., Teslich, N., Taheri, M., Susini, J., Stroud, R., Stephan, T., Stadermann, F.J., Snead, C.J., Simon, S.B., Simionovici, A., See, T.H., Robert, F., Rietmeijer, F.J.M., Rao, W., Perronnet, M.C., Papanastassiou, D.A., Okudaira, K.,

Ohsumi, K., Ohnishi, I., Meibom, A., Matrajt, G., Marcus, M.A., Leroux, H., Lemelle, L., Le, L., Lanzirotti, A., Langenhorst, F., Krot, A.N., Keller, L.P., Kearsley, A.T., Joswiak, D., Jacob, D., Ishii, H., Harvey, R., Hagiya, K., Grossman, L., Grossman, J.N., Graham, G.A., Gounelle, M., Gillet, P., Genge, M.J., Flynn, G.,

Ferroir, T., Fallon, S., Ebel, D.S., Dai, Z.R., Cordier, P., Clark, B., Chi, M., Butterworth, A.L., Brownlee, D.E., Bridges, J.C., Brennan, S., Brearley, A., Bradley, J.P., Bleuet, P., Bland, P.A., Bastien, R., 2006. Mineralogy and petrology of comet 81P/Wild 2 nucleus samples. Science 314, 1735–1739.